University of California, San Diego

UCSD-CER-09-01

Extreme-ultraviolet radiation transport in small scale length laser-produced tin plasmas

Kevin L. Sequoia

5 February 2009

Center for Energy Research
University of California, San Diego
9500 Gilman Drive
La Jolla, CA 92093-0417

CER
Center for Energy Research

UNIVERSITY OF CALIFORNIA, SAN DIEGO

Extreme-ultraviolet radiation transport in small scale length laser-produced tin plasmas

A Dissertation submitted in partial satisfaction of the Requirements for the degree Doctor of Philosophy

in

Engineering Sciences (Engineering Physics)

by

Kevin Lamar Williams Sequoia

Committee in charge:

Mark S. Tillack, Chair
Farhat Beg
Farrokh Najmabadi
Kevin B. Quest
George R. Tynan

The Dissertation of Kevin Lamar Williams Sequoia is approved, and it is acceptable in quality and form for publication on microfilm:

_____

_____

_____

_____

_____

Chair

University of California, San Diego

2009

Dedication

Throughout any individual's life, there are people that contribute to and nurture the growth of that individual, and there are the detractors and cynics. In my own life, I have had plenty of both. Although those who sought to bring me down played an important role; giving me strength to endure and motivation to prove them wrong, this work would not have happened without all of the people that have supported, encouraged, and believed in me through out my life.

There are so many people that have directly impacted me in a positive way it would be impossible to list them all here; many family members, friends, teachers, and coaches. The one person I would like to single out here and dedicate this work to is my Granddaddy, George Williams. Granddaddy taught me the value of hard work and generosity. He spent his life working extremely hard so that his children and grandchildren could live a better life than he had. Although he worked long hours, sometime multiple shifts, to earn the money needed to provide a decent standard of living for his family, he did not turn away from those in need. He could not just stand by and watch others in need if he could help them in any way. His life has been an example to me.

Granddaddy, I don't know where I would be without your influence in my life, but I know I would not have accomplished this. I hope you're proud of me. Thank you for all that you have given me. This is for you.

Epigraph

For light I go directly to the Source of light, not to any of the reflections.

~ Mildred Lisette Norman (Peace Pilgrim)

The light bulb has been around for 100 years. It's a great invention and a great light source ... but after 100 years, you would think we would make some progress from the efficiency standpoint.

~ Neal Hunter

Table of contents

List of figures

Acknowledgments

I would like to sincerely extend my gratitude to Dr. Mark Tillack for his continued support of my work and excellent guidance over the last several years. He has instilled into me that clear communication of ideas is just as, if not more, important as the ideas themselves. I cannot count the many hours I have spent discussing my work and, sometimes, backpacking trips with him. That time has proven to be invaluable to me and to the completion of this work. Most of all I would like to thank Dr. Tillack for his willingness to accommodate me at various times through out my studies at UCSD, so that I could maintain my family relationships.

I would also like to thank my doctoral committee: Professors Farhat Beg, Farrokh Najmabadi, George R. Tynan, and Kevin B. Quest. I feel extremely privileged to have such an all-star cast in the plasma physics community serve as my committee. I know that the members' time is very valuable and in short supply, so I am deeply appreciative that I have been given part of it.

The work I have done here would not have happened if not for Yezheng Tao. He has made it possible for the EUV program to continue and grow at UCSD making this work possible. He has provided excellent guidance and insight into the phenomena associated with laser-produced plasmas, and has been an exemplary model for me of a prolific publishing scientist.

The numerical simulations in this work would not have been possible without the help of Dr. Howard Scott and Dr. Jon Larsen. Dr. Scott's guidance on the proper use of Cretin and all the time he spent with me during my summer visit to Lawrence Livermore National Laboratory are greatly appreciated. Dr. Larsen's rapid response to issues and

help with Hyades and h2d was key to the completion of all the numerical simulations in my doctoral work.

I would also like to thank John Pulsifer for his maintaining the laboratory throughout my stay at UCSD. He has provided support to all of the experiments in the UCSD laser plasma and laser-matter interaction laboratory, and has been an excellent sounding board for ideas on experimental techniques and design. He has been a great friend to me over the last nearly six years. I have learned a great deal from him and will miss the discussions about experiments, the economy, business schemes, and photography.

Sam Yuspeh and Russell Burdt have also been very helpful to me over the last couple of years. Sam has been extremely helpful to me in on both experimentally, helping acquire the hundreds of shots needed to complete the data set used in this work, and on the computational side, by helping me keep the many iterations of h2d simulations running continuously. Russell's eye for misspellings and grammar mistakes have paid off many times in the presentations and publications I have made. They both have played an important role in helping me interpret the data and simulations in my dissertation.

Finally, I would like to thank my wife, Jacqueline Sequoia, for her continued love and support for the last eleven years. I can always count on her to be there for me no matter what. Her continued encouragement has helped me make it through some of those days when my experiments or computer simulations were not working.

Vita

2009 Doctor of Philosophy, Engineering Physics, University of California, San Diego

2005 Master of Science, Engineering Physics, University of California, San Diego

2002 Bachelor of Arts, Physics, Berea College, Berea

Publications

Y. Tao, M. S. Tillack, **K. L. Sequoia**, R. A. Burdt, S. Yuspeh and F. Najmabadi. "Efficient 13.5 nm extreme ultraviolet emission from Sn plasma irradiated by a long CO_2 laser pulse," Applied Physics Letters 92, 251501 (2008).

K. L. Sequoia, Y. Tao, S. Yuspeh, R. Burdt, and M. S. Tillack. "Two dimensional expansion effects on angular distribution of 13.5 nm in-band extreme ultraviolet emission from laser-produced Sn plasma," Applied Physics Letters 92, 221505 (2008).

Y. Tao, M.S. Tillack, S.S. Harilal, **K. L. Sequoia**, R.A. Burdt, and F. Najmabadi. "Mass-limited Sn target irradiated by dual laser pulses for an extreme ultraviolet lithography source," Optics Letters, 39, 1339 (2007).

Y. Tao, M.S.Tillack, S.S.Harilal, **K. L. Sequoia**, and F.Najmabadi. "Investigations on interaction of a laser pulse with a pre-formed Gaussian Sn plume for an extreme ultraviolet lithography source," Journal of Applied Physics 101, 023305 (2007).

Y. Tao, S. S. Harilal, M. S. Tillack, **K. L. Sequoia**, B. O'Shay, and F. Najmabadi. "Effect of focal spot size on in-band 13.5 nm extreme ultraviolet emission from laser-produced Sn plasma," Optics Letters, 31, 2492 (2006).

Y. Tao, M. S. Tillack, S. S. Harilal, **K. L. Sequoia**, B. O'Shay, and F. Najmabadi. "Effect of shockwave-induced density jump on laser plasma interactions in low-pressure ambient air," Journal of Physics D:Applied Physics 39, 4027 (2006).

M. S. Tillack, **K. L. Sequoia** and Y. Tao. "Geometric effects on EUV emissions in spherical and planar targets," Journal of Physics: Conference Series 112 042060 (2008).

K. Sequoia, Y. Tao, M.S. Tillack. "High conversion efficiency for laser-produced EUV plasmas with longer pulse durations," Proceedings of IEEE Pulsed Power and Plasma Science Conference (2007).

Y. Tao, M. S. Tillack, **K. L. Sequoia**, F. Najimabadi. "A mass-limited Sn target irradiated by dual laser pulses for an EUVL source," Proceedings of SPIE Vol. 6517, 65173Q, Emerging Lithographic Technologies XI, April 2007.

M. S. Tillack, **K. L. Sequoia**, B. O'Shay, C. A. Back and H. A. Scott. "Optimization of plasma uniformity in laser-irradiated underdense targets," Inertial Fusion Science and Applications 2005, Biarritz France, September 2005.

M. S. Tillack, J. Pulsifer, and **K. Sequoia**. "UV Laser-Induced Damage to Grazing Incidence Metal Mirrors," Inertial Fusion Science and Applications 2003, Monterey CA, pp. 810-814, September 2003.

K. L. Sequoia, M. S. Tillack and H. A. Scott. "A comparison of Hyades and Cretin for modeling laser absorption in underdense plasmas," UCSD Center for Energy Research internal report December 2006.

M. S. Tillack, J. F. Latkowski, J. E. Pulsifer, **K. L. Sequoia** and R. P. Abbott. "Grazing-Incidence Metal Mirrors for Laser-IFE," September 2005.

Y. Tao, M.S. Tillack, S.S. Harilal, B. O'Shay, **K. Sequoia** and F. Najmabadi. "Comprehensive and reliable diagnostics for the corona of laser-produced plasmas," September 2005.

K. L. Sequoia, M. S. Tillack, T. Albert, M. Wolford and J. D. Sethian. "Grazing Incidence Metal Mirror Mid-Scale Optics Research Plan," UCSD CER technical report, May 28, 2004.

M. S. Tillack, F. Najmabadi, A. R. Raffray, Z. Dragojlovic, A. C. Gaeris, J. E. Pulsifer, **K. Sequoia**. "High-Average-Power Laser Program Optics and Chamber Studies: Report on Research Performed During FY03," March 1, 2004.

A. C. Gaeris, B. Harilal, **K. Sequoia** and M. S. Tillack. "Aerosol Diagnostics for Liquid-Protected IFE Chambers," UCSD CER technical report, October 1, 2003.

K. L. Sequoia. "Techniques for controlling the radiative properties of underdense laser-produced plasma," UCSD CER Applied Plasma Physics and Fusion Energy Seminar Series, November 15, 2006.

K. L. Sequoia, M. S. Tillack, B. O'Shay, H. A. Scott, C. A. Back. "Optimization of Plasma Uniformity in Laser Irradiated Underdense Targets," UCSD Jacobs School of Engineering Research Expo 2006, Febuary 23, 2006.

M. S. Tillack, J. Pulsifer, **K. Sequoia**, R. Harrison. "Grazing Incidence Metal Mirrors for Final Optics," 12th Laser IFE Program Workshop, LLNL, June 20-21 2005.

M. S. Tillack, J. Pulsifer, **K. Sequoia**, R. Harrison. "Examination of the statistical aspects of laser-induced damage in metal mirrors," 12th Laser IFE Program Workshop, LLNL, June 20-21 2005.

M. S. Tillack, J. Pulsifer, **K. Sequoia**. "The End Game for Aluminum GIMM Fabrication and Laser Induced Damage Testing," 11th Laser IFE Program Workshop, NRL, March 3-4 2004.

M.S. Tillack, Z. Dragojlovic, F. Hegeler, E. Hsieh, J. Mar, F. Najmabadi, J. Pulsifer, **K. Sequoia**, M. Wolford. "Final Optic Research – Progress and Plans," 10th Laser IFE Program Workshop, PPPL, October 27-28 2004.

M. S. Tillack, J. Pulsifer, **K. Sequoia**, K. Cockrell. "Final Optic Research – Progress and Plans," 9th Laser IFE Program Workshop, UCLA, June 2-3 2004.

F. Najmabadi, J. Pulsifer, **K. Sequoia**. "Armor Simulation Experiments at Dragonfire Facility," 9th Laser IFE Program Workshop, UCLA, June 2-3 2004.

M.S. Tillack, J. Pulsifer, **K. Sequoia**. "Final Optic Research – Progress and Plans," 8th Laser IFE Program Workshop, Georgia Tech, February 5-6 2004.

F. Najmabadi, **K. Sequoia**. "Progress in Chamber Simulation Experiments at UCSD Laser Facility," 8th Laser IFE Program Workshop, Georgia Tech, February 5-6 2004.

M.S. Tillack, J. Pulsifer, **K. Sequoia**. "Progress on GIMM Fabrication and Testing," 7th Laser IFE Program Workshop, University of Wisconsin, "September 24-25 2003.

F. Najmabadi, **K. Sequoia**, S. Chen. "Progress in Chamber Simulation Experiments at UCSD Laser Facility," 7th Laser IFE Program Workshop, University of Wisconsin, September 24-25 2003.

M. S. Tillack, J. Pulsifer, **K. Sequoia**, E. Hsieh, T. Walsh, W. Kowbel. "IFE Final Optics Using SiC Substrates and Al Coatings," 6th Laser IFE Program Workshop, Sandia National Laboratories, April 9-10 2003.

ABSTRACT OF THE DISSERTATION

Extreme-ultraviolet radiation transport in small scale length laser-produced tin plasmas

by

Kevin Lamar Williams Sequoia

Doctor of Philosophy in Mechanical Engineering (Engineering Physics)

University of California, San Diego, 2009

Mark S. Tillack, Chair

The majority of the studies on laser-produced plasmas as an efficient extreme ultraviolet (EUV) light source have focused on relatively large plasmas produced at large laser facilities. However, to develop a commercially viable light source for EUV lithography, much smaller lasers and hence much smaller plasmas must be employed. Smaller plasmas behave quite differently than large plasmas in that the temperature and density are less uniform, and lateral expansion is more important. These differences affect the energy transport and, in particular, the radiation transport. This work studies the EUV radiation transport in small scale length tin plasmas, focusing on the effects of target geometry and laser pulse duration.

Both planar and spherical tin targets were irradiated with an Nd:YAG laser operating at 1.064 μm. Conversion efficiency of laser light to 13.5 nm radiation (in-band), EUV emission spectrum, two-dimensional in-band emission profile, and the plasma electron density were measured experimentally. These measurements provide

insight into where the laser is absorbed, where the in-band emission is produced, and how the radiation is transmitted. The plasma evolution in these experiments were simulated with a two-dimensional radiation hydrodynamic code, while the radiation transport and atomic kinetics where modeled with a collisional radiative code. Additional experiments were conducted using planar targets where the pulse duration was varied from 0.5 ns to 16 ns to understand the effects of laser pulse duration.

It was found that the optimum plasma temperature for efficient generation and transmission of in-band emission is 20 eV. This is lower than the previously reported optimum temperature of 30 eV. The use of a 1.064 μm heating laser results in overheating of the plasma in a region that is much too dense to transmit the in-band emission. This overheating is necessary for the plasma to reach the optimum temperature in the region where the density is low enough to transmit the in-band emission.

1. Introduction

1.1. Background on EUV lithography

In 1965, Intel co-founder Gordon E. Moore first described the trend for computer hardware, stating that "The complexity for minimum component costs has increased at a rate of roughly a factor of two per year…" [1]. Since then the trend has continued and has become known as Moore's law. For the last four decades electronic components have doubled storage capacity, clock speed, etc. every year, see Figure 1.1. The technique that has allowed Moore's law to continue for so long is photolithography. Currently the limiting factor for how small a feature can be made on a component is the diffraction limit. Although quantum effects will soon play a large role as the feature sizes approach the atomic scale. The diffraction limited resolution for a projection lithography lens is given by [2]

$$W = k_1\left(\frac{\lambda}{NA}\right), \tag{1.1}$$

where k_1 is an empirical constant, and λ and NA are the wavelength and numerical aperture of the exposure tool. The current state of the art lithography systems employ ArF excimer lasers emitting 193 nm light. This is the shortest wavelength laser with the power and cost requirements suitable for high volume manufacturing (HVM) lithography systems. These lasers can produce feature sizes below 65 nm when combined with liquid submerging techniques that push the NA over 1.2 [3]. However, it is believed that the

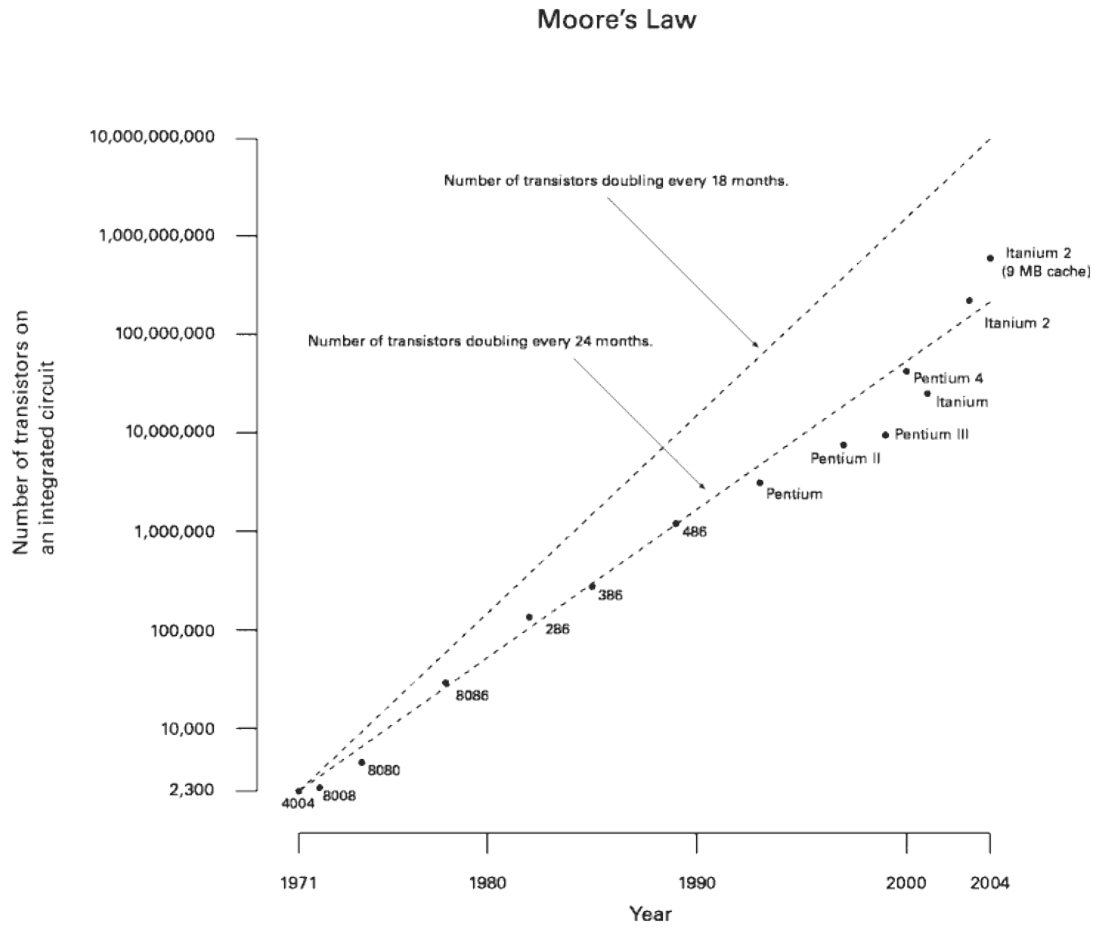

Figure 1.1: Moore's Law for the number of transistors on an integrated circuit. Permission is granted to copy, distribute and/or modify this figure under the terms of the GNU Free Documentation License.

limit has been reached using these techniques and in order for Moore's law to continue in the near future, a new light source must be developed that is capable of meeting the HVM criteria. The new light source must have a high average power at a wavelength of around 10 nm. The large decrease in wavelength is necessary due to the fact that liquid submersion can not be used below 193 nm due to absorption. It must also be capable of near continuous operation for several years to produce the number of components required. In addition the operating cost must be low enough to make the next generation of micro chips affordable.

The current leading candidate for the next generation photolithography source is a plasma radiating extreme-ultraviolet (EUV) light. Extreme-ultraviolet lithography (EUVL) will enable manufactures to make feature sizes below 50 nm [4, 5]. The wavelength of choice is 13.5 nm, because of the availability of highly reflective multilayer Mo/Si mirrors [6]. The three main sources for EUV emission are synchrotron radiation, pulsed discharge produced plasma (DPP), and laser-produced plasma (LPP) [7]. A synchrotron source, costing over ten times as much as the expected cost of an EUVL system, would be much too expensive for a HVM tool, so there are really only two choices. Both DPP and LPP are promising sources, and significant effort has been applied to develop both. This work will focus on LPP sources.

Once the heating source has been determined, here the source is a LPP, the emitter must be selected. There are three popular choices for the emitter of an EUVL source: Xe, Li, and Sn [8-10]. Sn emitters produce much more light since the emission comes from a range of charge states, Sn^{+8} to Sn^{+13} [6]. The higher emission makes Sn the emitter of choice for this research. The conversion efficiency (CE), laser energy to EUV,

is a key issue because of the high power demands of HVM. An EUVL source needs to produce 300 W of in-band, 13.5 nm with 2% bandwidth, power at intermediate focus to properly expose the photo resist [5]. For any LPP system to be economically viable for HVM, the CE needs to be at least 3% [11].

1.2. Background on laser-produced plasmas

Laser-produced plasmas have been studied for many years now and have been important for the study of inertial confinement fusion [12, 13], soft X-ray sources [14-16], X-ray lasers [17, 18], measuring the opacities and equations of state for high-density matter [19-22], particle accelerators [23], and laboratory astrophysics [24]. High-power pulsed lasers can be focused to produce very high intensities. When these lasers are focused onto a dense target, an environment with extreme conditions is produced. In the context of this work a LPP is created when a laser if focused to high intensity (10^{11} – 10^{17} W/cm^2) with wavelength from ten microns down to a quarter micron on to a solid density target. The high radiation intensity ionizes atoms at the surface because the electric field in the laser is comparable to that of the fields that keep the electrons in their orbits. The laser is then absorbed by two methods, collisions between the electrons and ions (inverse Bremsstrahlung absorption, IBA) and damping of plasma waves (resonance absorption). Once the laser energy begins to absorb a LPP can be thought of as consisting of three regions. The first region, referred to as the coronal region, is where the laser absorption occurs. Here the density is at or below the critical density, n_c:

$$n_c = \frac{m_e \omega^2}{4\pi e^2} \approx 1.1 \times 10^{21} \lambda_\mu^{-2} \, (cm^{-3}), \tag{1.2}$$

where m_e is the electron mass, ω is the laser frequency, e is the charge for an electron, and λ_μ is the laser wavelength in microns. The absorbed laser energy is transported into the second region by a nonlinear heat wave towards higher densities, where the

temperature drops rapidly. The boundary between the first and second region is referred to as the ablation front. The third region is where a compression wave produces a density jump where the density is above that of the solid target material. Typical parameters for a LPP can be seen in Figure 1.2. Here it is clear that LPP contains very steep gradients in temperature and density, as well as any parameters that may depend on the temperature and density.

In this work most of the laser absorption takes place via IBA, which for a Maxwellian distribution is given by,

$$\kappa_{IB} = \frac{4\pi^3 e^6 \overline{Z} n_e^2 \ln\Lambda}{3\omega^2 c\left(2\pi m_e k_B T_e\right)^{3/2}\sqrt{\varepsilon}}, \tag{1.3}$$

where,

$$\varepsilon = 1 - \frac{\omega_{pe}^2}{\omega^2}, \tag{1.4}$$

is the dielectric constant of the plasma, ln Λ is the Coulomb logarithm, $\overline{Z}$ is the average ionization level of the plasma, n_e is the electron number density, and ω_{pe} is the electron-ion collision frequency [25]. In the IBA process the electric field of the light gives the electrons in the plasma energy via quiver motion. The quiver motion is then transferred via collisions into random thermal motions of the electrons.

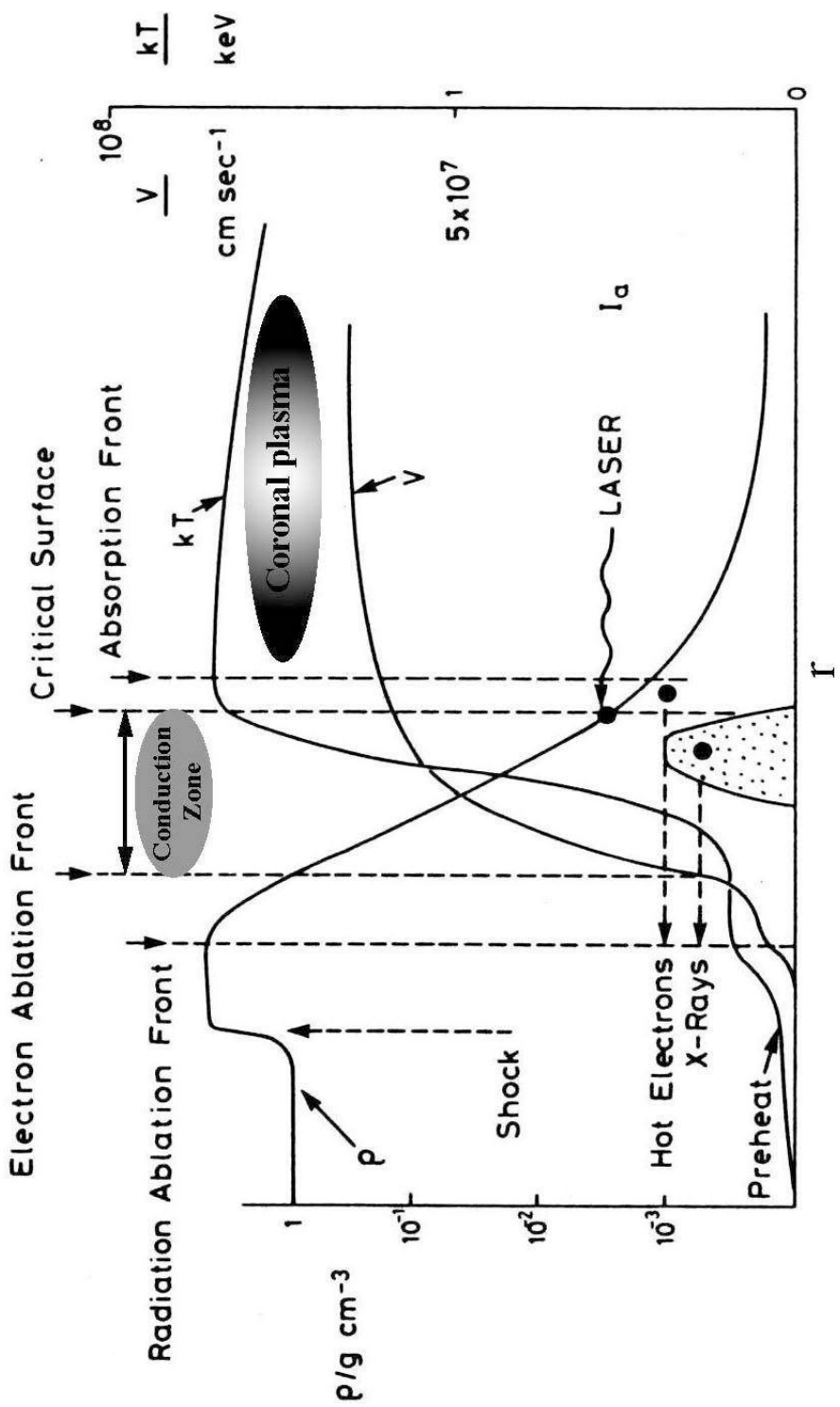

Figure 1.2: Typical plasma parameters for a LPP with the laser intensity between 10^{11} and 10^{17} W/cm^2 [26

A characteristic intensity for IBA can be defined as,

$$I^* = \frac{10^{12}\,\overline{Z} l_\mu f}{\lambda_\mu^4}\,(W/cm^2)\,. \tag{1.5}$$

Here l_μ and λ_μ are the plasma scale length and the laser wavelength in microns, and f is the flux limit [26]. The plasma scale length is given by,

$$l_s = C_s \tau_{laser}\,, \tag{1.6}$$

where,

$$C_s = \left(\overline{Z} T_e / M_i\right)^{1/2}, \tag{1.7}$$

is the plasma sound speed with M_i, and τ_{laser} being the ion mass, and laser pulse duration [27]. When the laser intensity $I << I^*$, absorption can be approximated as 100%.

In this work I is between 10^{10} and 10^{12} W/cm^2, $\overline{Z}$ is around 1 to 14, λ_μ is about 1 μm, and l_μ is around 200 μm. The flux limit does not apply here since classical electron conduction is still valid in for these conditions, but a typical range for f would be 0.01 to 1. With these parameters $I^* \sim 10^{15}$, hence 100% of the laser energy is absorbed via IBA.

The plasma scale length is a result of ionization of atoms and hydrodynamic motion of the plasma. These two processes can be described by the equation of state (EOS). From reference [28] using the ideal-gas approximation the pressure, p, and energy, E, are described by,

$$\begin{aligned} p &= p_e + p_i + p_r\,, \\ E &= E_e + E_i + E_r\,, \end{aligned} \tag{1.8}$$

Hence the electrons, ions, and radiation can be treated separately. In a plasma where the density is not too high and the temperature is below ~ 10 eV the ion thermal pressure is dominant. For plasmas that are optically thick and the temperature is above 1 keV the radiation becomes important. The range between these two, where the coronal plasma lies, can be treated as an ideal gas. The partially ionized ideal-plasma EOS is given by,

$$\begin{aligned} p_e &= n_e k_B T_e = \frac{\overline{Z}\rho k_B T_e}{M_i}, \\ E_e &= \left(\frac{3}{2}\overline{Z}k_B T_e + E_i\left(Z,\overline{Z}\right) \right) \Big/ M_i \end{aligned}, \tag{1.9}$$

where ρ is the mass density, $E_i\left(Z,\overline{Z}\right)$ is the sum of the first $\overline{Z}$ ionization potentials.

Nearly all of the equations so far have a dependence on the charge state of the plasma, $\overline{Z}$. There are several methods of calculating $\overline{Z}$ including: Thomas-Fermi theory [29], Quantum spherical-cell model [30, 31], Saha equation [32, 33], Atomic rate equations [34], and Screened-hydrogenic model [35, 36]. For this work the screened-hydrogenic model was employed. This model calculates the average populations of bound electronic states, P_n, with screening formulas for the energy levels. The energy and charge states for the each principle quantum number, n, are given by,

$$\begin{aligned} E_n &= E_n^0 - \frac{Q_n^2 e^2}{2a_0 n^2}, \\ Q_n &= Z - \sum_{m \le n} \sigma_{nm} P_m, \end{aligned} \tag{1.10}$$

where a_0 is the Bohr radius, and σ_{nm} are screening coefficients. In the case when the plasma is in local thermodynamic equilibrium (LTE) the populations can be calculated by,

$$P_n = \frac{2n^2}{1+\exp\left(E_n - \mu_c\right)/k_B T_e}, \tag{1.11}$$

where μ_c is the chemical potential. For Non-LTE plasma the populations are determined by rate equations.

While the EOS is a good starting point for calculating plasma parameters, radiation transport must also be taken into account in order for the calculations to be accurate. Radiation is one of the dominant means of energy transport in a plasma, and can have a huge impact on the excited states of the atoms. The radiation transfer equation can be written as,

$$\frac{1}{c}\left(\frac{\partial I_\upsilon}{\partial t} + c\Omega\cdot\nabla I_\upsilon\right) = j_\upsilon\left(1+\frac{c^2}{2h\upsilon^3}I_\upsilon\right) - \kappa_\upsilon I_\upsilon. \tag{1.12}$$

The radiation transfer equation gives the radiation intensity I_υ at a frequency υ as the light beam passes through a medium. On the right hand side is the emission term with the spontaneous emission coefficient j_υ, and the absorption term with the absorption coefficient κ_υ. Ω is the direction of the beam, and h is Planck's constant. One important feature of Equation (1.12) is that I_υ, j_υ, and κ_υ are all dependent on the frequency of the light. It is this frequency dependence that makes radiation transport calculations difficult for high Z materials. There are several methods of dealing with this problem such as using gray opacities [37-39], or treating the many lines of similar wavelength together as a group [40, 41]. This topic will be discussed in more detail in the sections describing the computational portion of this work, sections 3.1 and 3.2.

It should be noted that most of the methods described here for calculating the various plasma parameters are approximations. The refinement of these methods and

others is an on going project carried out by hundreds if not thousands of scientist around the world, the details of which are beyond the scope of this work. The material presented in this section is meant to provide an overall picture of the important interplay of plasma parameters.

1.3. Review of LPP EUV lithography sources

In recent years LPP base EUV sources have been studied extensively [8-11, 19, 42-53]. All of the important laser parameters have been explored to some degree. For Sn based sources, the in-band emission comes from the $4p^6 4d^N - 4p^5 4d^{N+1} + 4p^6 4d^{N-1} 4f$ ($9 \geq N \geq 1$) transitions, the unresolved transition array (UTA), produced in Sn^{5+} to Sn^{13+} [54], with Sn^{9+}, Sn^{10+}, Sn^{11+} contributing a majority of the in-band emission.

Spitzer et al. conducted a very broad study where target material, pulse duration, laser wavelength, intensity, and spot size were all studied [42]. The results of those experiments showed that a Sn based source would have a CE of less than 1%. Additionally they found that the laser pulse duration, from 7.5 to 30 ns, and wavelength, from 1.064 to 0.532 μm, had little or no effect on the CE, and that laser energy and spot size would not affect the plasma parameters when lateral expansion is minimal.

More recent studies have found that the CE can be increased by carefully selecting the proper laser parameters. For example there have been several studies that have shown the dependence of CE on laser intensity [49, 55, 56]. The laser intensity determines the temperature range of the plasma. A plasma temperature of around 30 eV, making the average charge state 10^+, is optimum for the production of 13.5 nm emission from Sn [49, 57]. It has been shown, see [49], that with a laser intensity around 5×10^{10} W/cm^2 the CE can be higher than 2%.

ensity for 2 to 15 ns laser pulse

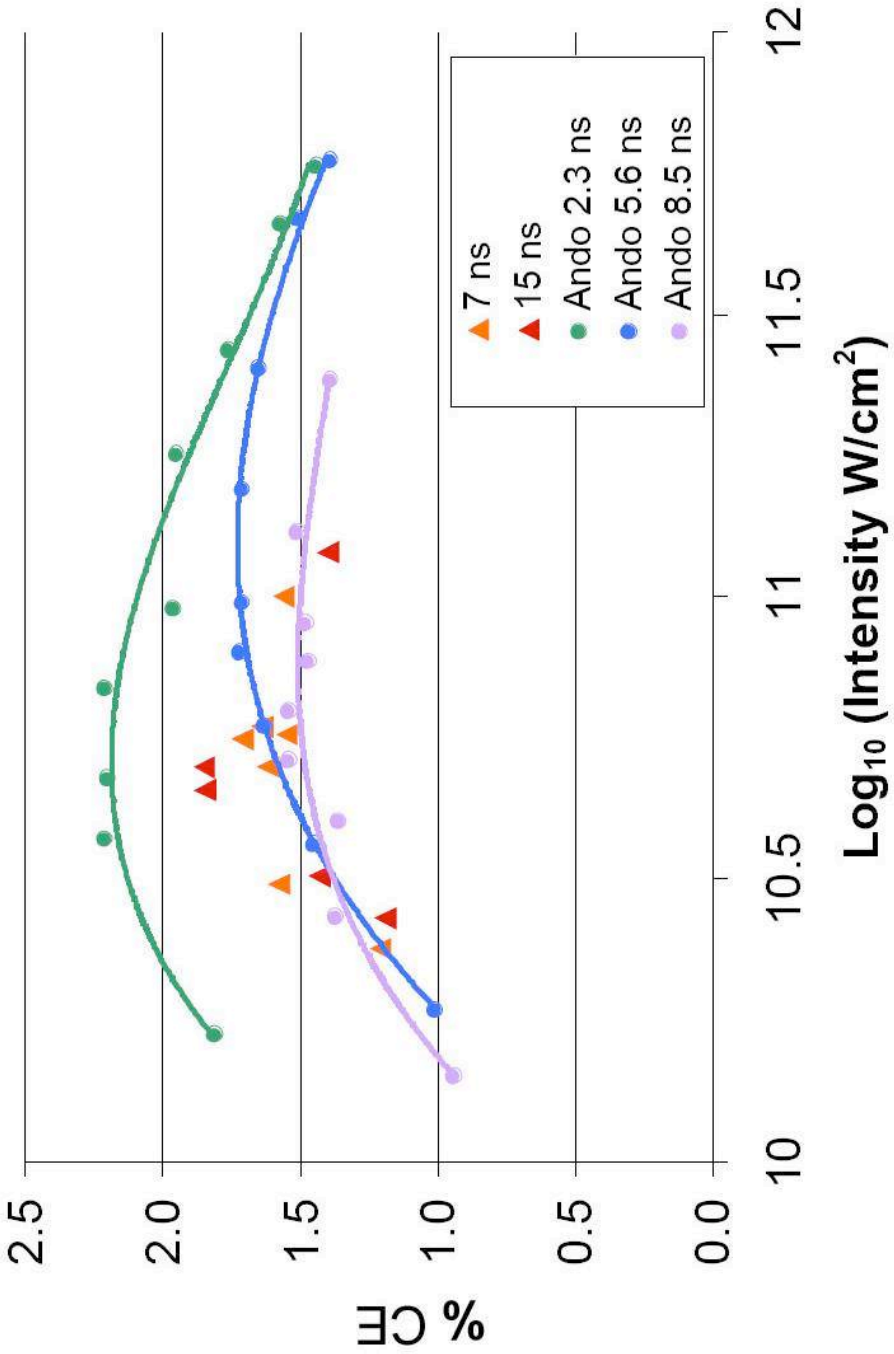
% CE
2.5
2.0
1.5
1.0
0.5
0.0
10
10.5
11
11.5
12
Log10 (Intensity W/cm2)
7 ns
15 ns
Ando 2.3 ns
Ando 5.6 ns
Ando 8.5 ns

There are also studies that reveal the importance of the laser pulse duration [49, 57]. The CE is highly dependent on the pulse duration, as shown in Figure 1.4, because the optical depth of the in-band emitting region changes when the pulse duration is changed. For long pulse lasers, since the plasma is optically thick to the in-band emission, much of the emission is absorbed before it can escape the surrounding lower temperature plasma because the plasma scale length is too long. For short laser pulses the limiting factor is the scale length of the laser absorption region. To obtain maximum CE the laser should be absorbed in the region where the in-band emission is produced. If this region is too small because the pulse is not long enough for the region to grow, then the emitting volume will be small, yielding little light [49].

The laser wavelength also plays an important role, and currently 10 μm wavelength, CO_2 lasers are producing much higher CE than 1.064 μm Nd:YAG lasers [58, 59]. This effect is again caused by the opacity of the plasma. The longer wavelength laser allows heating in the lower density plasma where the absorption of the in-band light is lower. Because of this many research groups have shifted focus away from Nd:YAG systems in favor of CO_2 lasers.

Along with the experimental work in this area, an equally extensive numerical modeling effort has been carried out, with the aim of gaining further understanding of the physics involved as well as to more easily explore the plethora of parameters that affect the EUV emission [45, 46, 56, 60-72]. There are essentially two main components of the modeling. The first component, radiation hydrodynamic (RH) simulations, calculates the evolution of the plasma properties as the laser energy is absorbed. This information can be used to understand issues of energy transport, laser absorption, and hydrodynamic

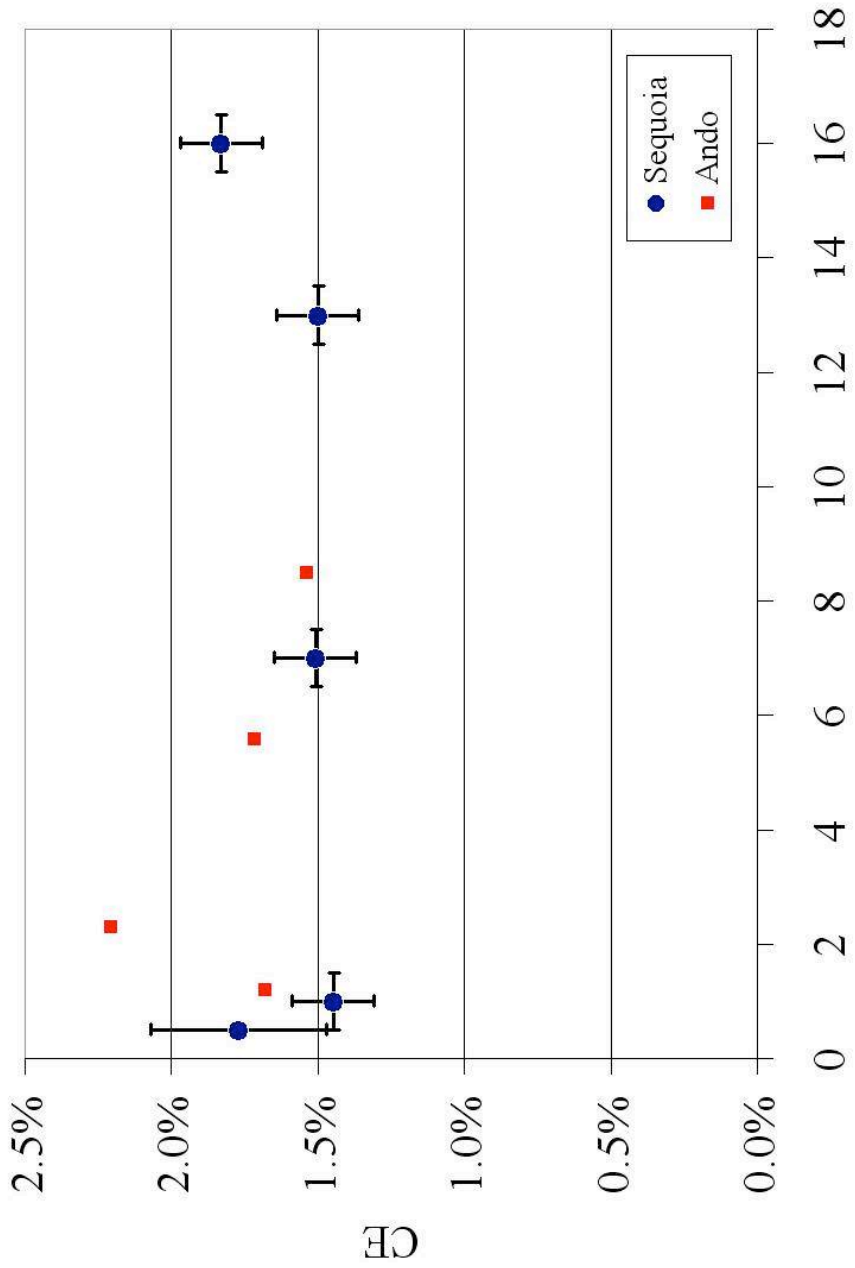

Figure 1.4: The effect of pulse duration on CE from [57], experiments discussed in Chapter 7.

motion, or it can be used along with the second component, atomic physics and radiation transport, to provide a complete picture of how the light is produced and what happens to it as it propagates through the plasma. The RH codes typically use a gray opacity model for the radiation transport, which provides reasonable results in regards to the plasma properties [46, 66-68]. This means that no line radiation, i.e. in-band transitions, will not be included in any radiation transport.

The atomic physics and radiation transport is typically treated separately. The reason for this is the complexity of the problem makes it difficult for one code to adequately handle the entire problem [72]. In a problem involving Sn^{6+} to Sn^{13+}, the charge states responsible for the in-band emission, there are tens of thousands of transitions that must be accounted for [70]. These transitions, referred to as an unresolved transition array (UTA), are from near-degenerate energy levels that can be treated statistically [72]. Once the important transitions have been accounted for properly, the atomic data is imported into a collisional-radiative (CR) model along with the plasma parameters from a RH code. The CR code uses the provided data and plasma parameters to calculate the detailed radiative and ionization phenomenon.

1.4. Dissertation objectives and organization

The research mentioned in the proceeding chapters begin to explore the physics behind producing efficient in-band EUV from laser produced. However, more work is needed to gain a better understanding of how the plasma heating process affects the radiation transport and opacity in the EUV spectral range. It was not until the need for a

EUVL source came about that these mid-Z, small scale length, several tens of eV plasmas were of interest to the scientific community. Therefore many of the mechanisms of radiation transport in this regime has not been explored thoroughly. The efficiency of EUV production can be improved by tailoring the temperature and electron density evolution of the plasma. This tailoring to the plasma conditions not only involves creating optimum conditions for EUV production, but also requires minimizing the absorption of the sought after light from the surrounding plasma expansion. The figure of merit in this work is the in-band CE.

Here two methods of controlling the plasma dynamics are explored. First, the affects of the target surface geometry are investigated by irradiating planar and spherical targets under identical laser conditions. It is well known that the plasma expansion occurs normal to the target surface. The plasma expansion affects every aspect of the plasma evolution from the plasma scale length to the opacity. Understanding the effects of the plasma expansion on the plasma is of key importance for efficient EUV production.

The second method for controlling the plasma evolution in this work is variation of the laser pulse duration. For the laser intensities and pulse durations in this work the dominant absorption mechanism is inverse-Bremsstrahlung. As the pulse duration increases, the location of the absorption moves away from the target surface and the amount of heated material increases. This provides an opportunity to control what region of the plasma is heated, and thus how much light is produced and then reabsorbed.

This dissertation is organized into six chapters. In chapter 1 the motivation and background for this work are given. The details and theory behind the experimental

arrangements and procedures can be found in chapter 2. An overview of the numerical models used for 2-D radiation hydrodynamic simulations (h2d) and atomic kinetics and radiation transport (Cretin) is provided in chapter 3. Chapter 4 contains the work that explores the effects of target geometry on the plasma evolution and CE. In chapter 5 the laser pulse duration results are presented. The final chapter, chapter 6, contains general conclusions drawn from the work and suggestions for future work.

2. Experimental description

2.1. Experimental layout

The basic experimental layout is illustrated in Figure 2.1. A pump laser is focused onto a tin target at the center of a vacuum chamber. The pump laser is either the EKSPLA SL355 or the Continuum Surelite II-10. The beam is focused using a f = 40 cm or f = 30 cm plano-convex antireflection lens.

A second laser is used as a probe beam, which passes through the plasma, perpendicular to the pump laser. Timing between the pump and probe laser is controlled by a Stanford DG535 pulse delay generator with less than 0.5 ns jitter. The probe laser is typically the EKSPLA SL355 frequency doubled to 532 nm with the pulse duration set to 130 ps. This beam is used for interferometry, described in section 2.2.

The targets are positioned remotely to the center of the chamber using a three-axis translation stage. The chamber is evacuated using a cryogenic pump, and the chamber pressure is 10^{-5} for the duration of the experiment. A soft x-ray transmission grating spectrometer (TGS) and absolutely calibrated in-band energy monitor (E-Mon) are both aligned to the target surface at 45° with respect to normal. The details of each diagnostic will be contained in the sections pertaining to each tool.

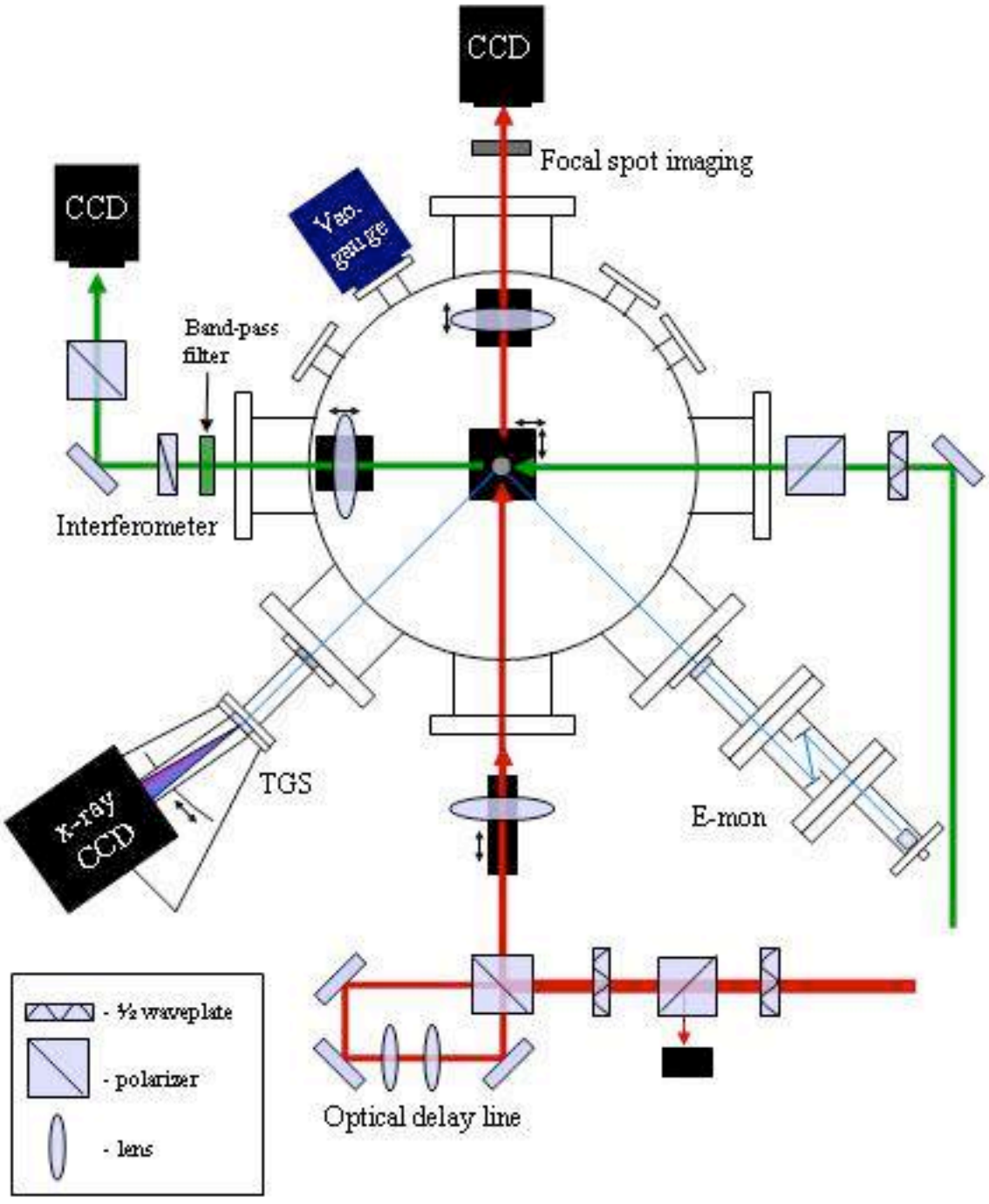

Figure 2.1: Experimental layout (not all stirring mirrors are shown)

2.2. Laser characterization

There are two solid state Nd:YAG laser power sources used in this work. One is the Continuum Surelite II-10 with maximum beam energy around 650 mJ at 1.064 μm. The temporal pulse is Gaussian with a full width at half maximum (FWHM) of about 7 ns Figure 2.2. The laser is operated at 1 Hz, by external triggering, continuously through out the experiment. The spatial profile is also Gaussian and can be seen in Figure 2.3. The second laser source for this work is the Ekspla SL355. The maximum beam energy for this laser is 500 mJ at 1.064 μm. The temporal pulse shape is Gaussian and the FWHM can be varied from 130, see Figure 2.4, to 550 ps, via SBS compression by rotating a lens wheel. The spatial profile is Gaussian and can be seen in Figure 2.5. Each laser is can be frequency doubled to 532 nm for use as a plasma probe.

Laser energy is measured using a thermal volume absorbing head (Ophir Model HE-150), by picking a single pulse from the pulse train. Several measurements are recorded in this way so that the energy and its shot-to-shot stability are fairly well known. Q-switch and flashlamp voltages and timing are fixed throughout the experiments to prevent changes in the laser pointing, divergence, and timing. The laser energy on target is controlled by an attenuator comprised of a half-waveplate and a cube polarizing beam splitter. The laser temporal pulse is monitored with a fast photodiode (Electro-Optics Technology ET-2000, 200 ps rise time) coupled to a 500 MHz oscilloscope.

The pulse duration of each laser can be extended up to a factor of two by using an optical delay path as shown in Figure 2.1. The beam passes through a ½ waveplate before entering a polarizing cube beam splitter. The s-polarized light is directed to the target surface immediately, while the p-polarized light is sent through an optical delay

line. A telescope composed of a lens pair is placed along the delay path so that the beam divergence can be corrected. The telescope allows the two beams to be focused to the same spot size at the target surface. Focal spot imaging is used to ensure both beams focus to the same size, intensity, and location.

Table 2.1: Nd:YAG laser source parameters

Laser	Max Energy (mJ)	Shortest pulse duration FWHM (ns)	Extended pulse duration range FWHM (ns)
Surelite	650	8	8 – 15
SL355	500	0.130	0.13 - 1

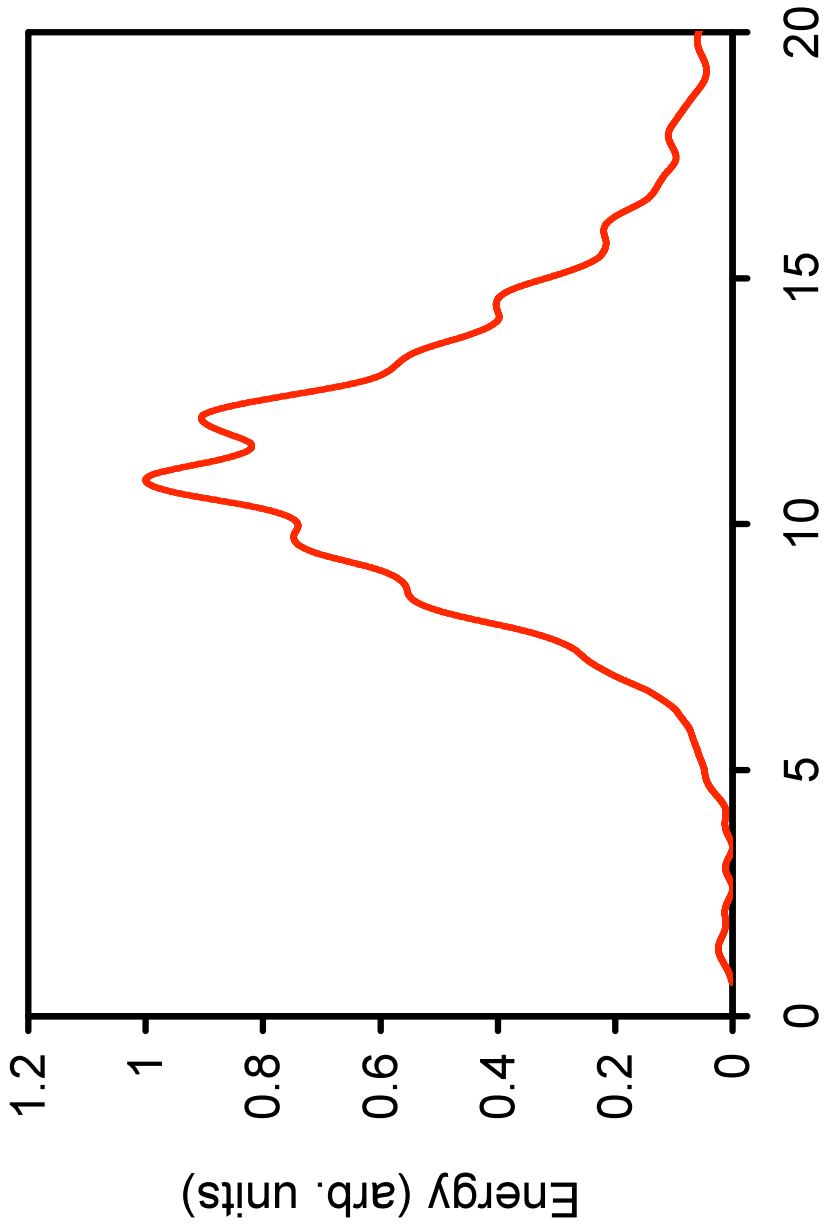

Figure 2.2: Typical temporal pulse shape of the Surelite II-10.

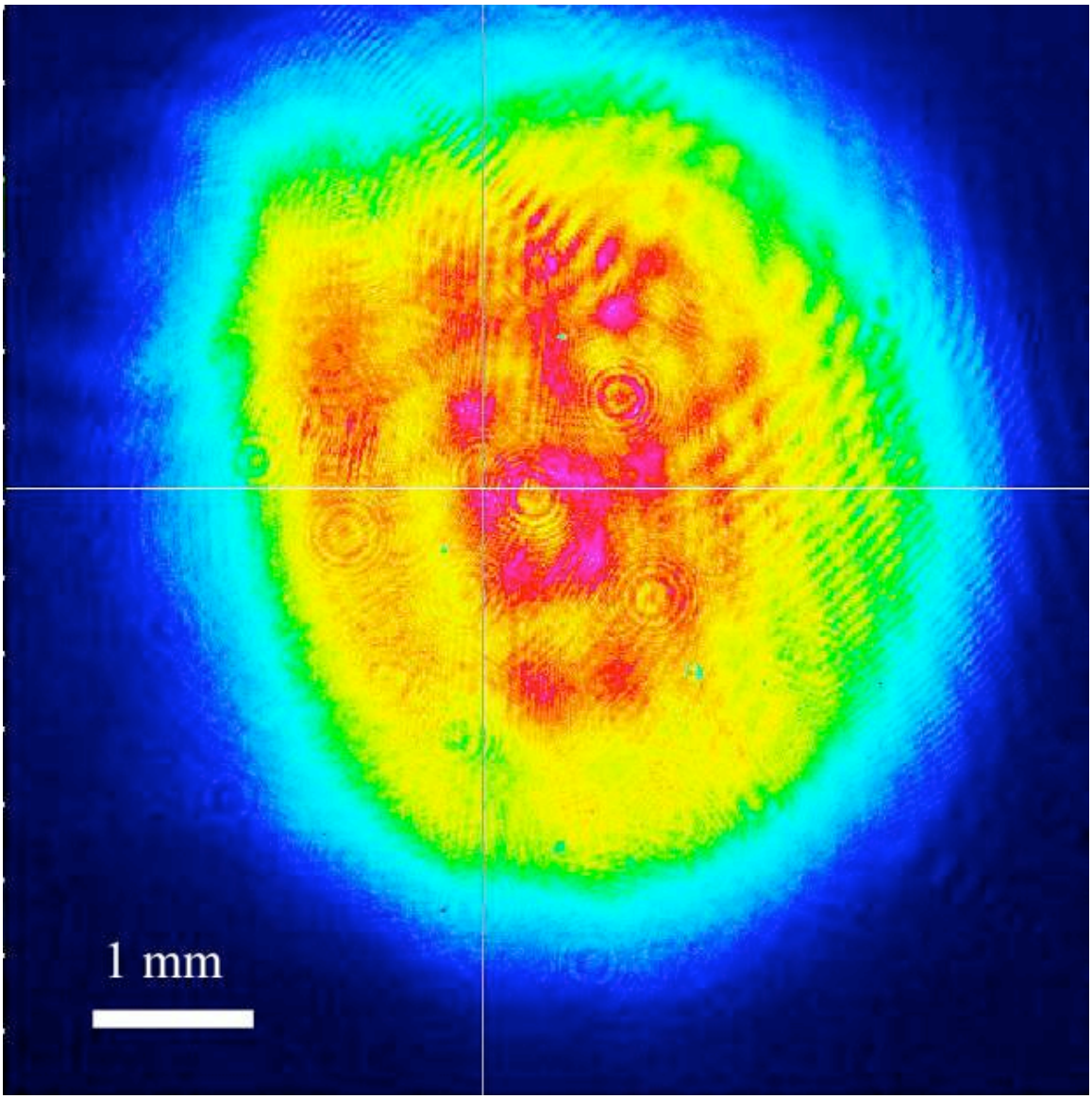

Figure 2.3: Typical near field spatial profile of the Surelite II-10

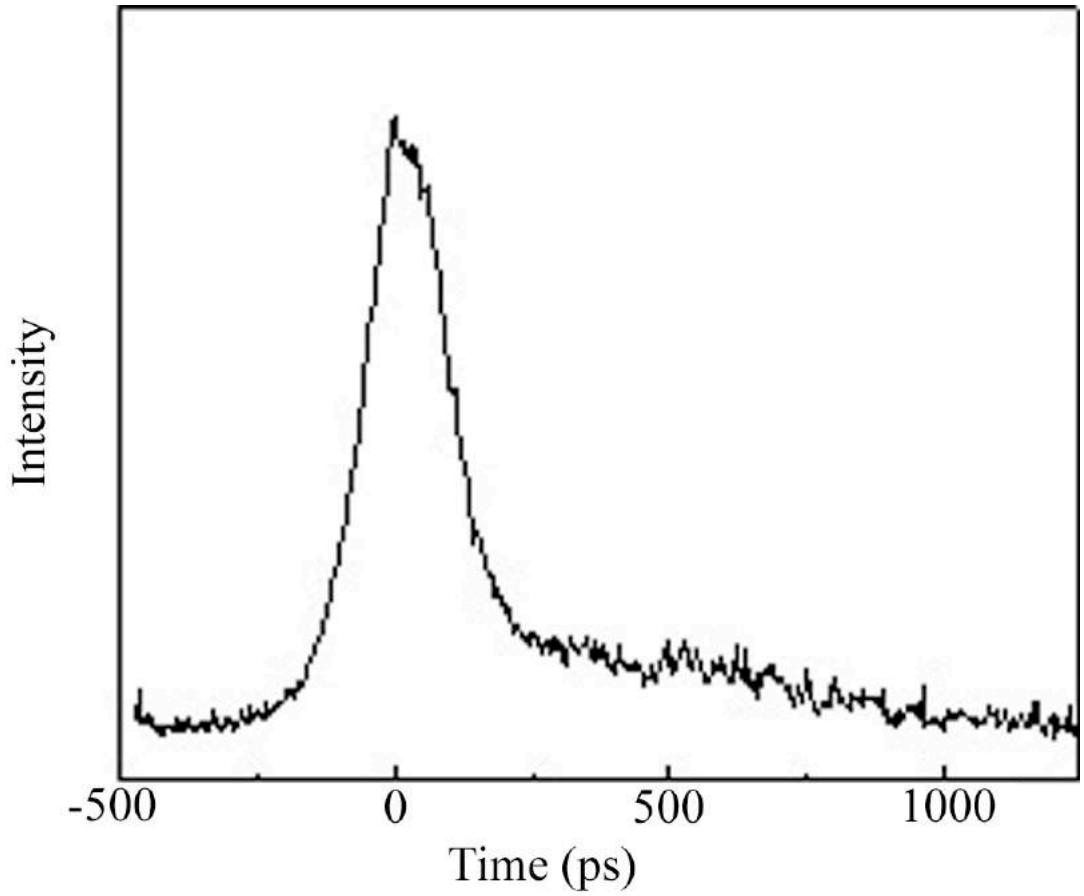

Figure 2.4: Factory measurement of SG355 minimum temporal pulse shape.

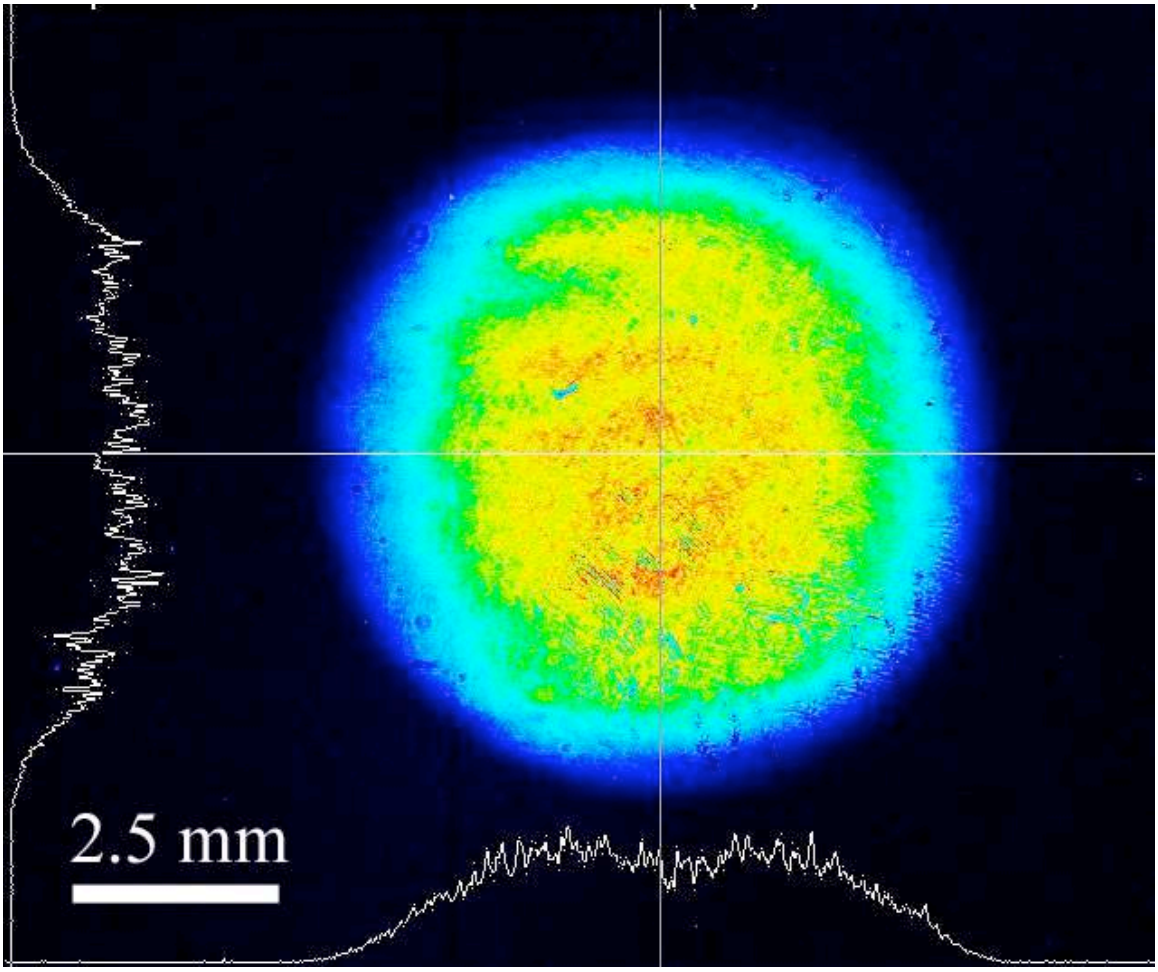

Figure 2.5: Near field spatial profile of the SL355

2.3. Plasma diagnostics

In this section the plasma diagnostics will be explained in detail. All diagnostics involving EUV measurements must be completely contained in vacuum conditions, since even small amounts of gas will absorb a significant portion of the light. Additionally all optics used for EUV measurements must be reflective, again because of absorption, adding a level of complexity to the diagnostics.

2.3.1. Electron Density Measurements

Optical interferometry yields a direct measurement of the electron density profile in regions well below the critical density (n_c). This technique records the phase shift induced in the probe beam as it passes from vacuum through the high density plasma. The information is recorded in an image, an interferogram, which can be processed into a 2-D density profile. The plasma density is related to the phase shift by,

$$\delta\phi(x,y) = \frac{2\pi}{\lambda}\int_0^L [n(x,y,z)-1]dz, \tag{2.1}$$

where,

$$n = (1 - n_e/n_c)^{1/2}, \tag{2.2}$$

is the refractive index of the plasma [27].

When probing a LPP it is important to take into consideration the refraction of the probe beam, due to the density gradient, as it passes through the plasma. A ray that begins parallel to the target surface will bend toward regions of low plasma density. This

introduces two effects on the interferogram. First the maximum density that can be measured is limited due to the limited collection angle of the imaging lens. The other effect determines the spatial resolution that can be obtained. Using the paraxial ray equation the angle of refraction can be calculated as,

$$\theta_r = L\left(\frac{n_e(z)}{n_c l_s}\right) \tag{2.3}$$

where L is the size of the plasma, and l_s is the plasma scale length, and the plasma density profile is given by [73],

$$n_e = n_0 \exp\left(\frac{-z}{l_s}\right). \tag{2.4}$$

The error due to refraction can be approximated as [27],

$$\sigma \approx L\theta_r . \tag{2.5}$$

Using reasonable values for the plasmas in this study, L=600 μm, and keeping the total error below 20 μm, the error due to refraction should be > 15 μm. With these values the maximum accessible electron density is $3.2\text{x}10^{19}$ cm^{-3} for a 532 nm probe beam assuming l_s=200 μm.

All interferometry in this work utilized a polarization scheme known as a Nomarski interferometer shown in Figure 2.6. The 532 nm laser energy from the EKSPLA laser, described earlier, is controlled with the combination of a λ/2 wave plate and a linear polarizer. Part of the beam then passes through the plasma, while the remaining beam continues unchanged. The probe beam is then imaged with an F/20 lens

on to a CCD camera. The CCD camera has a 6.7 μm by 6.7 μm pixel size in a 1280 by 1024 array with 16 bit dynamic range. A Wollaston prism and a linear polarizer are located between the lens and camera. The Wollaston prism splits the beam into two orthogonally polarized beams. The beams have a separation angle ϕ_w of 10 mrad, creating interference fringes. The fringe spacing is determined by,

$$\delta i = \frac{D}{b\phi_w}\lambda, \tag{2.6}$$

where D is the separation between the Wollaston prism and the CCD camera, and b is the distance from the focus of the lens to the Wollaston prism [27]. The magnification of the system is given by,

$$M = \frac{f + b + D}{f}, \tag{2.7}$$

where f is the focal length of the lens. A reasonable experimental arrangement for this work would be: b = 200 to 400 mm, b + D = 900 mm, and f = 100 mm. This makes M = 10, and δi = 7.5 – 15 μm in the target plane.

The phase shift is extracted from two images, a reference image taken before the laser pulse, and an image taken when the plasma is present (Figure 2.7). The images are then processed using a Fast Fourier Transform method into a two-dimensional phase shift map as described in [74]. The phase shift is converted to n_e by solving Equation (2.1). The equation is simplified by approximating the plasma as having a uniform density over some length, L, and then droping rapidly to zero as seen in Figure 2.8. The length, L, is taken to be the FWHM of the cross-section at each distance from the target surface, z. Additionally, there is a axis of symmetry that divides the length, L, in half.

Then Equation (2.1) becomes,

$$n_e = \frac{\delta\phi \, n_c \, \lambda}{\pi \, L} . \tag{2.8}$$

This method agrees well with the software package IDEA, which also uses a Fast Fourier Transform method as described by Hipp et al.[75], but the inversion of equation (2.1) is done numerically without the approximation in Equation (2.8). Additionally, the maximum electron density calculated from the interferograms using Equation (2.8) is around is 3.2×10^{19} cm^{-3} as predicted from combining Equation (2.3) and Equation (2.5).

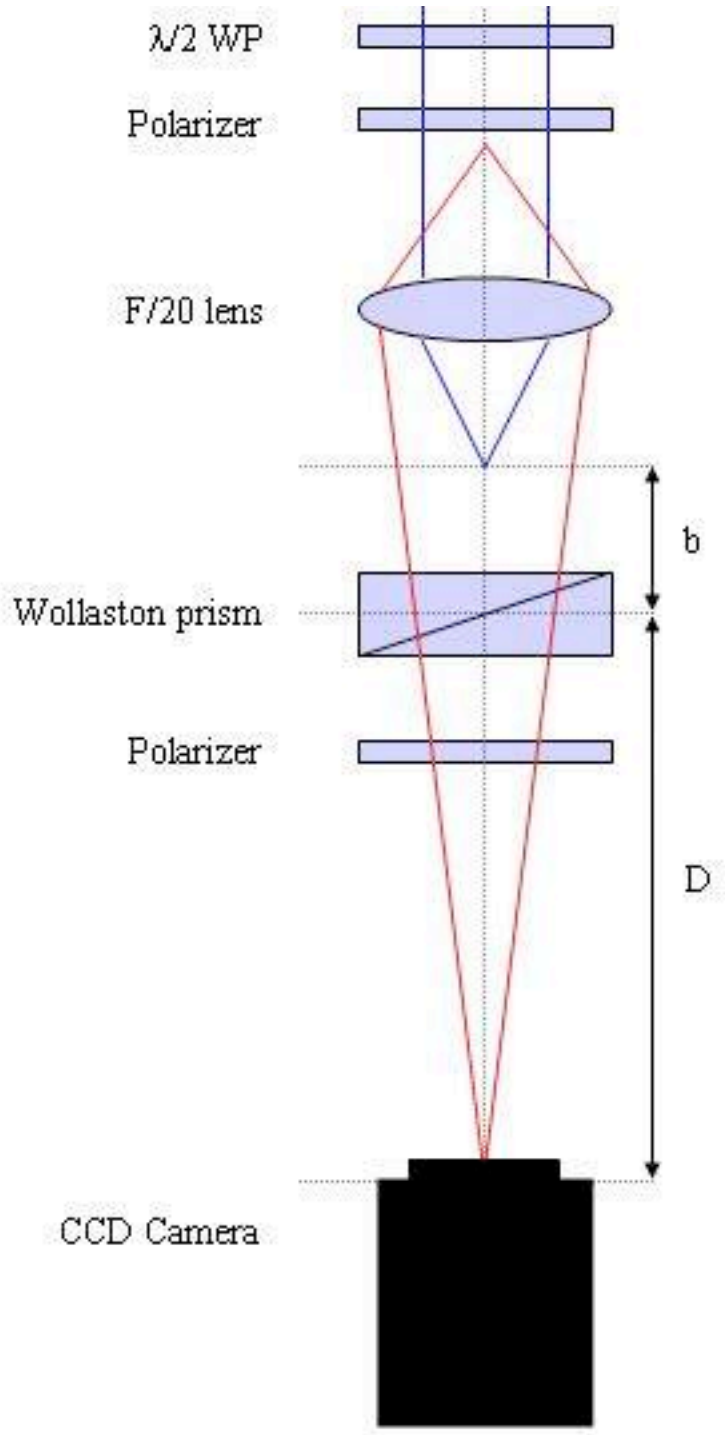

Figure 2.6: Optical layout of Nomarski polarization interferometer

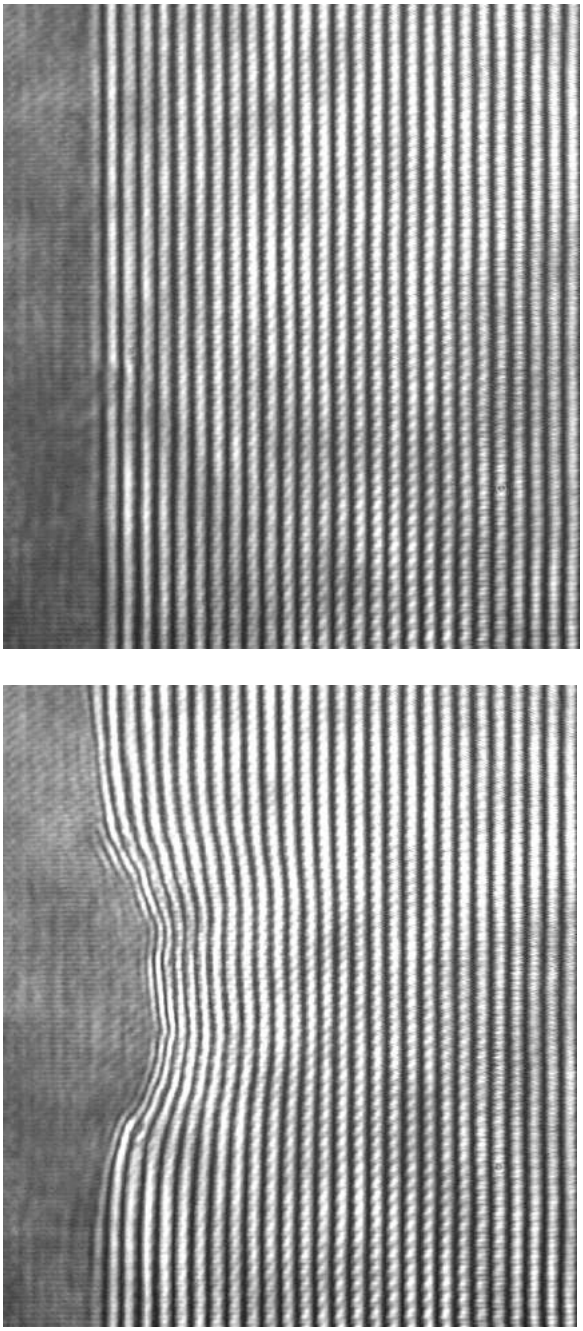

Figure 2.7: Reference image (Top), and interferogram (Bottom) produced with Nomarski interferometer.

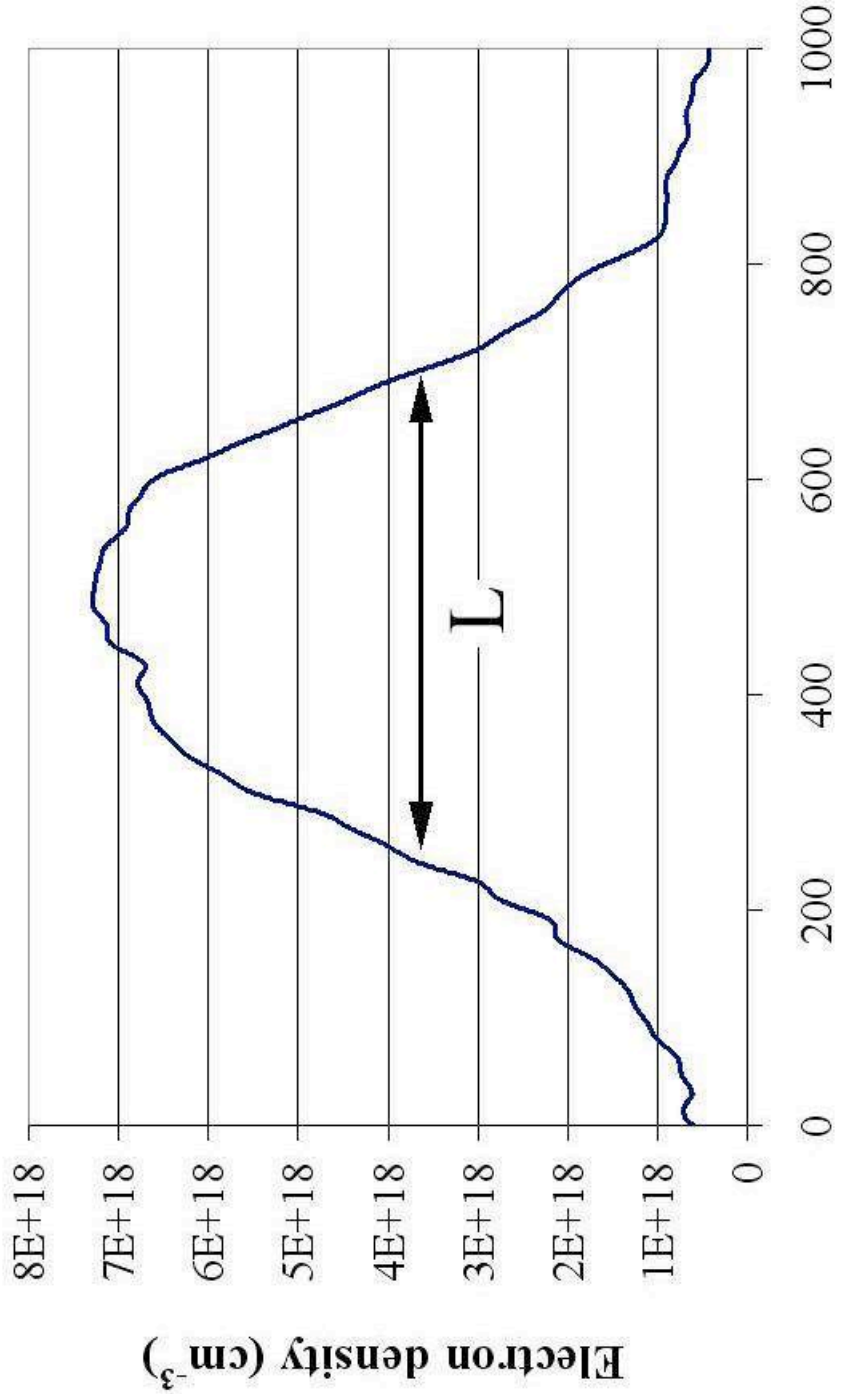

Figure 2.8: Typical temporal pulse shape of the Surelite II-10.

2.3.2. Transmission grating spectrometer

The transmission grating spectrometer (TGS) provides time integrated soft X-ray spectra from 5 – 20 nm, with $\lambda/\Delta\lambda \approx 160$. There are three main components of the TGS: the vacuum vessel and mount, the grating, and the CCD camera. The vacuum vessel and mount allow for in situ alignment and adjustment without risk to the grating, Figure 2.9. The grating is a 100 nm thick silicon nitride foil with 10,000 lines/mm. The detector is a PI-SX X-ray camera, sensitive to photons from <30 eV to ~ 10 keV. The sensor is an array of 1340 by 1300, 20 μm pixels, and is a thermoelectrically cooled, back-illuminated CCD with no AR Coating.

The spectral resolution of the TGS is determined by three factors: the source size, CCD pixel size, and the number of illuminated grooves on the grating. The resolution of the TGS is given by,

$$\Delta\lambda = \max\left(\Delta\lambda_{grooves}, \Delta\lambda_{pixel}, \Delta\lambda_{source}\right) \tag{2.9}$$

where $\Delta\lambda_{grooves}, \Delta\lambda_{pixel}$, and $\Delta\lambda_{source}$ are the resolution limits caused by the principle grating resolution, the image projection on to the CCD, and the divergence of the radiation from the source respectively. These limits are given by,

$$\frac{\lambda}{\Delta\lambda_{grooves}} \cong N_{grooves} = \frac{b_{grating}}{d} = \frac{1}{d} \cdot \left[s + \left(Q_{source} + s\right) \cdot \frac{L_{slit-grating}}{L_{source-slit}} \right], \tag{2.10}$$

$$\Delta\lambda_{pixel} = b_{pixel} \cdot \frac{d}{L_{grating-CCD}}, \tag{2.11}$$

and

$$\Delta\lambda_{source} = b_{source} \cdot \frac{d\lambda}{dx}, \tag{2.12}$$

where

$$b_{source} = s + \left(Q_{source} + s\right) \cdot \frac{L_{slit-CCD}}{L_{source-slit}}. \tag{2.13}$$

Here s is the slit size, $L_{x\text{-}y}$ is the distance from object x to object y, b_{source} is the size of the source, $b_{grating}$ is the size of the image on the grating, and b_{pixel} is the pixel size. The angular diffraction for a grating is given by,

$$\sin\varphi = m \cdot \frac{\lambda}{d}, m = 0,1,2,..., \tag{2.14}$$

where d is the period of the grating. The displacement x on the CCD of the wavelength λ depends on the angular diffraction and the distance between the grating and the CCD according to,

$$\frac{d\lambda}{dx} = \frac{d}{L_{grating-CCD}} \cdot \cos^3\varphi \cong \frac{d}{L_{grating-CCD}}, \tag{2.15}$$

for $\varphi < 15°$. The approximation is valid since in this work $\varphi = 7.76°$, d = 100 nm and λ = 13.5 nm. For the experiments in this work reasonable values are: d = 100 nm, s = 25 μm, Q = 100 μm, $L_{slit\text{-}groove}$ = 160 mm, $L_{source\text{-}slit}$ = 250 mm, $L_{grating\text{-}CCD}$ = 310 mm, and b_{pixel} = 20 μm, so that the TGS resolution is $\lambda/\Delta\lambda \approx 160$.

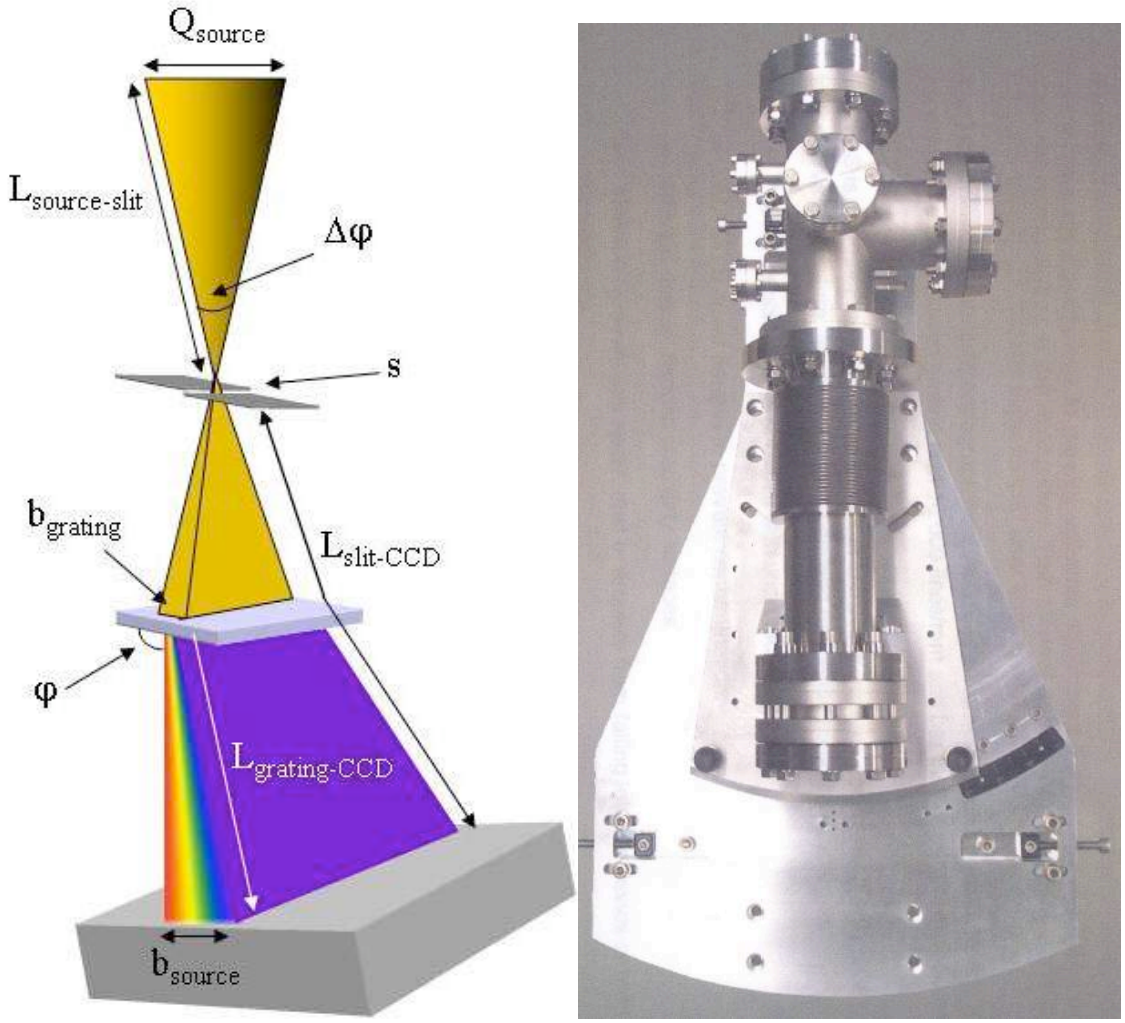

Figure 2.9: Vacuum vessel and mount for TGS (left) [76], and schematic of TGS (right)

2.3.3. In-band EUV energy monitor

The in-band EUV energy monitor (E-Mon) is an absolutely calibrated instrument composed of a filter, two multilayer mirrors, and a photo diode contained within a vacuum vessel, Figure 2.11. Emissions from the plasma in the chamber center enter the E-Mon through a vacuum flange at 45° with respect to the laser axis. The emitted spectrum will contain a wide range of photon energies including the visible photons. Light with wavelengths above 50 nm is filtered out by a 150 micron thick Si_3N_4/Zr filter. The filter aperture is 3.5 mm. About 10% of the light with wavelengths below 50 nm is transmitted through the filter to a pair of near normal incidence, 10°, multilayer Mo/Si mirrors with a narrow band reflectivity centered at 13.5 nm, see Figure 2.12. The second Mo/Si mirror reflects the in-band light to the photo diode. The detector is connected to a 500 MHz oscilloscope that integrates the diode signal, seen in Figure 2.10, yielding the detected photo charge, Q_{pulse}. Afterward the average background signal, of the order of 100 pVs, is subtracted from the total charge, around 20 nVs. The response time of the photo diode is much longer than the in-band emission, so all measurements with the E-mon are time integrated.

The in-band EUV energy per solid angle is given by,

$$E_{inband} = \frac{Q_{pulse}}{f_{calib}\Omega}, \tag{2.16}$$

where f_{calib} is a calibration factor in A/W, and Ω is the collection solid angle. The solid angle is calculated by,

$$\Omega = \frac{b_{Emon}^2}{4d_{Emon}^2} \tag{2.17}$$

where b_{Emon} is the aperture size at the Zr filter, and d_{Emon} is the distance from the plasma to the aperture.

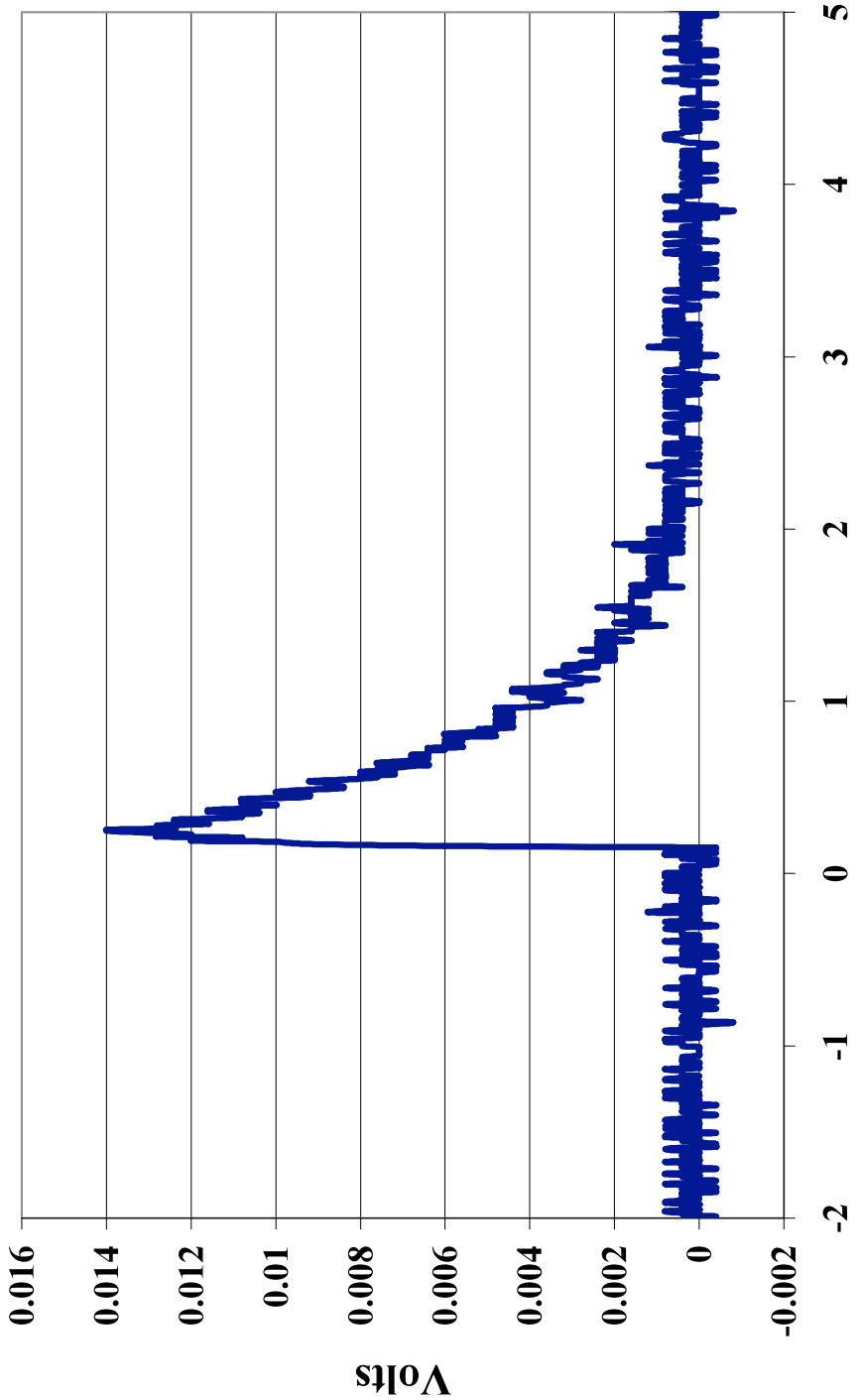

Figure 2.10: Typical signal from E-Mon

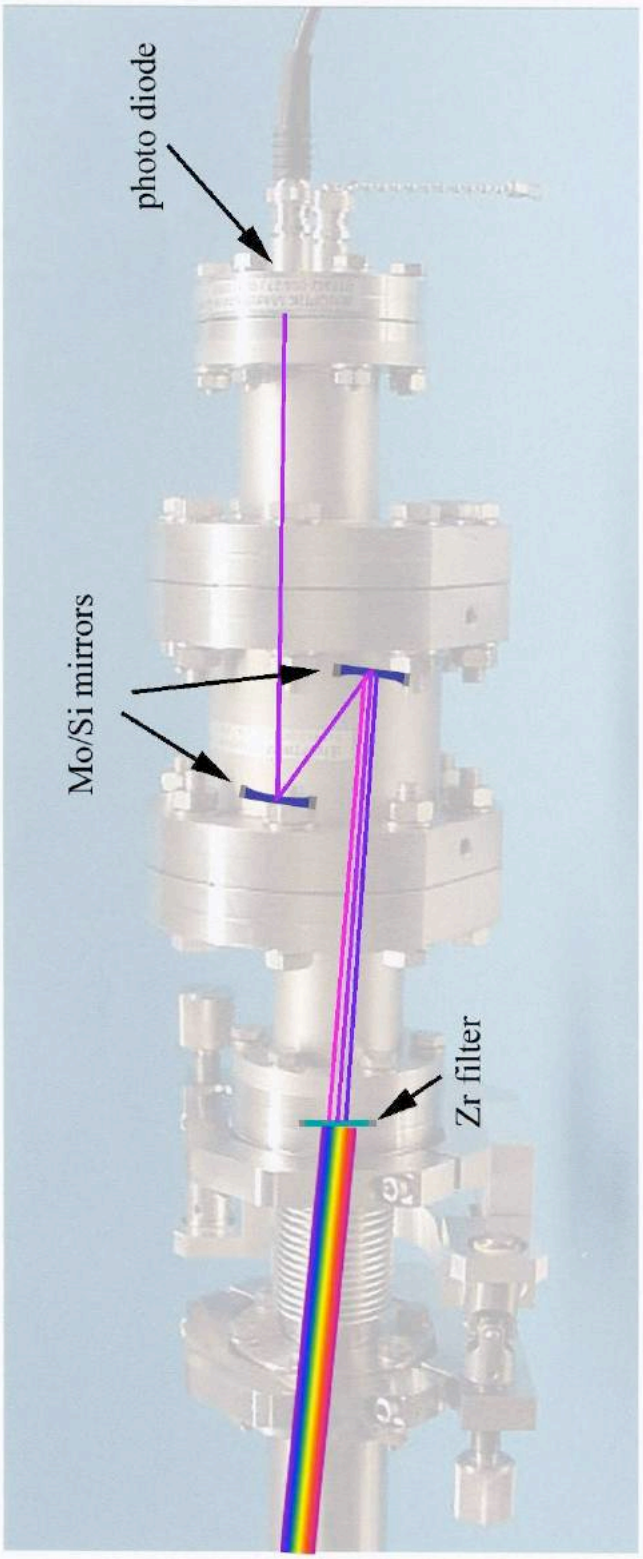

Figure 2.11: Optical path for the absolutely calibrated energy monitor (E-Mon).

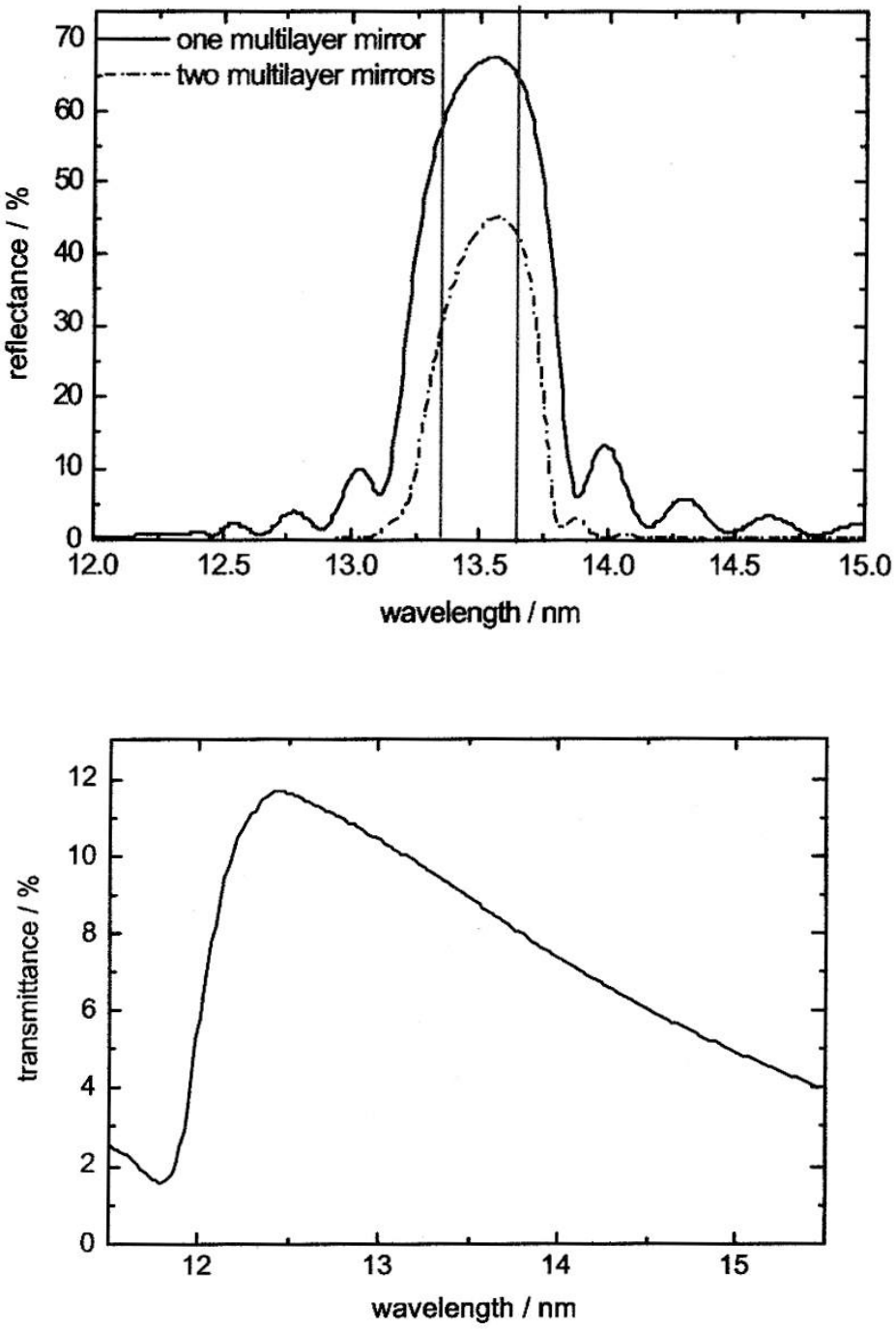

Figure 2.12: Reflectance of multilayer Mo/Si mirrors (top), and transmittance of Si_3N_4/Zr filter (bottom) from [77].

2.3.4. EUV Imaging

A schematic of the EUV imaging diagnostic setup can be seen in Figure 2.13. The imaging system shares the same camera, PI-SX X-ray camera, as the spectrometer. A ½ inch, concave, multilayer Mo/Si mirror with a 100 mm focal length is positioned ~11.5 cm from and perpendicular to the target surface. The mirror is positioned so that the plasma is imaged onto the CCD camera. An acrylic box lined with black material is placed over the mirror to reduce scattered light. Two holes in the front of the box act as an entrance and exit aperture. The entrance is covered by a Zr filter, which filters the visible light from the plasma. The exit hole is covered with several pieces of lens paper which act as attenuation filters for the EUV light in order to prevent saturation of the CCD camera. A black tube is placed between the camera port and the exit hole again to reduce scattered light.

The image magnification is calibrated using a 180 μm wire at the chamber center. The wire is back illuminated using a HeNe laser and imaged on the CCD through the EUV mirror. The Zr filter must be removed during this process. The wire can then be used as a reference to determine the proper scale of the plasma. The wire also provides a means of focusing the system without producing a plasma. The image resolution is around 5 μm, based on a 180 μm wire covering 42 pixels.

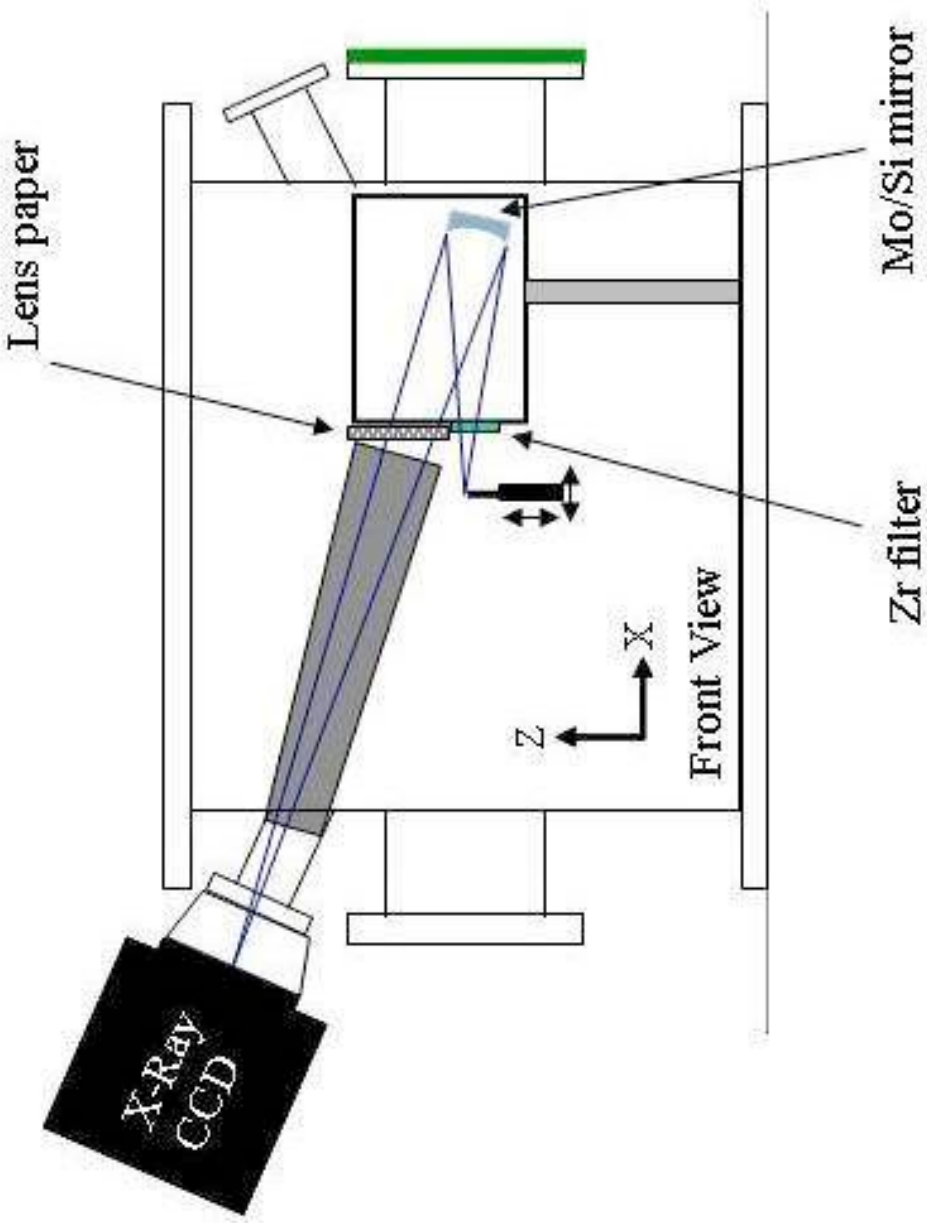

Figure 2.13: Schematic of EUV imaging system

2.3.5. Time resolved in-band EUV measurements

Time resolved in-band EUV measurements were made in much the same way as the E-Mon described in section 2.3.3. A multilayer Mo/Si mirror is place at a 45° angle with respect to the pump laser at a near normal incidence as shown in Figure 2.14. The reflected light is focused on to a photo diode with a rise time of 0.4 ns. Mounted in front of the photo diode is a filter used to eliminate light above 50 nm. The diode was connected to the same 500 MHz oscilloscope as the diode monitoring the laser pulse duration, so that the temporal evolution of the in-band EUV could be measured simultaneously with the laser pulse.

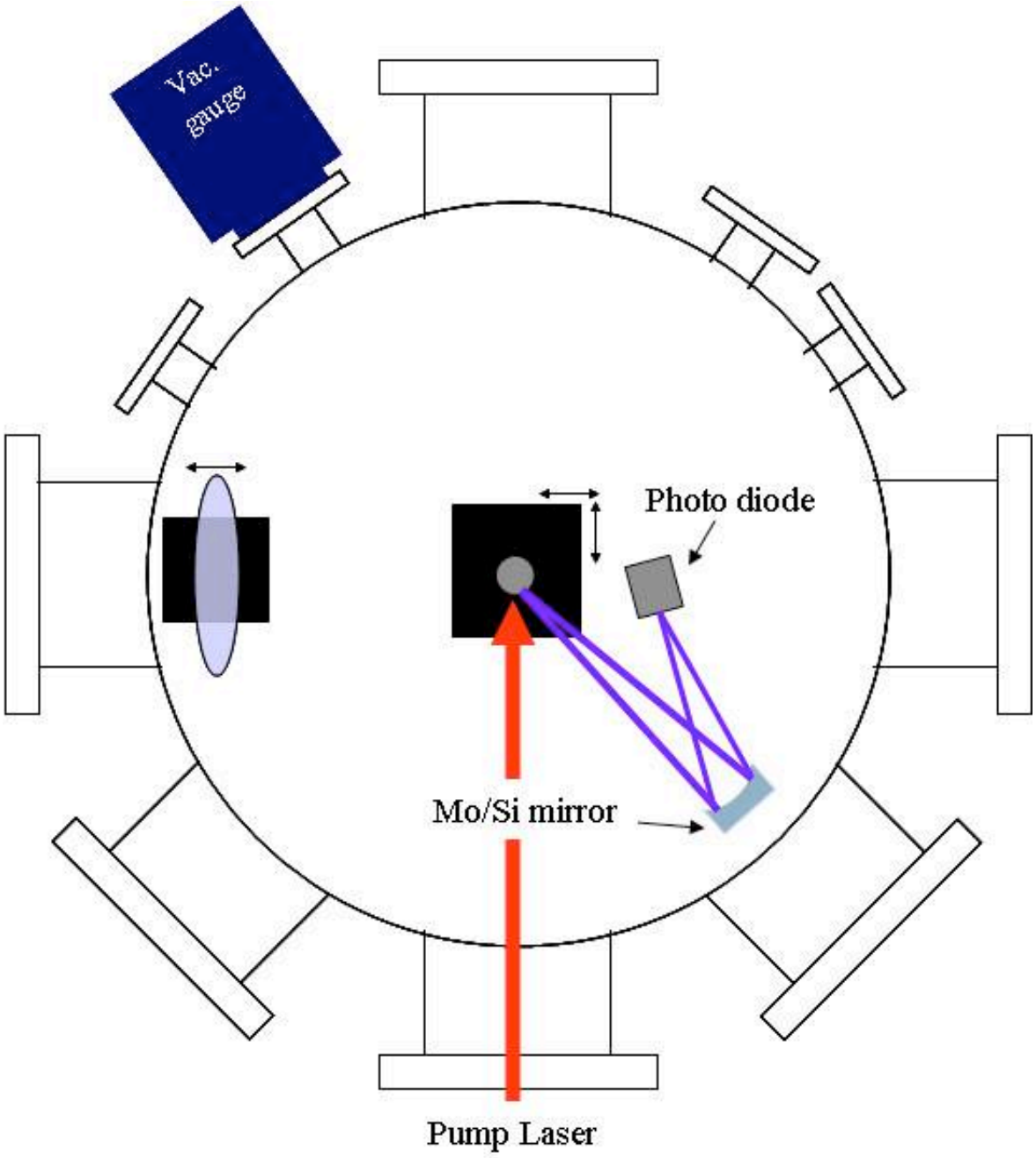

Figure 2.14: Schematic of the in-band EUV temporal diagnostic.

2.4. Target description and engagement

2.4.1. Target description

All targets used in this work are made of 99.9% pure or purer Sn. As discussed in earlier chapters Sn is the material of choice for radiating 13.5 nm. Using pure Sn is important as any contaminants could increase the absorption of the in-band radiation, lower the heating efficiency of the Sn, or lead to the production of unwanted high energy ions. The high energy ions are a concern for HVM since they could lead to damage of the collecting optic. There are two primary target types studied in this work, planar and spherical.

The planar targets come in two forms. The first is a solid, fully dense slab of tin which is several mm thick. The slab is sliced into several long pieces several mm wide. If the slab is too wide, it is difficult to acquire a clean density profile. Wide targets tend to shadow the image of the plasma since it is extremely difficult to place the target perfectly normal to the probe beam. The surface is prepared with a metal file to remove any pits or scratches that might affect the plasma expansion. Targets that have already been shot are reused after reconditioning the surface.

The other planar target consists of a glass microscope slide coated with at least 2 μm of Sn. The slides are sputter coated using a 99.999% Sn target. The Sn thickness is measured using a stylus profiler. Results comparing the different types of planar targets can be seen in chapter 4. These targets are shot once per location as most of the Sn is removed from the surface after one shot.

Spherical targets are produced in the same manner as the coated slide targets. Glass beads ranging in size from 150 to 350 μm, are sputter coated with pure Sn. The spheres are contained in a small dish during the coating process so that they can be removed from the sputter chamber periodically and shaken. The spheres undergo four rounds of coating and shaking to ensure uniform coating thickness. The coating thickness is estimated based on the thickness of Sn on a slab target that remains in the sputter chamber for the entire process. The thickness of Sn on the sphere should be more than half the thickness of the Sn on the slide, since the sputtering process coats more than half the sphere surface each round. Targets of the proper size can then be selected during the mounting process. Examples of the spherical targets can be seen in Figure 2.15.

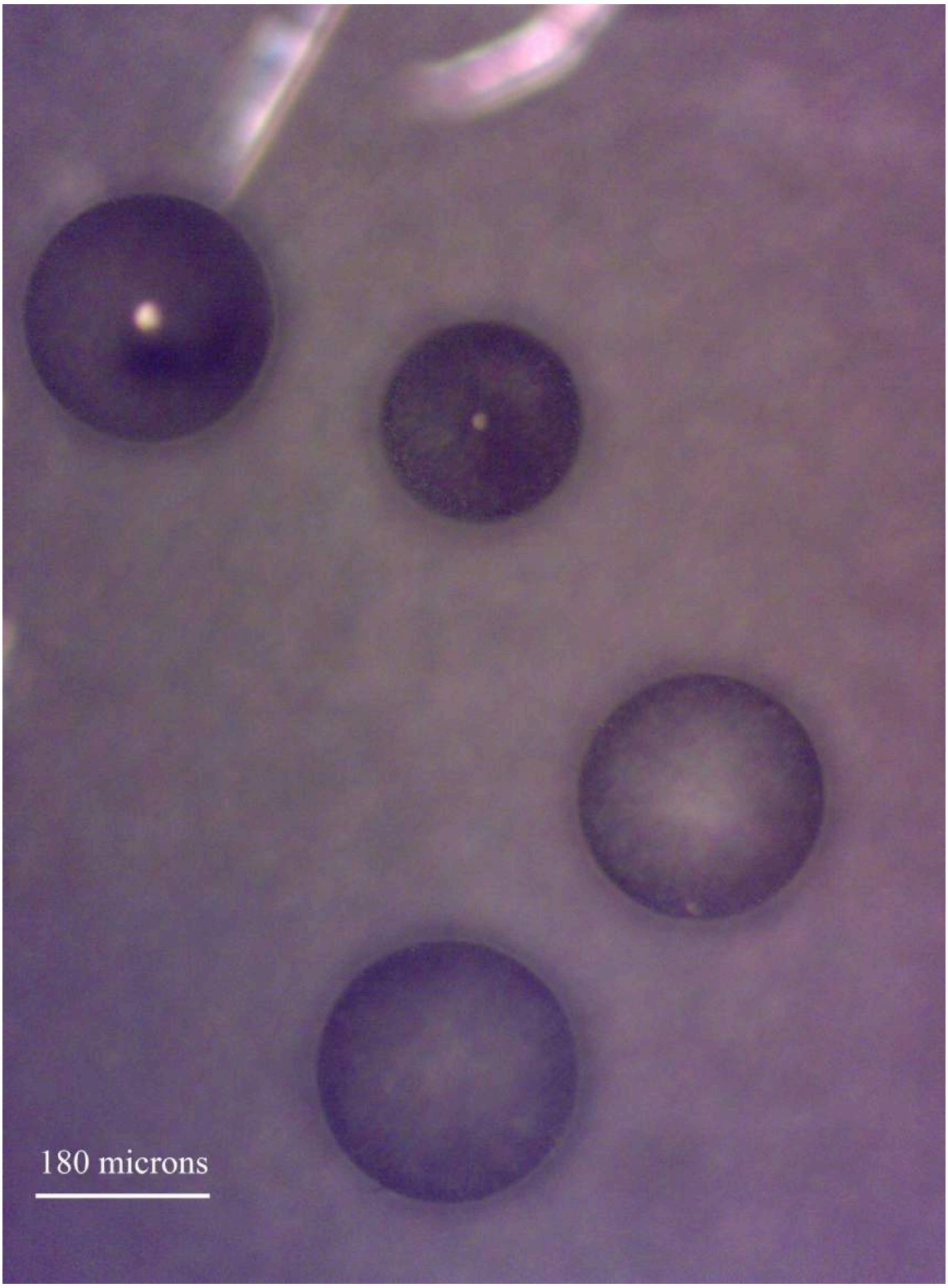

Figure 2.15: 99.999% pure Sn coated glass beads used for spherical targets.

2.4.2. Target Engagement

One of the most important considerations in any laser experiment is proper beam alignment. This is especially true when the target and the focal spot are of the same scale. A misalignment, as little as a few tens of microns, makes the difference between a properly acquired data point and a wasted shot. This section will reveal the details of beam alignment, target alignment, and target mounting.

First the laser beam must be focused to the proper size at the proper location in the chamber. Since the plasma diagnostics are directed toward the center of the vacuum chamber, the laser must also focus to the center of the chamber. The pump laser beam path is set on the optical table as seen in Figure 2.1, but without the lenses. The beam is directed through the front window of the vacuum chamber, passes through the center, and exits the rear window. Thin sewing thread is used to make a crosshair on the front and rear window. The thread is wrapped around the equally spaced flange screws making the intersection the center of the window. A CCD camera is placed after the rear window so that the shadows of the crosshairs are visible on a monitor. Adjustments are made to the final steering mirror until the beam passes through the center of both windows. This is achieved when the center of each crosshair is aligned in the center of the laser beam shown in

Figure 2.16. The same process is followed for the probe laser beam except now the beam is entering the left side window and exiting the right side window. This process determines the center of the camber to at best a few hundred μm and at worst around a mm.

Now that the lasers are passing roughly through the center of the chamber the position must be marked. A 180 μm wire is mounted onto the three-axis translation stage inside the chamber. The tip of the wire is positioned at the center of each beam indicated by the crosshairs. The wire tip now serves as the chamber center location.

At this point the optic required for Nomarski interferometry can be installed. This will serve a dual purpose as a plasma diagnostic and the first target monitor. The imaging lens is installed first by ensuring that the beam continues to pass through the center of the crosshairs. Then the other optics can be installed and the image of the wire tip is focused onto the CCD camera. The wire position is double checked with the pump beam to ensure that it did not move while the lens was being installed. The position of the wire tip can then be marked with a crosshair on the interferogram as shown in Figure 2.16. Once the tip is marked on the monitor the Y and Z coordinates are established to better than 10 μm. The X coordinate is still roughly marked to within about 200 μm, by the focus of the image.

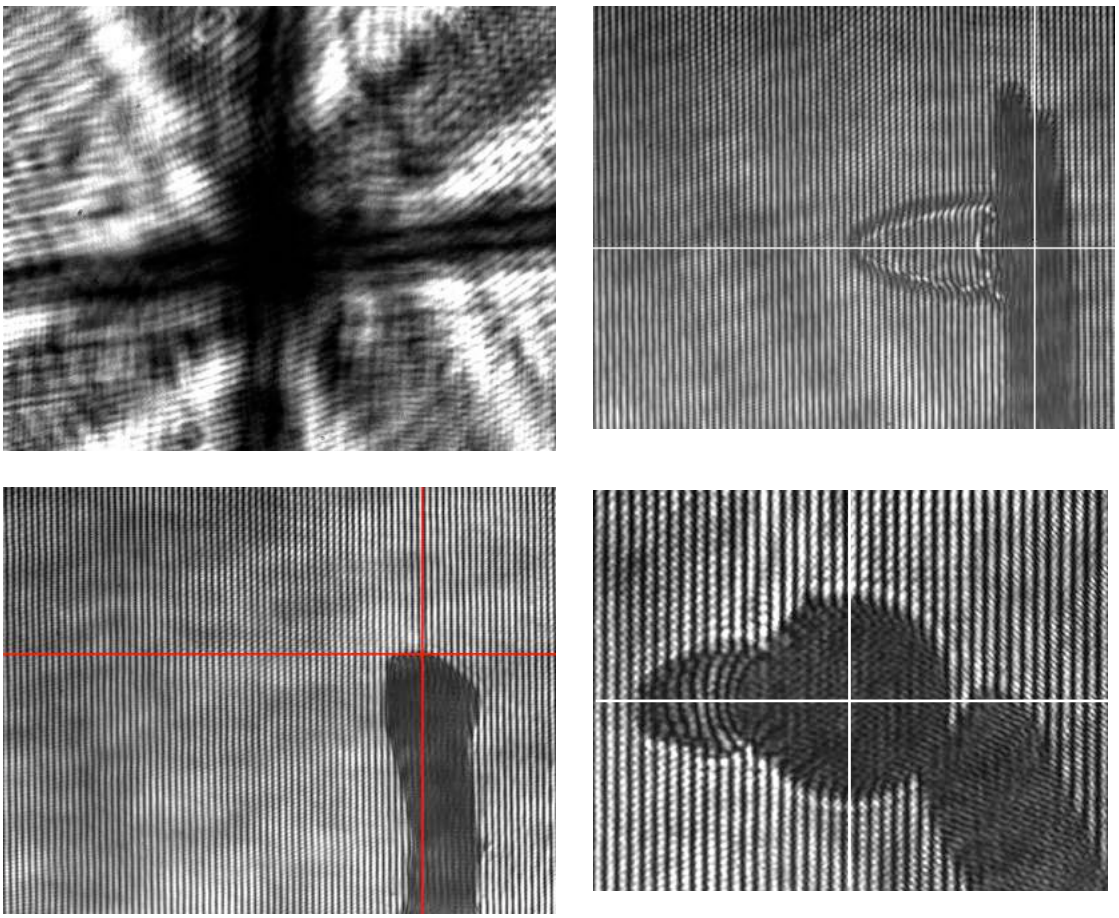

Figure 2.16: Shadows of crosshairs for aligning the pump beam to the center of the chamber (top left), wire marking center of chamber (bottom left), adjusting the X axis alignment by maximizing the length of the shockwave (top right), demonstration of alignment by shooting a spherical target at atmospheric pressure (bottom right).

Now the pump laser focusing lens, referred to as primary focusing lens from here forward, can be installed. The primary focusing lens is mounted on a translation stage so that the focal spot size can be changed without dramatically affecting the alignment. The laser energy is reduced to a minimum by adjusting the ½-waveplate, to a few mJ, and the primary focusing lens is aligned to the center of the front window. It should be noted that any change to the laser operations such as timing of the Q-switch, operating voltages, or repetition rate will cause a change in beam pointing and divergence. The alignment must be rechecked and the spot size re-measured if any of the laser operating conditions change. When the alignment is just right the laser focuses onto the wire tip, and a shockwave can be seen on the interferogram. The wire tip is raised so that the tip is above the Z axis on the interferogram. The fine adjustment on the primary focusing lens is then made so that the shockwave is symmetric about the Z axis as seen in Figure 2.16. The wire is translated along the X axis until the shockwave reaches its maximum length. This centers the laser beam on the wire to within a few tens of μm. The wire tip is again placed at the focal position to mark the final chamber center location.

Before an X axis monitor can be implemented, the laser spot size must be measured and adjusted as needed. Again the laser is kept at minimum energy by using a polarizing cube and ½-waveplate. A 100 mm lens is mounted between the wire and the rear window on a translation stage. The beam passes through the center of the lens and is imaged on a CCD camera as depicted in Figure 2.1. The primary focusing lens is translated so that the beam is much larger than the wire at the chamber center. The shadow of the wire is used to calibrate the magnification of the image. Figure 2.17 shows a shadowgram of the 180 μm wire. It is important that care is taken to get the wire into

best focus before the spot is measured. This establishes a focal plane at a known location. The wire is translated along the X axis until the beam can pass freely, and the lens is adjusted until the desired beam size is realized. The beam size is measured as the $1/e^2$ width, and can be seen in Figure 2.17. Once the beam size is fixed, the wire is translated back to the center of the beam, again looking for the maximum shockwave length. This time the X position is confirmed by the focal spot image showing the wire in the center of the beam.

With the wire in the correct location and the spot size known the X axis monitor can now be implemented. A HeNe laser is mounted to point at the wire tip from the upper front port of the chamber to act as a backlighter as shown in Figure 2.18. The HeNe is expanded using a 30 mm focal length lens and a mirror is positioned after the wire and below the pump laser axis to direct the beam to a CCD camera. A 100 mm focal length lens is used to image the wire onto the CCD camera. Again a crosshair is used on the monitor to mark the wire tip, establishing a precision marker for the X axis and a second marker for the Z axis. This monitor also gives a rough Y axis alignment in the same way as the as the interferogram gives a rough X axis alignment.

Now that the position is fixed for the target location the E-Mon and TGS can be fine tuned. A Sn slab target is mounted in the chamber and aligned to the proper location. The diagnostics are fine tuned until the maximum signal is reached with each instrument. Once this procedure is performed, the target location can move several tens of microns without significant change in signal strength. However, it is best to always keep the target location fixed in the chamber.

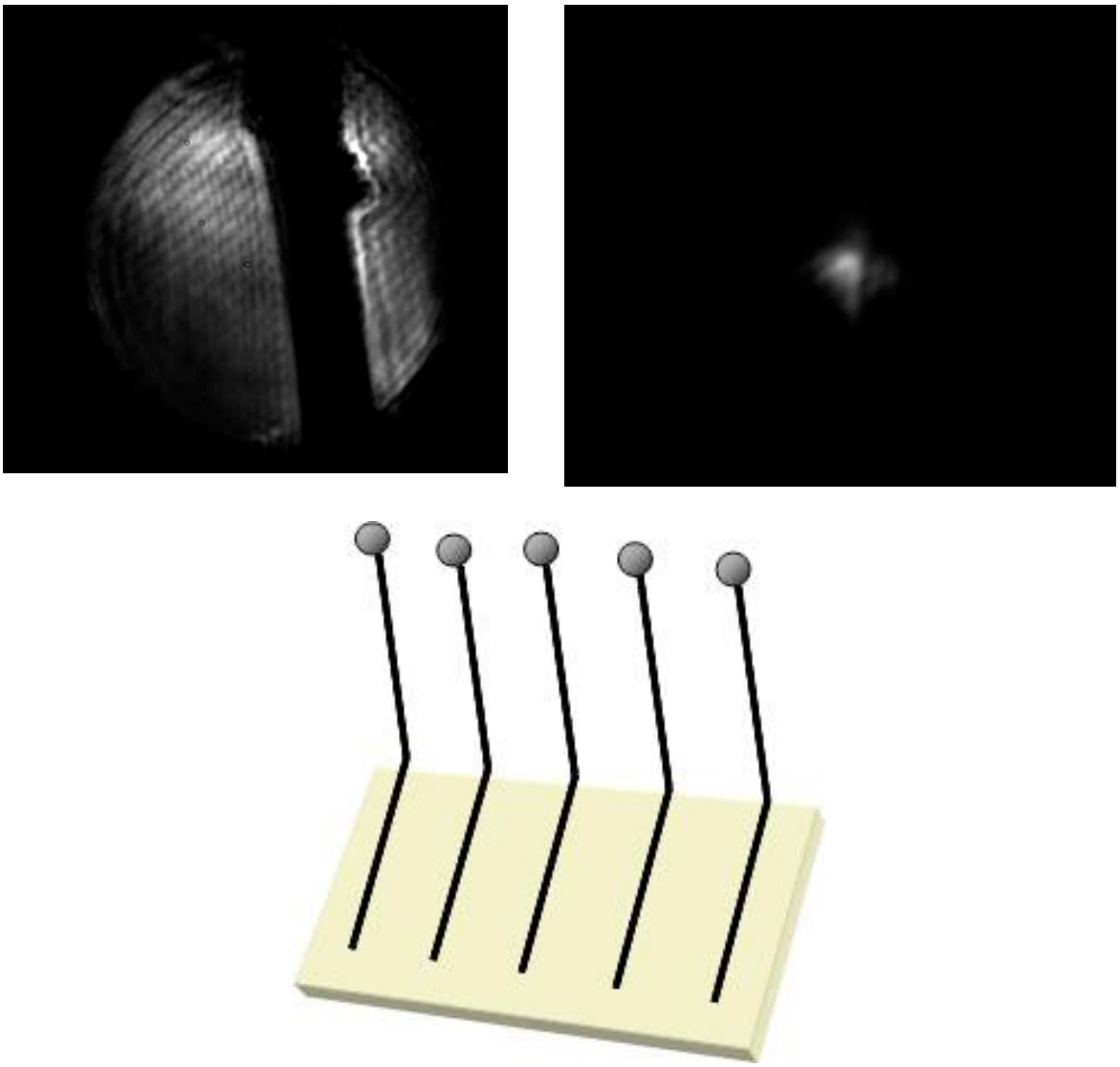

Figure 2.17: 180 micron wire used for calculating the magnification for focal spot imaging (top left), focused laser spot (top right), schematic of the spherical target holder (bottom).

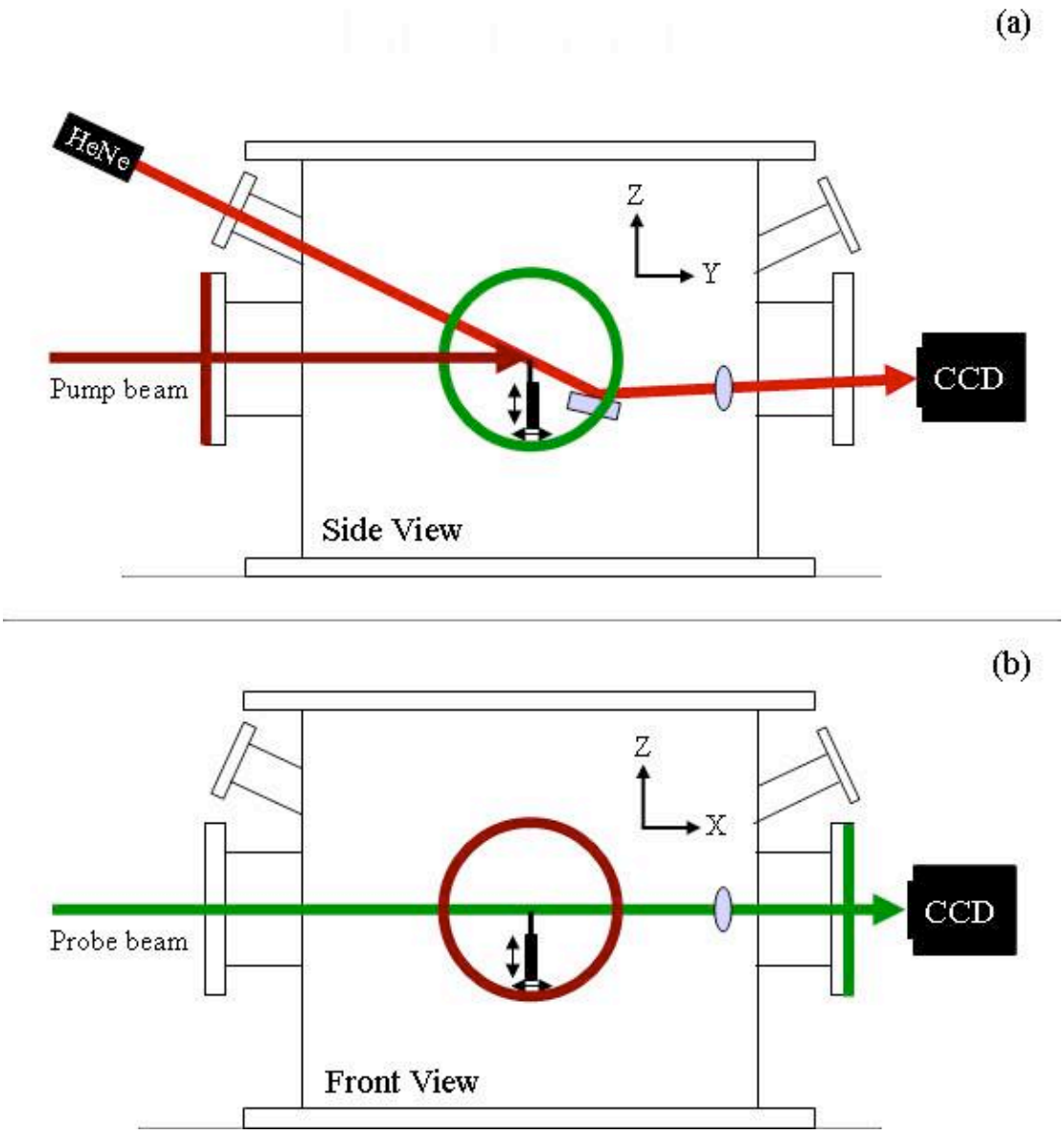

Figure 2.18: Schematic of target monitoring system

The final step in target engagement is to mount the targets in the chamber. For planar targets, this is simple. Double sticky tape is applied to the three axis stage in the chamber. Then planar target is simple placed directly on the stage. The target is then aligned to the crosshairs on the two target monitors. It is necessary, however, to translate the target along the X axis until the target is in sharp focus on the interferogram. In other words, only one edge of the target can be utilized since it is difficult to make the target perfectly flat. If the wrong edge is used the target will make a shadow on the interferogram which hides the plasma close to the surface.

Spherical targets require a bit more care in mounting than planar targets. A target holder is fashioned out of five pieces of 180 μm wire about 1 cm long. The pieces are taped side by side like fingers on a hand to form a wire array as seen in Figure 2.17. The wires are bent out of the plane of the tape by about 45° for alignment purposes. A dish containing many thousands of Sn coated spheres is places under a 10x microscope. Glue is added to the wire array by poking the tips of the wires into a glue stick. The spherical targets can then be hand selected one by one under the microscope by touching them with the end of the wires. The wire array is then mounted in the chamber in the same way as the planar targets. The spheres are aligned when centered on both crosshairs on the target monitors.

3. Numerical modeling

Numerical modeling plays a key role in understanding the complex processes in the evolution of a laser-produced plasma. There is not currently a single code publicly available that can accurately predict the hydrodynamic motion of the plasma while simultaneously solving for the radiation field including the relevant bound-bound transitions for a high-Z material. Because of the complexity of the present problem the numerical modeling is carried out with two separate codes. In this chapter a brief description of the codes implemented in this work will be covered along with a discussion of the limitations of these models.

3.1. h2d

The first part of the numerical problem that must be solved is the hydrodynamic motion of the plasma and the determination of the plasma properties (i.e. temperature and density). h2d is a two-dimensional version of the radiation hydrodynamic code Hyades [78]. It was developed with the purpose of providing experimentalist with an easy to use tool to model experiments where dense plasma is driven by an intense energy source. It is formulated using simple yet accurate approximations to the relevant physics models. However, it can not provide any information about the UTA responsible for the in-band emission which is of key importance for this work.

3.1.1. Hydrodynamics

The hydrodynamic motion of the plasma is the paramount physics package in h2d. All other packages such as thermal energy transport, ionization, and radiation transfer are coupled to the hydrodynamic package as a source term. The ultimate goal is to describe the fluid motion at any instant in time, and how applied forces affect this motion. The most precise method of these types of calculations would involve many equations relating the interactions between particles. This would take extreme computing power not readily available at the current time. Instead a fluid model is implemented with the primary concern being the macroscopic properties of the flow from a continuum point of view.

The coordinate system of choice here is Lagrangean. In a Lagrangean system the computational mesh moves with the fluid element such that the mass of any given zone does not change with time. This simplifies the computational process by eliminating the need to track the flow of mass into and out of a zone. In other words in the Lagrangean system the convective term of the Eulerian system is transformed away so that the conservation of mass and momentum equations become,

$$\frac{\partial \rho}{\partial t} + \rho \nabla \cdot \vec{u} = 0, \tag{3.1}$$

and

$$\rho \frac{\partial \vec{u}}{\partial t} = -\nabla P + \vec{f}. \tag{3.2}$$

Here ρ, $\vec{u}$, P, and $\vec{f}$ are the fluid mass density, the fluid velocity, the fluid hydrostatic pressure, and a body force respectively.

The Lagrangean coordinate system provides an advantage when the fluid experiences a shock, when the mass changes over several orders of magnitude, and when interfaces between fluids with different thermodynamic properties are present. The disadvantage of a Lagrangean system is that when mass diffusion takes place at material interfaces or when the flow patterns are highly distorted, such as when turbulence is present, this system does not work well.

The electrons, ions, and photons are treated as separate fluids that interact to produce the hydrodynamic motion of the material. The ions are coupled to the electrons by collisions where the electrons impart energy onto the ions. The electrons and ions are considered a perfect gas with Maxwellian distributions. The electron fluid gains and loses energy by interactions with the photons.

The problem time step is predominately controlled by the Courant condition. The Courant condition limits the maximum time step so that any disturbance in a zone can not travel more than the width of the zone in a single time step. If the time step were longer than that allowed by the Courant condition sound waves would travel slower than the sound speed.

3.1.2. Laser absorption

Laser absorption in the under dense plasma is calculated via the classical inverse Bremsstrahlung absorption model. The absorption coefficient is prescribed in h2d according to,

$$\alpha_{IBA} = 9.75641\times10^{-12} \times XLIBAM \times \frac{\left\langle n_i \left(Z^*\right)^2 \right\rangle n_e}{T_e^{3/2}\omega_0^2\sqrt{\varepsilon'}} \ln\Lambda \,, \qquad (3.3)$$

where ω_0 is the laser frequency, and ε is the complex dielectric function. The factor XLIBAM is a user defined constant and is set to the default value of 1 for this work. Once the laser reaches the critical density it is reflected back through the plasma and is again absorbed via inverse Bremsstrahlung. The non-linear (intensity-dependent) Langdon effect is not accounted for in the model, and is not important since the laser intensity is well below the 10^{16} W/cm^2 range where this effect begins to be important.

3.1.3. Radiation transport

Radiation transport is one of the key mechanisms for energy transfer in hot dense plasmas. Unfortunately, the treatment of radiative processes is a very complex problem involving the production, transport, and absorption of the photons. In h2d the treatment of the radiation as a fluid of photons allows for a kinetic theory to be applied. The assumption here is that the volume element is much larger than the wavelength of the photons, and that the photon density is high enough so that averages of their properties may be formed. Here only processes that contribute significantly to the hydrodynamic motion will be addressed. Bound-bound transitions would make the computation overly complicated and are not considered. The most fundamental assumption here is that the plasma is near a state of thermodynamic equilibrium so that the radiation field does not significantly differ from a Planck distribution.

The transport of radiation within the plasma is modeled via an equilibrium diffusion approximation. The radiation field is discretized by frequency into a finite number of groups. The photons within a group are treated the same so that average properties of the group are used for the interactions. The opacities of the groups are derived from the Los Alamos National Laboratory T4 SESAME tables. Additionally, the photon flux must be limited when the photon mean free path becomes large compared to the plasma scale length. Otherwise the flux out of an optically thin zone may exceed the energy density times the speed of light.

3.1.4. Atomic physics and ionization

The atomic physics package influences the hydrodynamic simulation in many ways in that the material pressures and energy are determined by the ionization of the plasma. The temperature and density are the key factors that determine the ionization level, and these quantities can vary by several orders of magnitude within the problem. For this reason a sophisticated model must be developed. When the density is high, collisional processes will dominate, and the atomic physics model should agree with Saha-Boltzmann equilibrium. However, in the limit of very low density the package should correspond to the coronal model where radiative spontaneous emission is the dominant process.

In a typical plasma composed of a mid to high Z material there will be a mixture of ions with different levels of ionization. To track the ionization level of every atom would be huge computational undertaking. Instead an average-atom model is implemented where the atoms in a given fluid element are considered to have identical

charge states equal to the average of the states that would be present using an exact calculation. The average-atom model implements a screened hydrogenic model to calculate the energy-levels. The approximate shell populations are based on the rate of change in population of a state n and is given by,

$$\frac{dP_n}{dt} = A_n Q_n - B_n P_n , \tag{3.4}$$

where A_n is the coefficient for the addition of electrons, Q_n is the availability for electrons to be added to the state n, B_n is the coefficient for the removal of electrons, and P_n is the shell degeneracy. The code also makes corrections to account for dense plasma effects.

In the work presented here the ionization model assumes local thermodynamic equilibrium (LTE). LTE is achieved when the distribution of particles can be described by a single temperature and the radiation field can be expressed by that same temperature. In addition the temperature and density gradients must be small compared to the mean-free-paths associated with the relevant physical processes, and the rate of change of the temperature and density must be small compared to the relaxation time.

3.1.5. Electron thermal conduction

h2d implements a flux-limited Spitzer-Härm electron thermal conduction model. The classical Spitzer heat flux is given by,

$$\vec{q}_e = -\chi_e \nabla k T_e , \tag{3.5}$$

where $\vec{q}_e$ is the heat flux, and χ_e is the thermal conductivity of the electron fluid and is given by,

$$\chi_e = \frac{\pi e^2 \overline{Z}^2 m^{1/2}}{(kT_e)^{3/2}} \ln \Lambda , \tag{3.6}$$

where $\ln \Lambda$ is the Coulomb logarithm [79]. Here the underlying assumption is that there are no steep temperature gradients. As mentioned previously one of the characteristics of a LPP is steep gradients. We must now define what is meant by steep temperature gradients. First the electron temperature scale length is defined by,

$$L_{Te} \equiv T_e / \nabla T_e , \tag{3.7}$$

If this scale length is shorter than the electron mean free path,

$$\lambda_{mfp} = 1/n_e \sigma , \tag{3.8}$$

here σ is the collision cross section, then the thermal energy transport given by Equation (2.1) can exceed the free streaming flux. A common method of accounting for this effect is to adopt a flux-limited model where the heat flux is now given by,

$$q_e^{fs} = -f_e^{fs} n_e k T_e v_e \tag{3.9}$$

where f_e^{fs} is the flux limiter [79]. When calculating the thermal conduction h2d will apply the smaller of the two heat fluxes calculated from the Spitzer or the flux-limited model.

In this work the maximum electron temperature is around 60 eV, and it drops to about 30 eV in a distance of ~50 μm, so L = 50 μm. The electron mean free path in such

a plasma is around 0.3 μm assuming that $n_e = 1x10^{19}$ cm^{-3}. From this it is clear that the classical description in Equation (2.1) is sufficient to calculate the thermal conductivity.

It should be noted, however, that all h2d simulations in this work used the default flux limiter of 0.4. Test cases were performed where the flux limiter was varied over a range from 1 to 0.04 to verify that the classical heat flux was in fact the dominant means of thermal transport, and no differences were found amongst the cases. There is a plethora of publications on the use of a flux-limited heat flux when the laser intensity is above 10^{14} W/cm^2, but nothing exists for the intensity ranges implemented in this work [80-83].

3.1.6. Modeling deficiencies

The most significant deficiency in h2d for modeling mid to high-Z materials is the ionization and radiation transport packages. As mentioned in the previous sections the ionization model is based on an LTE assumption, which in the coronal region of the plasma may not be true. When the plasma density is sufficiently low radiative processes can begin to dominate collisional processes to a point that the radiation temperature and the particle temperature no longer agree. In turn this can cause the populations to deviate from a Boltzmann distribution, which the model assumes. Obviously this can lead to significant errors in the radiation and ionization calculations.

Additionally the lack of bound-bound transitions in the code can introduce significant errors in the radiation field. The multi-group radiation transport in h2d only accounts for free-free and some free-bound transitions. In this work, bound-bound transitions make up a significant portion of the radiated energy, yet in h2d are completely

unaccounted for. Not only does this prevent the use of a single code to model the experiments, since the sought after radiative processes are missing, it also changes the energy balance within the plasma, affecting the hydrodynamic processes.

3.2. Cretin

Cretin provides multi-dimensional non-local thermodynamic equilibrium (NLTE) radiation transfer and atomic kinetic simulations for laboratory plasmas [84]. The time evolution of the atomic populations and photon distributions are followed in a self-consistent method. Each plasma element is modeled according to the distribution of the electrons among the numerous atomic levels. Level populations depend on interaction rates between electrons, ions, and photons. Cretin contains no atomic data. Instead the level structure and transition processes are specified in an external data file provided by the user. The core of Cretin is atomic kinetics and radiation transfer. However, opacities, emissivities, heating rates, heat capacities, conduction coefficients, and other physical quantities can be calculated based on the atomic kinetics.

It should be noted that nonlocal-thermodynamic-equilibrium (NLTE) codes such as Cretin are still under development, and that the results from each code can be very different. In fact, since 1996 there have been regular NLTE code comparison workshops so that the authors of these codes can compare results from identical simulations, and discuss the appropriate treatment of the relevant physics. In Figure 3.1 we can see that the average charge state of Sn ions calculated with various NLTE codes can differ by 2 to 3 levels in the temperature range of interest. This must be kept in mind when using these types of codes.

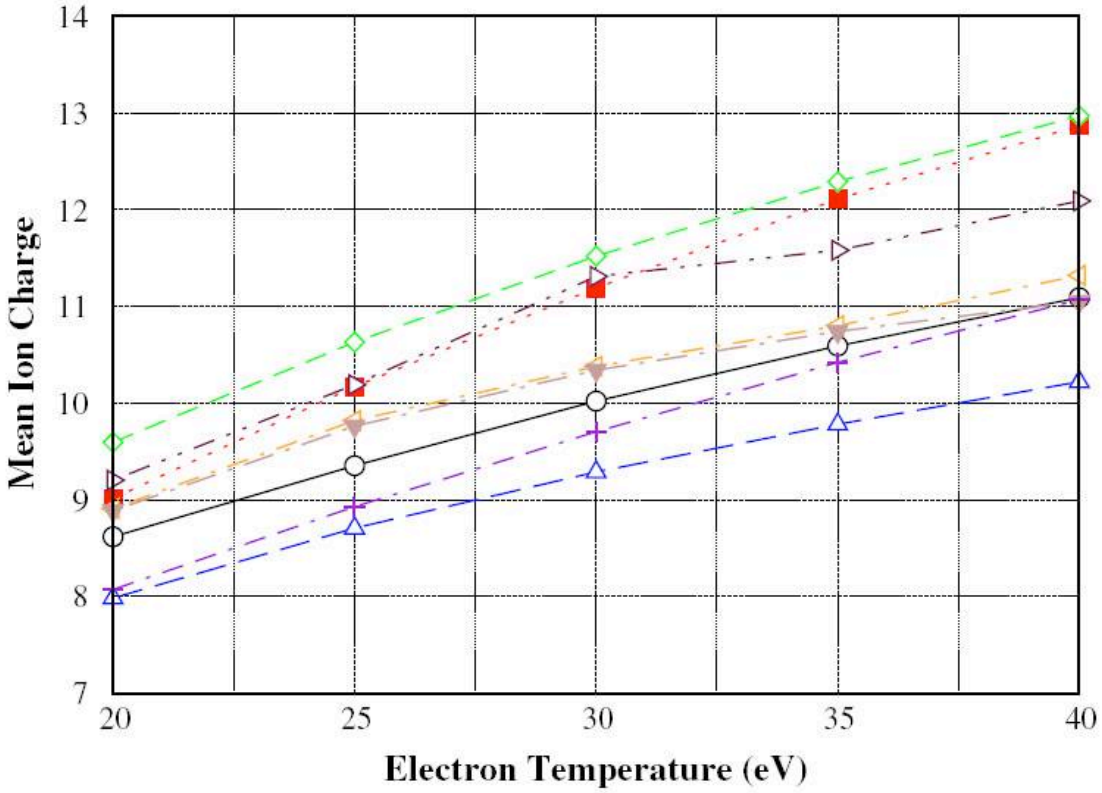

Figure 3.1: Mean ion charge calculated by various NLTE codes for Sn with $n_e = 10^{18}$ cm-3. Cretin results are indicated by red squares. Adapted from [85].

3.2.1. Atomic kinetics

The atomic kinetics in Cretin starts with the calculation of the various rates involved. The details of these rates and how they are calculated can be found in Mihalas [86]. The forward rates, i.e. excitation and ionization, are calculated based on the atomic model provided by the user, and the inverse rates are determined by the principle of detailed balance. Electron collisional excitation and ionization rates, and those of ions when necessary, are based on fits to Maxwellian-averaged collision strengths. Photoionization rates are integrated over the photon spectrum with energy dependent cross-sections derived from the atomic data file.

Because many finite-density effects are absent when using the isolated atom atomic models, Cretin implements a low-density plasma model. Electron degeneracy and polarization are approximately accounted for by continuum lowering. Here the ionization potential is lowered by the Stewart-Pyatt formula [87]. Once the rates are calculated, the atomic populations can be obtained in a time dependent or steady-state mode, where the electron or ion density is assumed to be fixed.

3.2.2. Radiation transfer

Cretin implements a three phase radiation transport routine. Continuum radiation is treated separately from line radiation, and both are coupled to the atomic kinetics and other relevant physics packages. Spectral calculations are the third phase, and provide a means of diagnosing the plasma via detailed spectral emissions. The spectral calculations are not coupled to any physics packages inside of Cretin.

Continuum radiation is composed of a broad, coarse frequency structure used to calculate photoionization integrals. Line transfer is handled by implementing a narrow, highly resolved frequency structure over the range of the line shape. Each line is treated individually and has its own structure. However, overlapping lines can be treated simultaneously when needed. Typically, Voigt functions are used to calculate the line absorption profiles, as the profile is both naturally broadened from the kinetics and Stark-broadened.

When full line transfer is not needed, escape factors can be used. Escape factors provide a convenient approximation for handling radiation transfer problems in hot, optically thick plasmas. The method was first described by Holstein [88], and was applied to Lorentzian and Gaussian line profiles. Escape factors provide reasonably accurate results for radiation transfer of strong line radiation in a much simpler and manageable form.

3.3. Cretin using h2d input

The problems of interest in this work are inherently two-dimensional. The geometry is cylindrical, with the axis of symmetry being along the laser beam. Cretin's hydrodynamic package is only capable of one-dimensional calculations, which limit it's usefulness for this application. Cretin can, however, use any 2-D geometry defined in the problem initialization and perform 3-D radiation transport calculations. Therefore it is possible to use a series of outputs from h2d to define the plasma for Cretin.

There are several ways to define the plasma in Cretin. First the temperature must be defined. Here there is a choice to define the electron, ion, and/or the radiation

temperature. For this work the electron temperature was defined and Cretin calculated the other temperatures based on the atomic model. The second plasma parameter that must be defined, for Cretin to perform the sought after calculations, has to do with the distribution of material. This parameter also has several options. The user can input the average charge state, ion density, electron density, and/or mass density. Here we chose to only input the electron density. This allows Cretin to calculate the plasma properties more accurately based on the atomic model provided in the input file.

The h2d simulations provide the electron temperature and density at equally spaced intervals, typically every half ns. These plasma property dumps are then post processed one by one into text files that contain the coordinates, temperature, and density of each node in the computational mesh. The computational mesh is restructured from the original h2d mesh for use in Cretin. In Figure 3.2 an original h2d T_e profile is compared to the same profile processed for use in Cretin. The zone reduction is necessary because a large number of zones are required to accurately model the laser ablation process in h2d. Reducing the zones did not significantly affect the radiation transport calculations performed by Cretin. Each text file produced from the h2d dumps is for a single moment in time. The files are input into Cretin one at a time, providing snapshots of the emission for each moment during the problem. These snapshots can then be assembled to provide time-integrated information. This method is only valid when the atomic transitions have a lifetime much shorter than the evolutional time scale of the plasma. This is the case here since the average lifetime is around 1 ps for the transitions of interest [89].

The final piece of the computational puzzle is the atomic data used by Cretin. As described in chapter 1, the emission of interest here comes from the $4p^6 4d^N - 4p^5 4d^{N+1} + 4p^6 4d^{N-1} 4f$ ($9 \geq N \geq 1$) transitions, the unresolved transition array (UTA), produced in Sn^{5+} to Sn^{14+} [54]. These transitions can not be properly accounted for using the screened hydrogenic model built into Cretin. Instead a more detailed atomic physics model must be employed that uses quantum mechanical principles to accurately calculate the rates and energies of these transitions. The Hebrew University Lawrence Livermore atomic code (HULLAC) is a popular choice for performing such calculations [90]. Tin atomic data were provided from Lawrence Livermore National laboratory containing the relevant transitions from charge state Sn^{6+} to Sn^{14+}. The number of transitions was significantly reduced from hundreds of thousands to thousands to make the problem tractable. The HULLAC data were then post processed to a form that can be read by Cretin. These data were used for the atomic model for all Cretin results presented in this work.

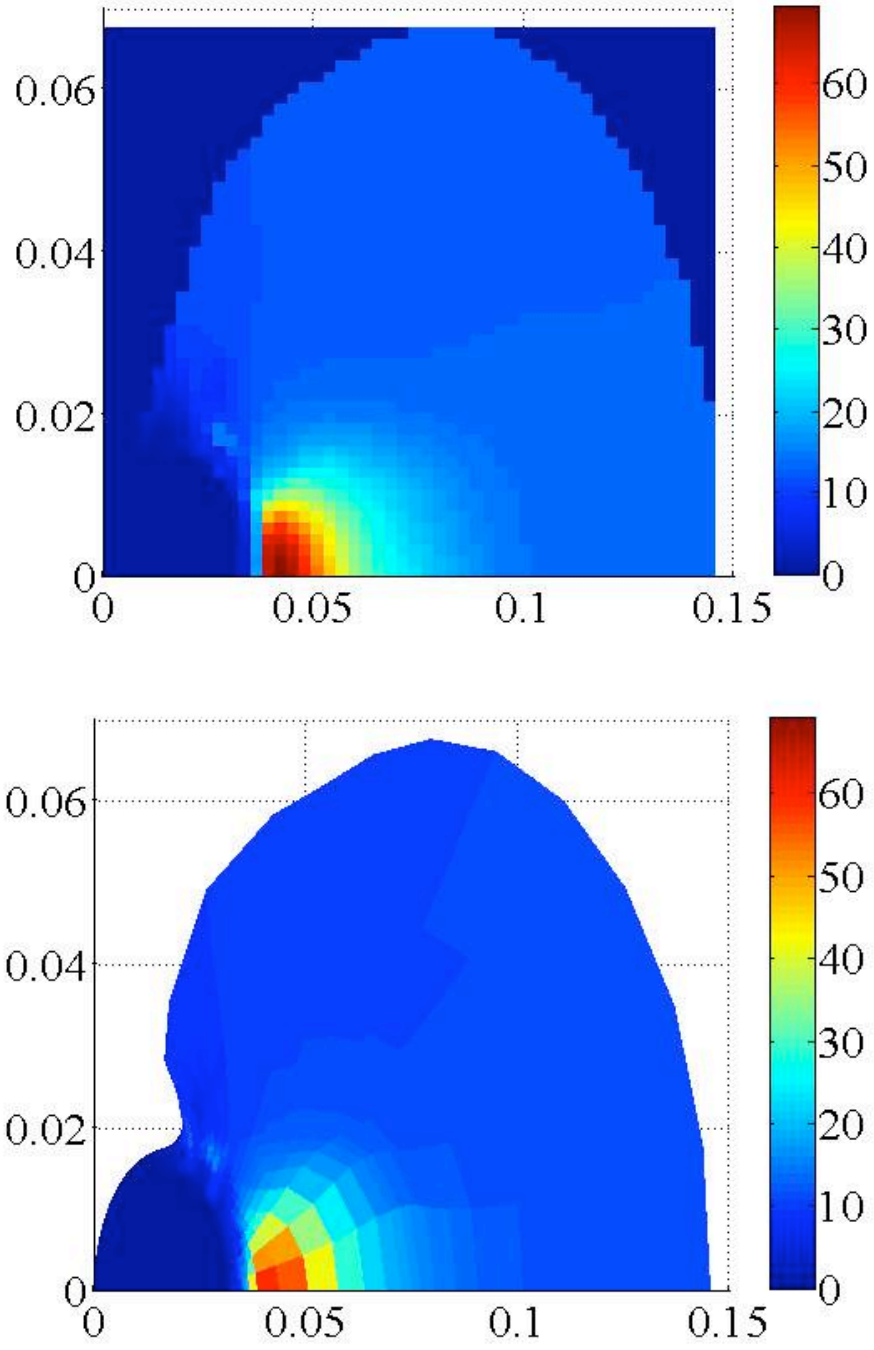

Figure 3.2: Electron temperature profile used for Cretin computations (top) compared to the profiles produced by h2d (bottom). The dimensions are in microns and the color scale is in eV.

4. Experimental results on geometry effects

The need to study the effects of target geometry on the in-band emission arises from the power requirements for HVM. To meet the requirements using reasonable laser energy and minimal target material, a lithography system will need to operate at around 10 kHz, and hence the target delivery system must supply tin targets at 10 kHz. One proposed method utilizes a high repetition rate liquid Sn droplet generator [91], seen in Figure 4.1. Yet many of the studies so far have used planar targets [92-95], or spherical targets [55, 96, 97] without any direct comparison between the two target geometries. In this chapter the effect of the plasma dynamics, caused by the target geometry, on the EUV emission will be explored.

4.1. Planar target

In the following sections, the experimental results for planar targets will be presented. The angular dependence of the in-band EUV as well as the EUV spectral shape will be covered in sections 4.1.1 and 4.1.2 respectively. It is important to note that the E-Mon and TGS are both at 45° with respect to the axis of symmetry, but on opposite sides of the plasma. Because the symmetry of the plasma is not perfect, the two diagnostics do not see identical plasma conditions. Additionally the plasma density evolution is characterized at various stages during the laser pulse. Finally, the in-band EUV emission is characterized spatially by time-integrated imaging and temporally with a fast photo diode.

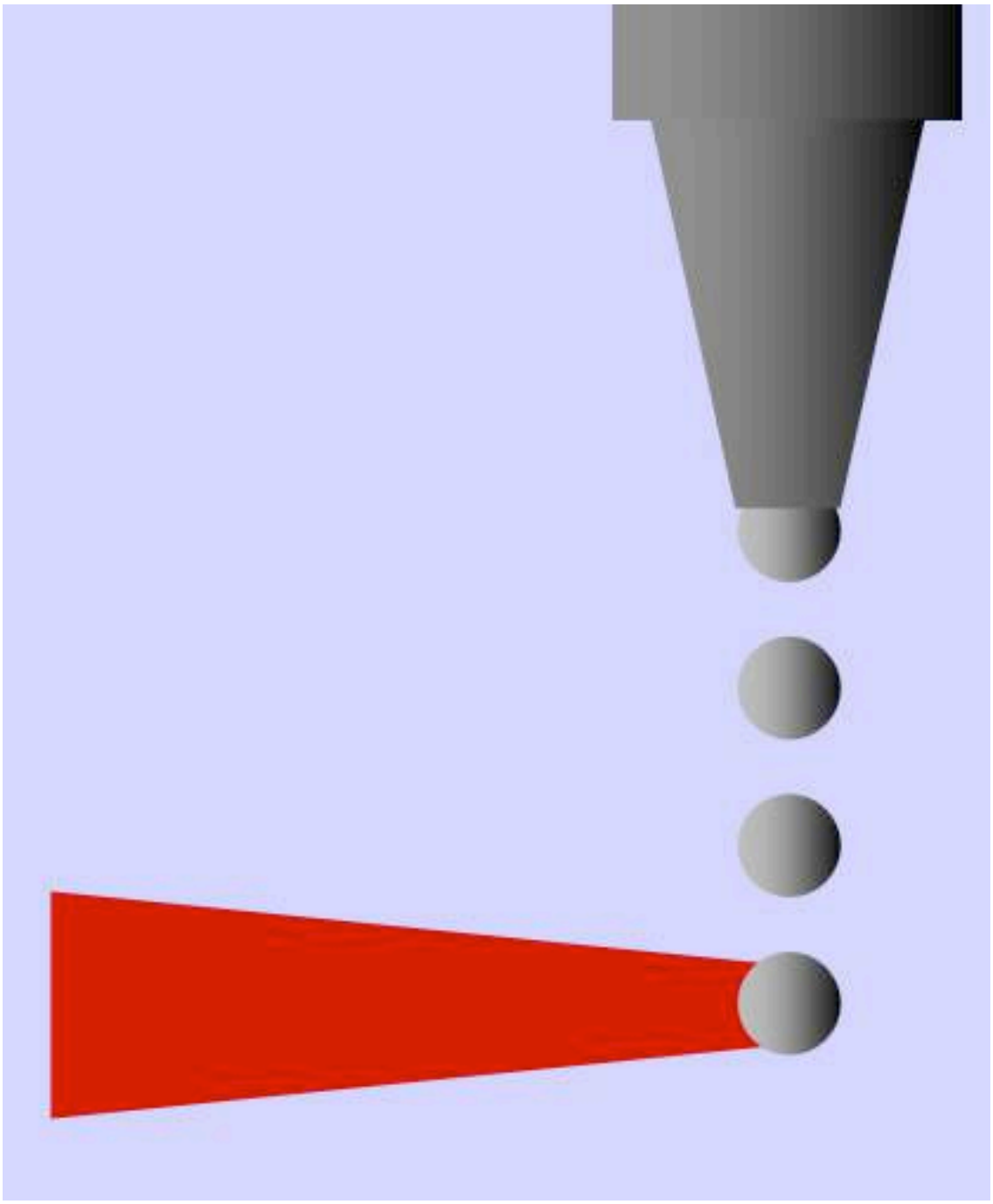

Figure 4.1: High repetition rate liquid Sn droplet generator and laser engagement (not to scale)

4.1.1. Angular distribution of in-band EUV for planar targets

Angular distribution measurements of the in-band EUV emissions were obtained by rotating the target and laser beam together so that the laser incidence is always normal to the target surface as shown in Figure 4.2. This was achieved by mounting the slab target on one of three aluminum wedges, and then mounting the wedge on the three-axis stage. The wedge angles are 15°, 30° , and 45°. With these three wedges measurements from 0° – 90° every 15° can be made. The laser is kept normal to the target surface by using a pair of broadband mirrors to steer the beam inside the chamber. However, for 0° and 90° measurements the laser cannot be at normal incidence less the mirror block the diagnostics, so the laser is at 10° incidence for the extreme angles. The total distance from the focusing lens to the target surface is fixed at 317 mm, so that the $1/e^2$ spot size is 150 μm. The laser energy is 250 mJ, making the laser intensity around $2x10^{11}$ W/cm^2.

Figure 1.1 shows the angular distribution of the in-band EUV for the conditions described above. Both the E-Mon measurements and data collected with the TGS are presented here. The major source of error for these measurements is in the alignment.

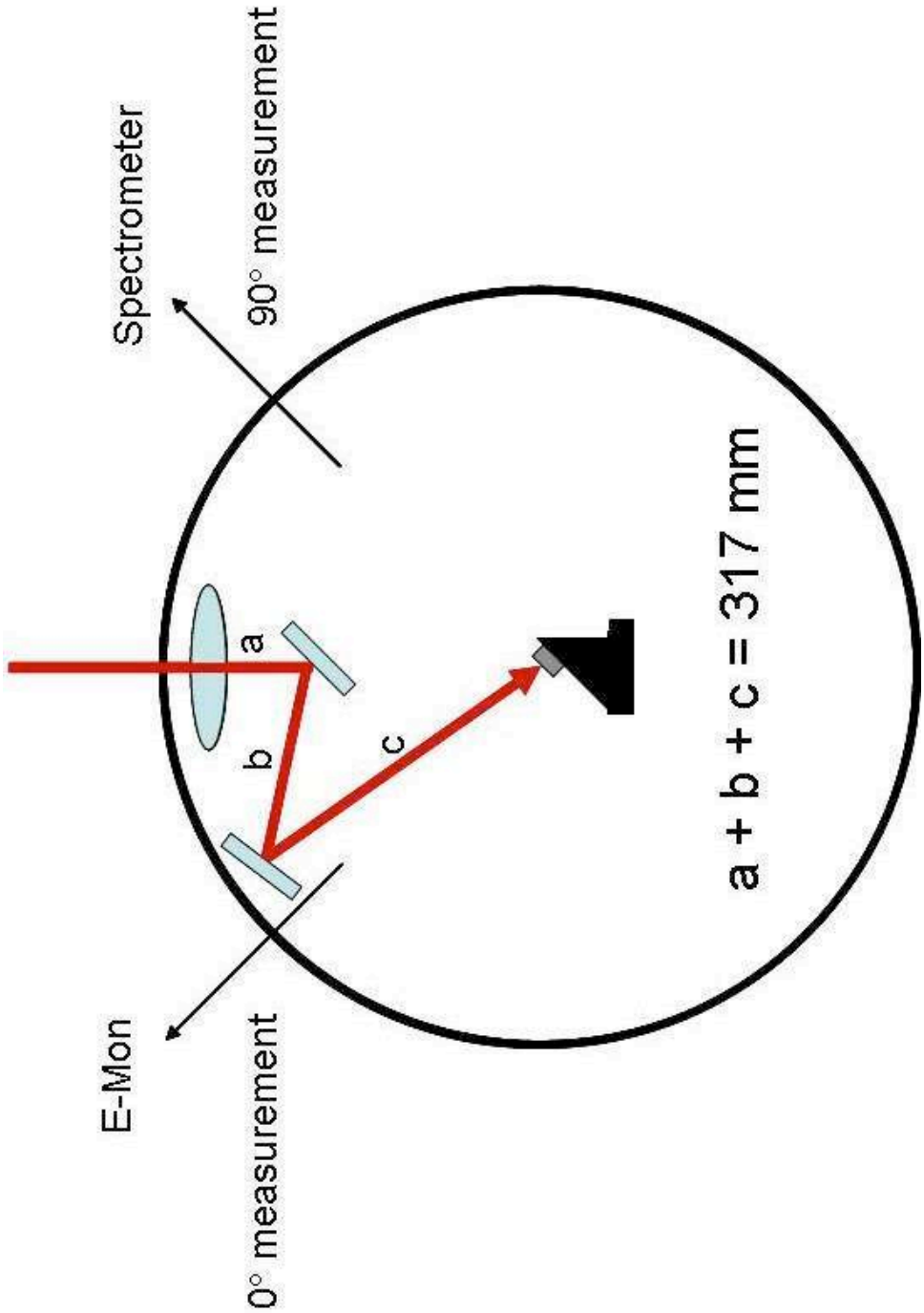

Figure 4.2: Schematic of laser path for angular distribution measurements.

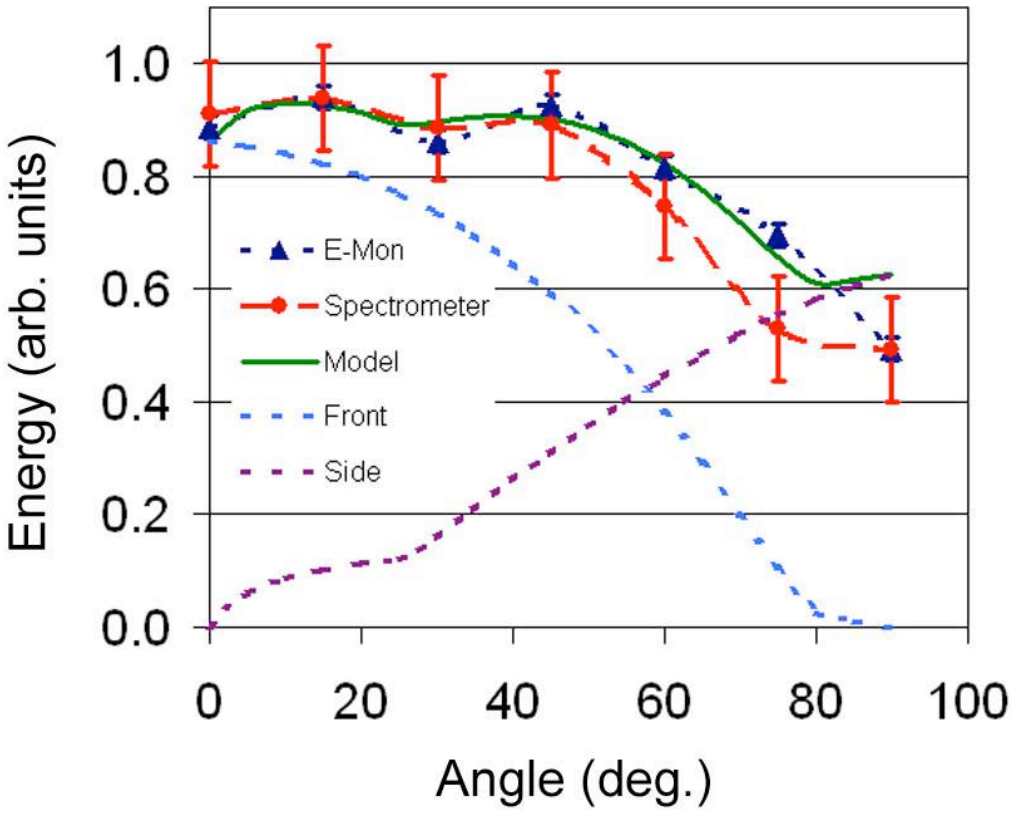

Figure 4.3: Angular distribution if in-band EUV emission measured by E-Mon (blue) and TGS (red), along with calculated values from a simple model (green). The front and side components of the model are shown in light blue and purple respectively. 0° is along the laser axis.

Therefore the measurements were conducted on three separate occasions where the beam path was reconstructed and aligned each time. Data labeled E-Mon are scaled values directly from the E-Mon readings. Whereas data labeled spectrometer, are scaled values calculated from the spectra taken with the TGS. The spectra were integrated over the range 13.23 – 13.77 nm providing an in-band energy measurement.

The TGS data have larger error because, having a much smaller aperture, it is much more sensitive to alignment than the E-Mon. Additionally at large angles the E-Mon and TGS measurements do not agree as well as they do at smaller angles. At small angles both instruments are directed toward essentially the same region of the plasma, but at large angles, the two diagnostics see opposite sides of the plasma. If the plasma were perfectly symmetrical the E-Mon and TGS measurements would be identical. The fact that they are not indicates that there is an asymmetry to the plasma about the laser axis. The asymmetry arises from the less than perfectly Gaussian laser spatial profile.

The data in Figure 1.1 show a double peak structure in the angular distribution. Previous studies [49, 51, 94, 98, 99] found that the EUV monotonically decreases as the angle increases from 0° to 90° according to,

$$E_{EUV}(\theta) = \alpha + \beta \cos^{\gamma} \theta , \tag{4.1}$$

where θ is the angle between the surface normal and the detector. In these earlier studies the laser spot size was large compared to the plasma scale length, making the expansion dynamics one dimensional. A typical laser spot size for references [49, 51, 94, 98, 99] is around 500 μm. In this work the spot size is around 150 μm making the expansion more

two dimensional, and it is this effect that causes the double peak structure of the angular distribution.

A simple model was developed to validate that such a distribution arises when the plasma is two dimensional. The model assumes that the plasma consists of a hot emitting core region surrounded by a cool, low density absorbing region. A diagram of the plasma model can be seen in Figure 4.4. The emitting region is considered optically thick. However, the inner region is not so optically thick that photons emitted just under the surface of the region can not escape. This effect is taken into account by γ in Equation (4.1), which is determined empirically, and is 0.5 for a 1.064 μm laser [99]. Only emissions from the front and one side surface contribute to the total detected EUV emission. The surrounding plasma absorbs the EUV emission according to,

$$E_{out} = E_{EUV}(\theta) \cdot \exp\left(\frac{-\mu}{l}\right), \tag{4.2}$$

$$l = \min\left[\frac{t}{\cos(\theta)}, \frac{d}{\sin(\theta)}\right], \tag{4.3}$$

where μ is the absorption coefficient, t is the thickness of the absorbing layer and d is the distance from a rays origin to the side edge of the absorption region. The model utilizes three regions within the absorbing layer; a front and side region corresponding to the two emitting surfaces, and a corner region where the two meet. The corner region is outside of the laser beam and is far from the hot plasma center leading to a lower temperature and therefore higher opacity.

A Matlab code was written to find the dimensions and μ of each region. The code varies the lengths of the front and side emitting surfaces, the thickness of the front and

side absorbing layers, and μ in each of the three absorbing regions. The emissions from the front and the side surface are calculated using Equation (4.2). Note the angle is between the emitting surface and the laser so that as θ increases from 0° to 90° for the front surface it decreases from 90° to 0° for the side surface. Rays that exit the sides of the absorption regions don't travel the full distance t/cos(θ). Instead the ray travels a distance d/sin(θ) through the region. The code scans through a reasonable range for each parameter, lengths, thicknesses, and absorption coefficients, and calculates the total detected emission. The calculated emission is compared to the experimental measurement by a least squares method to determine the optimum set of parameters to reproduce the measured distribution. The calculated angular distribution with the best fit can be seen in Figure 1.1 as the green line. The contributions from the front and side surfaces can also be seen as the blue and purple dashed lines respectively. It can be seen that the simple model is able to reproduce the angular distribution of the in-band EUV emission. This indicates that the two-dimensional plasma expansion has a significant effect on the total in-band emission. The dimensions and absorption coefficients resulting from the simple model can be seen in Figure 4.4. In later sections we will see how well the model was able to predict the dimensions of the emission and absorption regions.

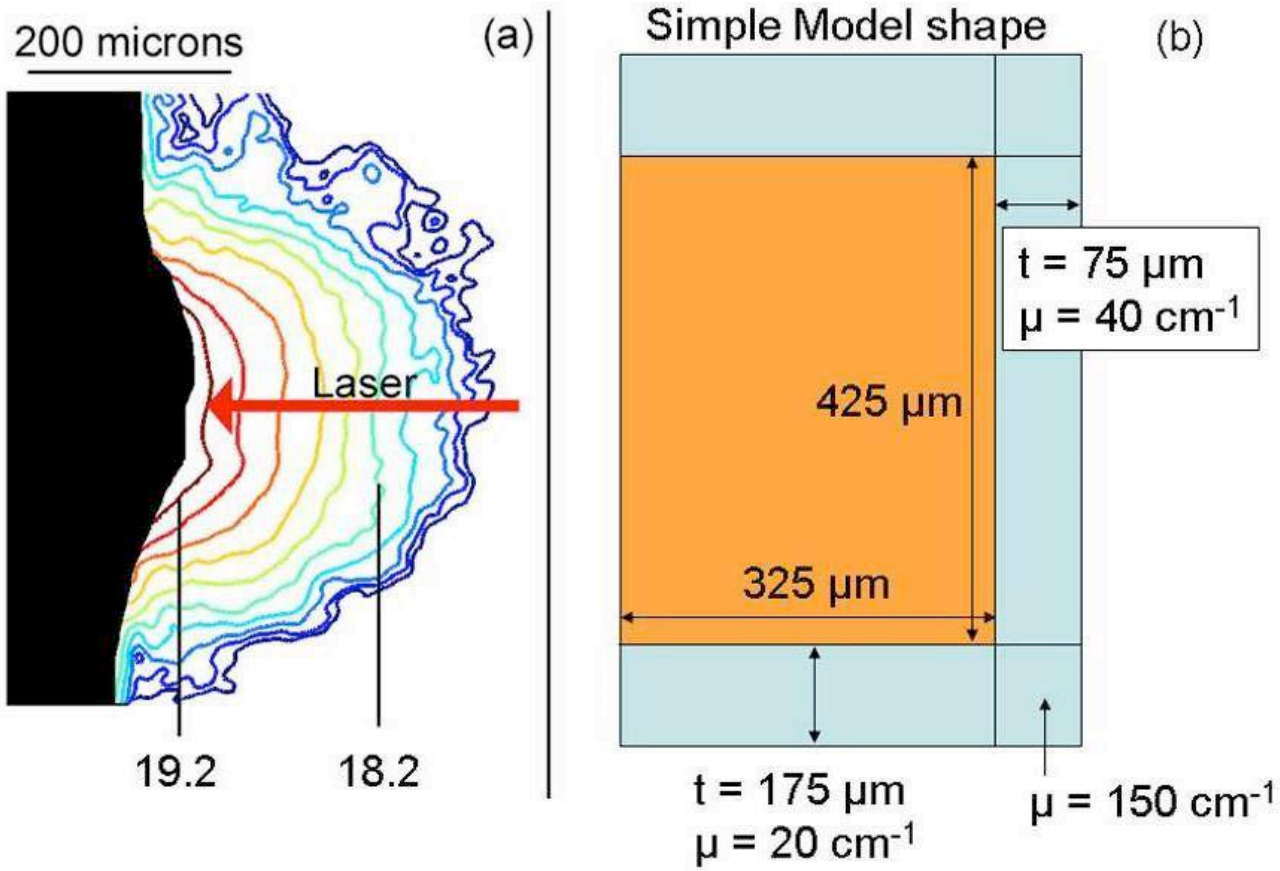

Figure 4.4: Comparison of electron density (a) and simple model geometry (b).

4.1.2. Angular dependence of EUV spectrum for planar targets

The EUV spectrum was measured simultaneously along with the in-band energy, so that a 0° measurement with the E-Mon corresponds to a 90° measurement with the TGS, see Figure 4.2. The data from the TGS shown in Figure 1.1 is consistent with the E-Mon measurements as discussed in the previous section.

The angular dependence of the EUV spectrum is shown in Figure 4.5. Here it can be seen that the peak is centered at 13.5 nm at 90°, and shifts to shorter wavelength as the angle decreases. The 13.5 nm peak is produced when the charge state is around 10. The shift to shorter wavelengths indicates the average charge state is above 10, and that the plasma is hotter than the optimum temperature for in-band production. However, in-band EUV production is not the only factor that determines the CE. The surrounding plasma readily absorbs the in-band emissions, making it necessary to overheat the plasma core in order to reach the optimum balance of emission and absorption. Overheating the core of the plasma allows the location of the optimum temperature to coincide with the location of the optimum density.

It is also evident that the long wavelength, out-of-band emissions increase as the angle decreases. This is a result of the plasma heating along the laser axis. It is shown in Equation (1.3) that the laser absorption depends on n_e^2. Thus most of the laser is absorbed near the critical surface. However, a portion of the beam is absorbed by the low density plasma away from the target surface along the laser axis. Additionally, the plasma expands nearly normal to the target surface when near the laser axis, allowing the heated ions to remain inside the laser beam, close to the axis. This produces a wide range

of charge states that in turn produce a wide spectrum. From the spectra it is evident that the plasma along the laser axis contains Sn^{7+} to Sn^{14+}. The main mechanism of heating for the sides of the plasma is radiation transport and conduction from the center. This leads to cold dense plasma developing along the side of the plume, which absorbs the emission from the plasma core in a spectrally uniform manner. The sharp drop in temperature and density laterally, near the edge of the laser beam, produces a uniform charge state and a narrow spectrum in the lateral regions outside of the laser beam.

Another notable feature of the spectra is the dip in the in-band portion that first appears at 45°, is most prominent near 15°, and nearly disappears by 0°. The dip corresponds to resonant lines from Sn^{9+} to Sn^{11+} [65]. The dip indicates that the emitted in-band light travels through more plasma in the temperature range of 20 to 30 eV when the viewing angle is around 30°. The reduction in the dip at 0° is likely due to a reduction in the electron density along the laser axis. This will be discussed later in section 4.1.3.

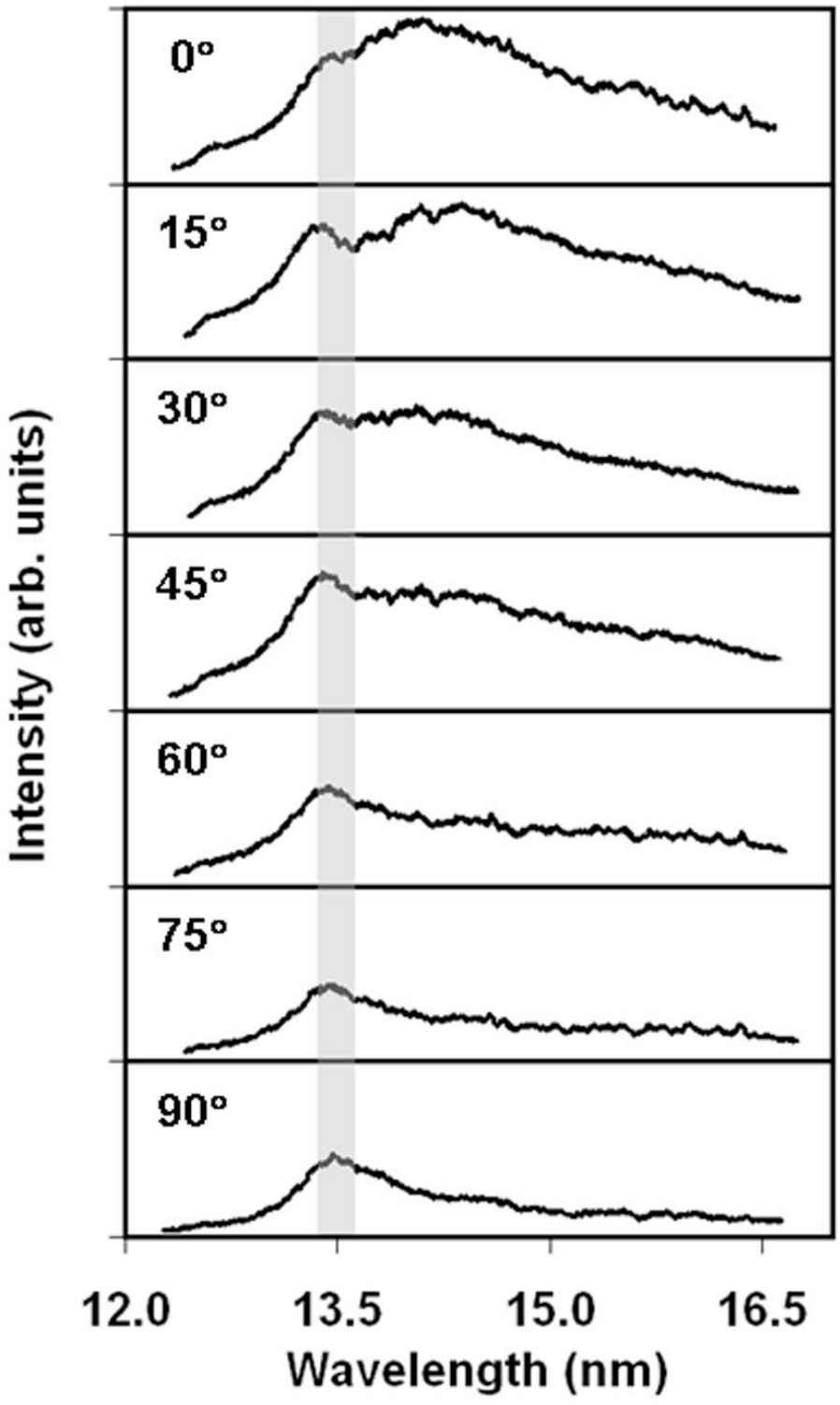

Figure 4.5: Angular dependence of EUV spectra for planar targets

4.1.3. Plasma density measurements for planar targets

In the experiments conducted in this work, the only fundamental plasma parameter that can be measured directly is the electron density. The electron density influences the EUV emission directly due to the fact that collisional de-excitation is responsible for a majority of the in-band light being generated. The electron density also provides insight into the temperature, charge state and opacity. From Equations (1.6) and (1.7) the plasma scale length is proportional to square root of the electron temperature and the average charge state. This can be helpful to determine if the plasma is at optimal conditions for 13.5 nm light production, thought to be where $\overline{Z}$ is around 11 and T_e is around 30 eV [49, 65, 95].

The 2-D plasma density evolution is shown in Figure 4.6, and

contains line profiles along the laser axis of each image in Figure 4.6. It can be seen that the plasma is already well developed by 3 ns before the laser peak.

It is well known that the coronal plasma density along the laser axis is given by,

$$n_e(z) = n_0 \exp\left(\frac{-z}{l_s}\right), \tag{4.4}$$

The natural log of the electron density profile along the laser axis, Figure 4.8, is fit with a linear function. The slope of the linear fit is the inverse of the scale length, l_s. The plasma scale length obtained from Figure 4.8 is 69 and 161 microns for the early and late times respectively. The plasma scale length is related to the plasma temperature and the average charge state by,

$$l_s = \left(\bar{Z}T_e / M_i\right)^{1/2} \tau_{laser}, \tag{4.5}$$

Since we only know the product of $\bar{Z}$ and T_e from the scale length, it is necessary to calculate the proper dependence of $\bar{Z}$ on the temperature. From Figure 4.9, $\bar{Z}$ can be determined for any given temperature at an electron density of $1x10^{19}$ cm^{-3}. It can also be seen in Figure 4.9 that $\bar{Z}$ has a weak dependence on the electron density in the range from below 10^{18} to 10^{20} cm^{-3}, only changing by about 1 over these densities. Therefore the calculated values of $\bar{Z}$ can be applied to a large portion of the coronal plasma without much error. Using Equation (4.5) with the scale lengths above the plasma temperature and charge states are calculated to be 32 eV with $\bar{Z}$ of 12 for 3 ns before the laser peak, and 25 eV with $\bar{Z}$ of 10.5 at 4 ns after the peak. It should be noted here, as discussed in chapter 3, that there is a significant discrepancy between the various models used to predict $\bar{Z}$ in such a plasma.

It is clear from the plasma scale length measurements that the plasma reaches the optimum conditions for in-band EUV emission where $T_e \sim 30$ eV and $\bar{Z}$ is around 11. However, as discussed earlier the generation of in-band emission is only part of the problem, the surrounding plasma acts to absorb the EUV light reducing the net production. It can be seen in Figure 4.6 that the lateral dimension of the plasma extends over 700 μm across despite the fact that the laser spot size is only 150 μm. As a result, dense plasma surrounds the emitting region as described in Figure 4.4. It is evident from the spectra shown in Figure 4.5 that the surrounding plasma is too cold for efficient EUV production, as expected, since the plasma is outside of the laser path.

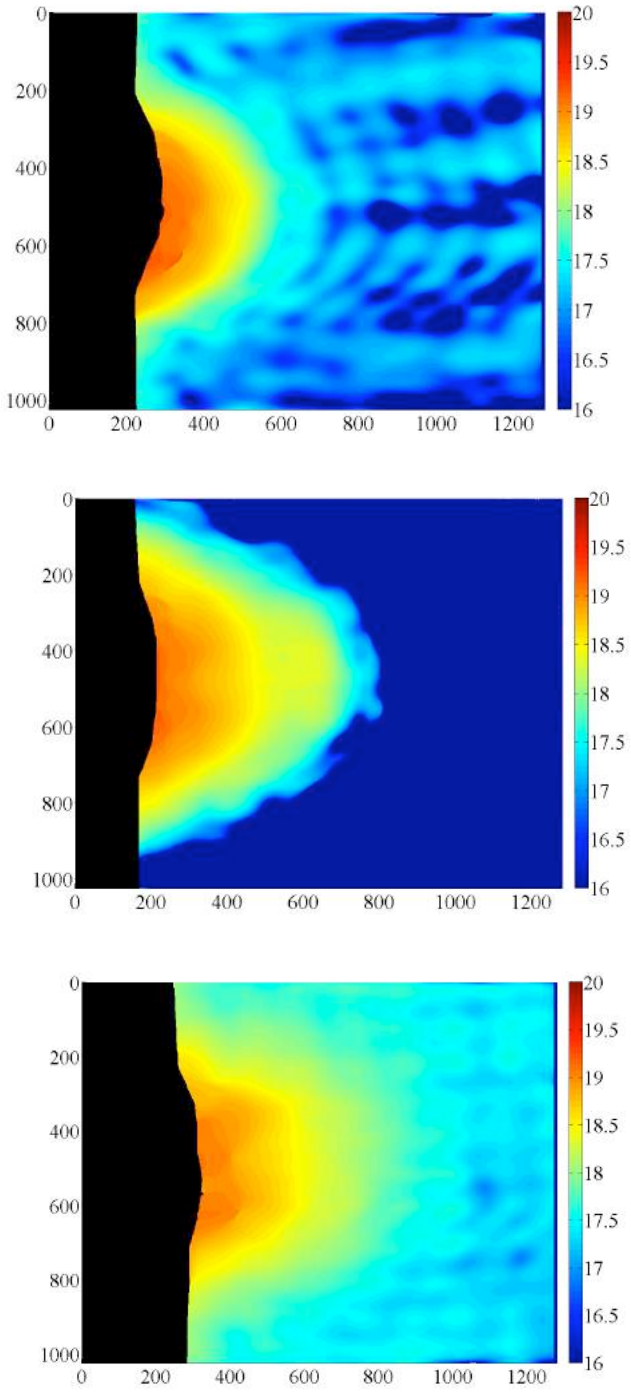

Figure 4.6: Plasma density profile at -3 ns (top), 0 ns (middle), and +4 ns (bottom) with respect to the laser peak. The spatial scale is microns and the color scale is the $\log_{10}$ of ne in cm^{-3}.

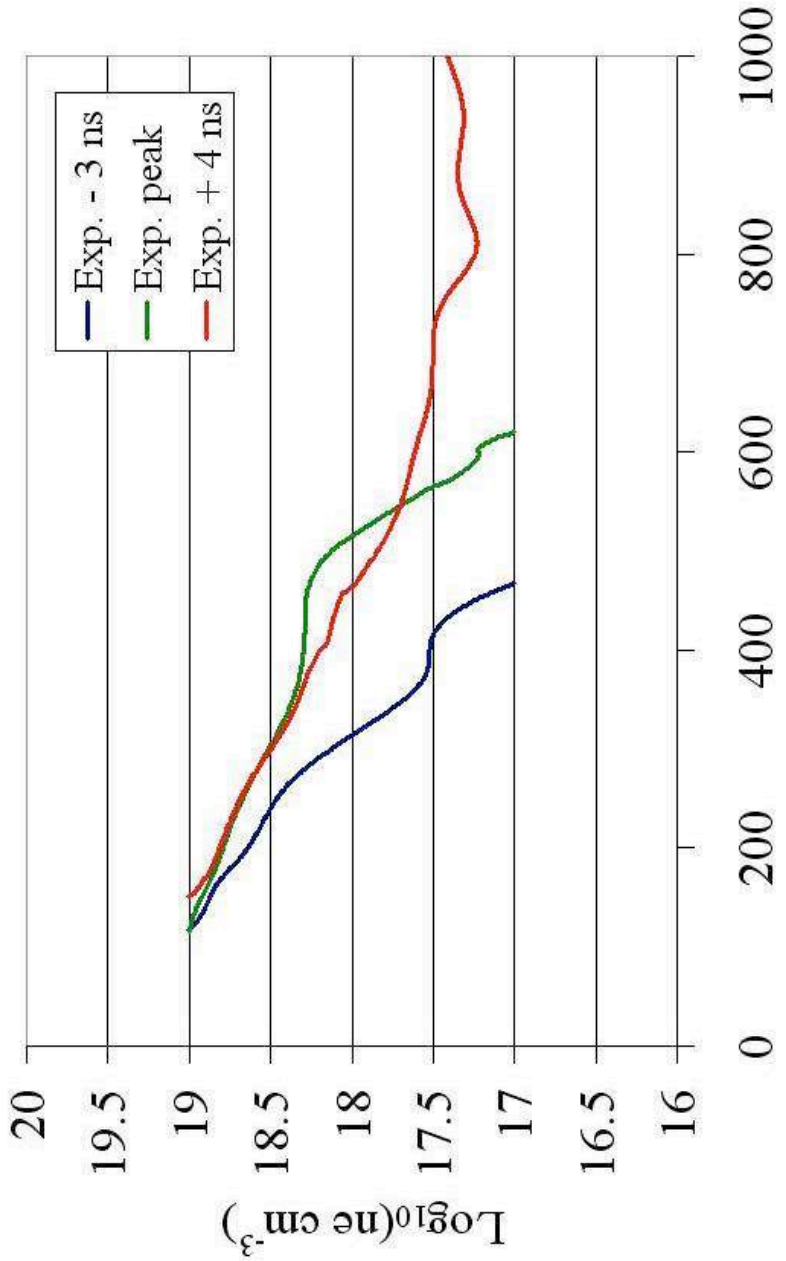

Figure 4.7: Plasma electron density along the laser axis at 3 ns before (blue), during (green), and 4 ns after (red) the peak laser intensity.

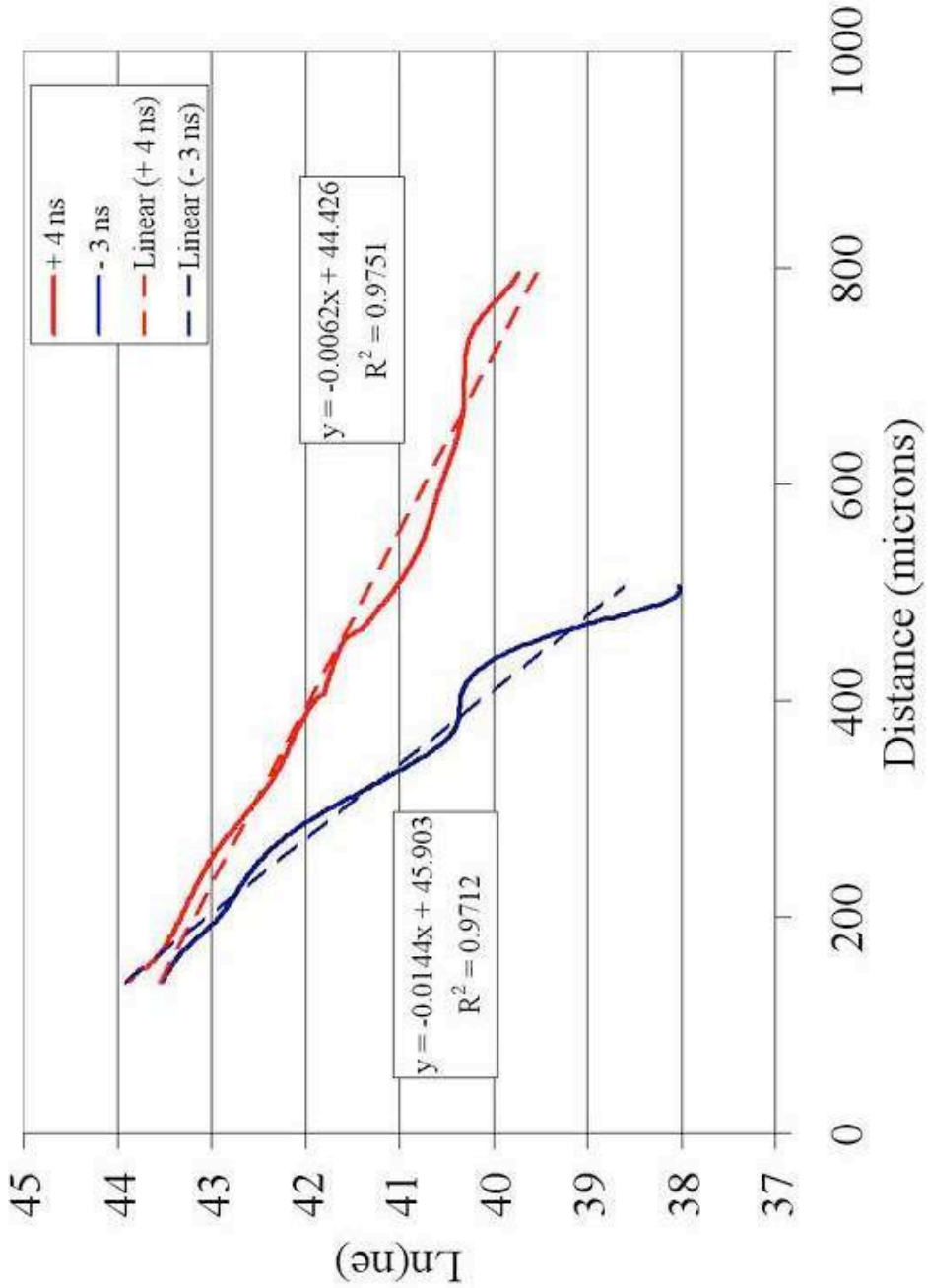

Figure 4.8: Natural log of the electron density 3 ns before (blue) and 4 ns after (red) the laser peak.

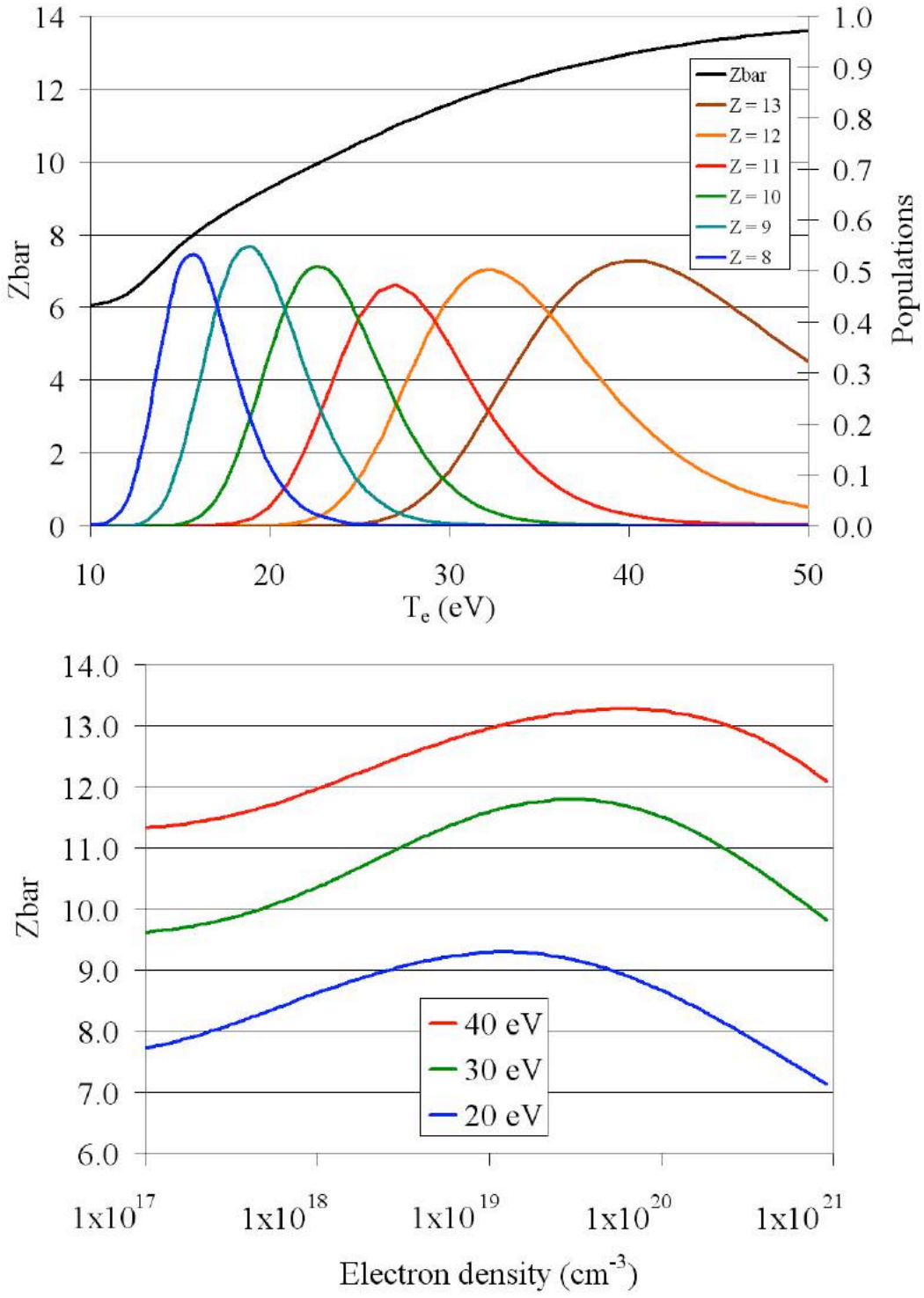

Figure 4.9: Charge populations and $\overline{Z}$, vs. T_e with $n_e = 1x10^{19}$ cm^{-3} (top) and vs. n_e at 20, 30, and 40 eV (bottom).

4.1.4. EUV imaging for planar targets

Time integrated in-band EUV images were acquired under the exact conditions as described in the preceding sections. The details of the experimental arrangements can be found in chapter 2. The images provide information on cross sectional profile of the emission region. This information is utilized to understand the plasma conditions where the EUV is generated, gain a better understanding of the radiation transport, and reveal the location in the plasma where the laser absorption is strongest.

Figure 4.10 is a typical image of the in-band EUV produced with planar targets. The low level light seen throughout the image is scattered visible light detected by the camera and has a typical intensity of between 1400 and 5000 counts. The background light is still present and has the same distribution when the camera is blocked with a piece of glass so that no EUV light is detected. Unfortunately the shot to shot intensity of the background varies too much for a reliable background subtraction to be performed. The figure also includes approximate contours at 20% and 70% of the peak intensity. These contours will be used in later figures to indicate where the emission occurs within the plasma.

Figure 4.10 can be used to compare the dimensions of the emitting region of the actual plasma with those calculated in the simple model presented in section 4.1.1. A box is drawn around the emission region in the EUV image which corresponds to the size and shape of the emission region calculated via the simple model. There are also two red lines which indicate the lengths for the absorption region in the lateral and longitudinal directions. The majority, measuring to 20% of the peak value, of the measured EUV emission is produced in a region that is approximately 300 by 330 μm, and the model

predicted an emission region with the dimensions of 325 by 425 μm. The agreement is within 10% in the longitudinal direction; however the lateral dimension differs significantly. The explanation for this will be explored in chapter 5, when two-dimensional radiation hydrodynamic simulation results are presented.

The peak intensity of the EUV image is located between 180 μm and 240 μm from the target surface, as can be seen in Figure 4.11. In this figure a line profile along the laser axis is extracted from the 2-D image. The peak location agrees with that found by Tao et al. [48] where a 10 ns, 1.064 μm laser pulse was utilized. One point worth noting is that the emission profile extends behind the target surface. Since it is impossible for the emission to come from within the bulk material, an explanation is necessary. There are two possible explanations. One is that the image is not in proper focus so that the edges of the emission are blurred causing the appearance of emission behind the surface. This is not likely the issue here, since care was taken to ensure that proper focus was achieved. The most likely explanation is that the imaging system was not perfectly aligned to look across the target surface. This is a typical problem in the experiments in this work, and is seen frequently when acquiring interferograms for planar targets. The effect is that the camera observes the plasma from a small angle so that the view of the plasma is clipped by the edge of the target. It is not uncommon to clip 50 to 100 μm of the plasma in an interferogram, so it is not unreasonable that the same could occur here. The difference is that in an interferogram the plasma is back lit, so that the slight angle of the target surface causes a shadow. For the EUV imaging the plasma is the light source so the target acts as a backdrop.

4.1.5. In-band EUV temporal profile measurements

The final measurement to be presented for planar target geometry is the temporal profile of the in-band emission. The EUV emission is determined by the plasma temperature and, to a lesser extent, the plasma density. In turn the plasma temperature is determined by the laser intensity, which has a Gaussian temporal profile and can be seen in Figure 4.13. In this figure the in-band EUV history can be compared to that of the laser intensity. It can be seen that the EUV emission follows the laser intensity on the rising edge of the pulse. After the laser reaches the peak intensity, the EUV begins to decay. Interestingly the EUV emission decay is delayed by approximately 1 ns compared to the laser intensity. This is the first experimental indication presented in this work that suggests the plasma is over heated.

The plasma can not emit in-band radiation if the temperature is too low, so the continued radiation after the laser peak indicates the plasma is remaining above the minimum temperature required for in-band generation. The only external heating source is the laser, and the main mechanism for cooling is radiation. It is also known that the transitions responsible for the EUV emission have lifetimes of around 1 ps, this means that a single ion could excite and de-excite nearly 1000 times in the 1 ns time between the laser and EUV peaks. If the plasma were at just the right temperature the EUV emission would follow the laser profile, because the temperature would rapidly drop due to radiation. However, if the plasma is over heated, then there would be a delay in the decay of the emission associated with the plasma cooling from an over heated state to an optimal state.

In Figure 4.13 it can be seen that the laser pulse is composed of several modes that produce a double peak. These peaks are also present in the EUV emission. The first peak of the laser pulse has a slightly higher intensity than the second, yet in the EUV emission the second peak is higher. This is another indication that the plasma is being overheated. The emission region remains hot due to the overheated plasma at higher densities while the first peak in the laser pulse decays. During this time the plasma conditions in the emission region do not change enough to significantly reduce the in-band emission. The second laser peak provides additional energy to the plasma, which is then converted to in-band emission. The increased in-band emission with lower laser energy may indicate that increased pulse durations and/or laser pulse shaping could be used to increase the CE. More insight into the overheating of the plasma will be gained in chapter 5.

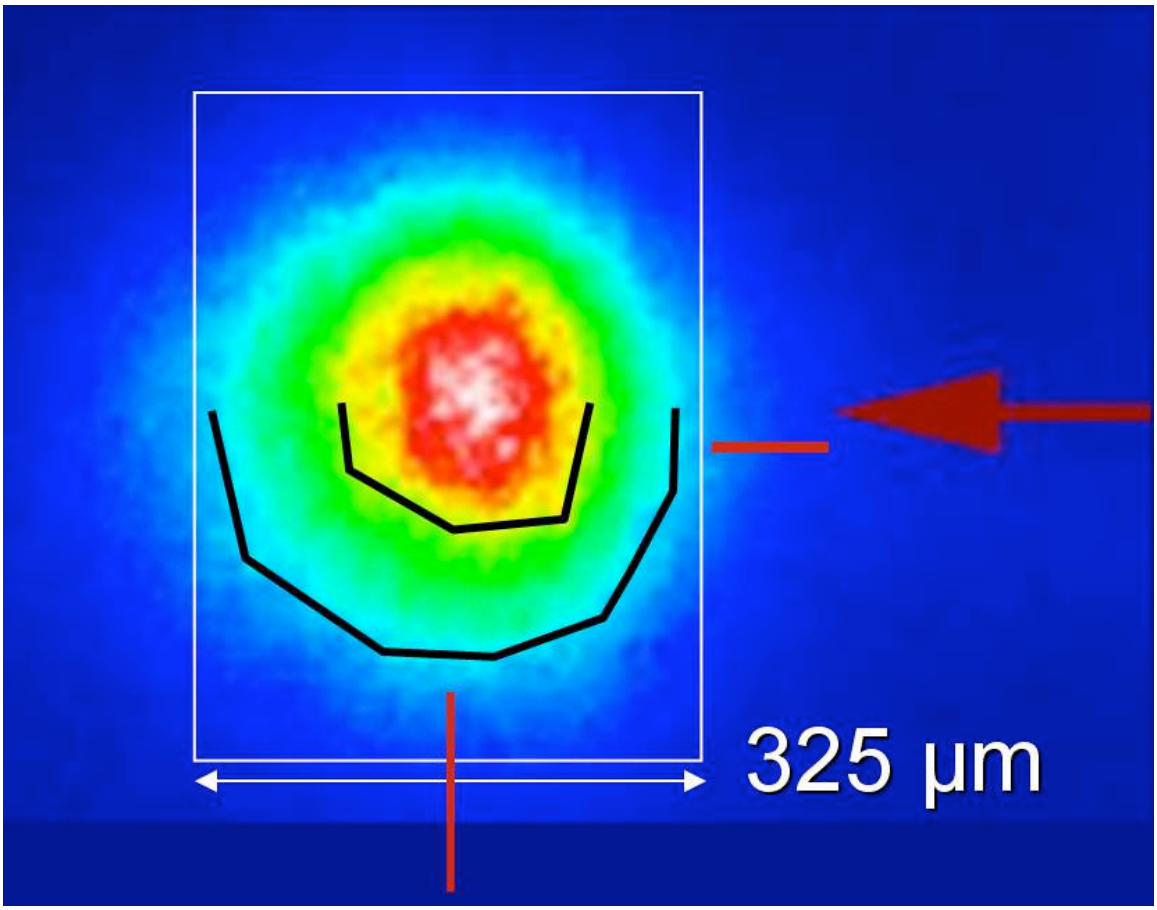

Figure 4.10: Typical time integrated in-band EUV emission from a planar target. The arrow indicates the laser incidence. Approximate contours are drawn at 70% and 20% of the peak intensity. Box outline and red lines indicate scales from simple model.

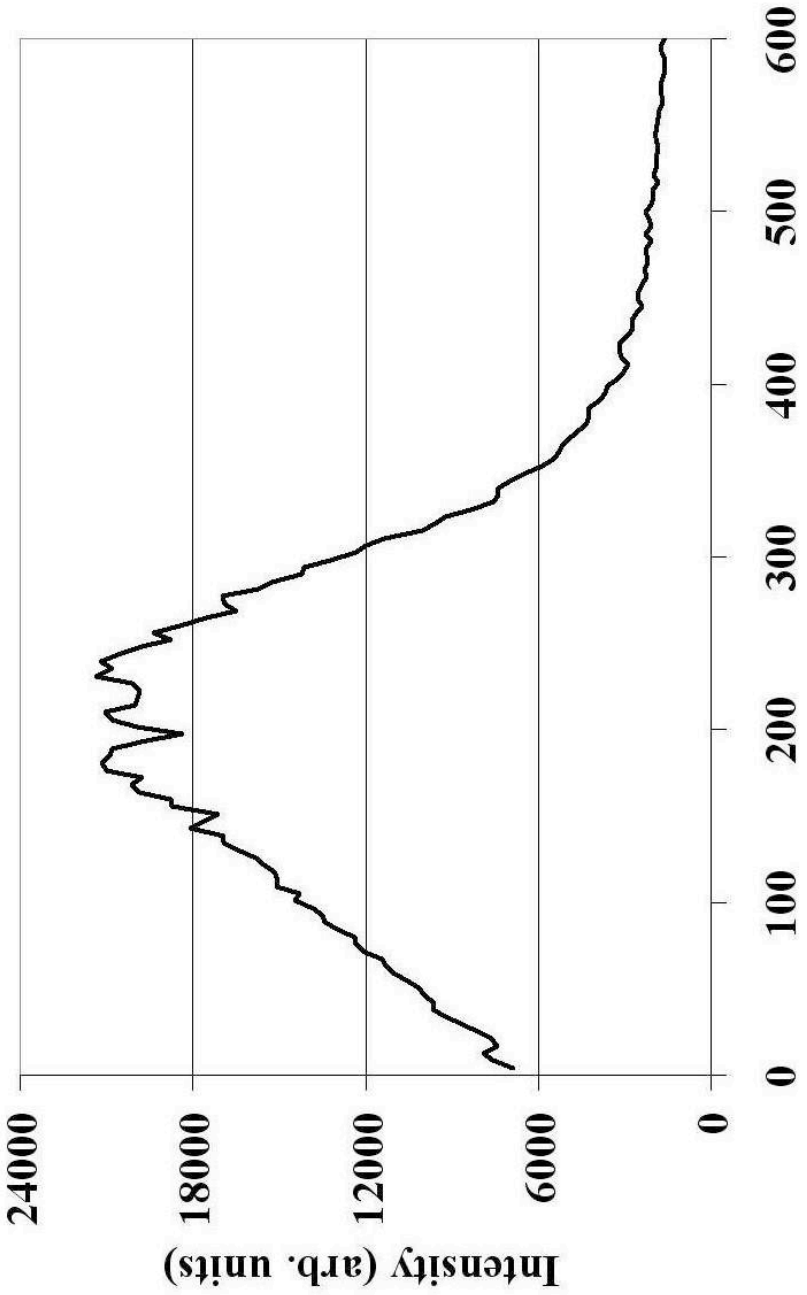

Figure 4.11: Typical line profile of in-band EUV emission along laser axis for a planar target. Zero represents the target surface.

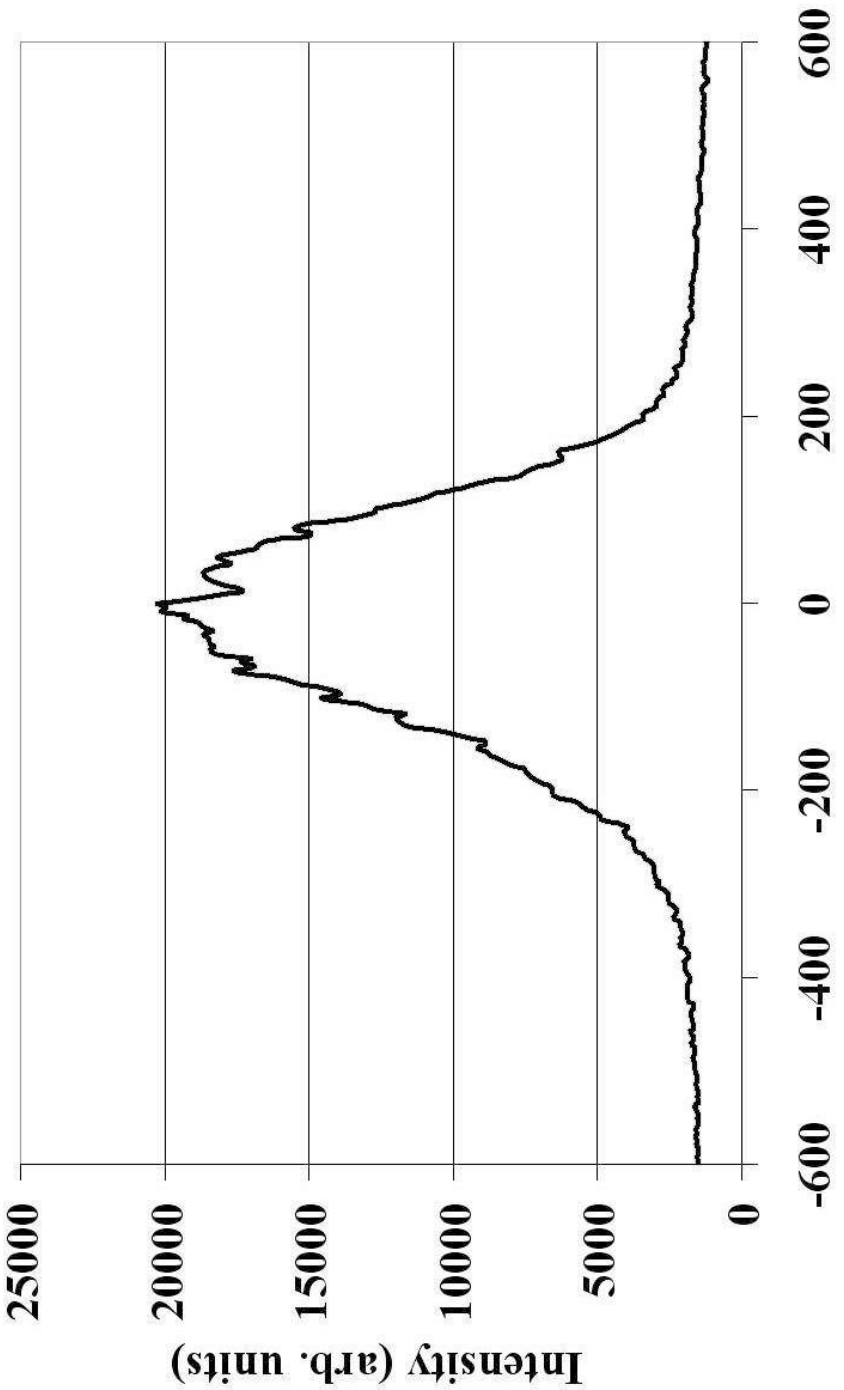

Figure 4.12: Typical line profile in the lateral direction across the peak of the EUV emission for a planar target. Zero represents the laser axis.

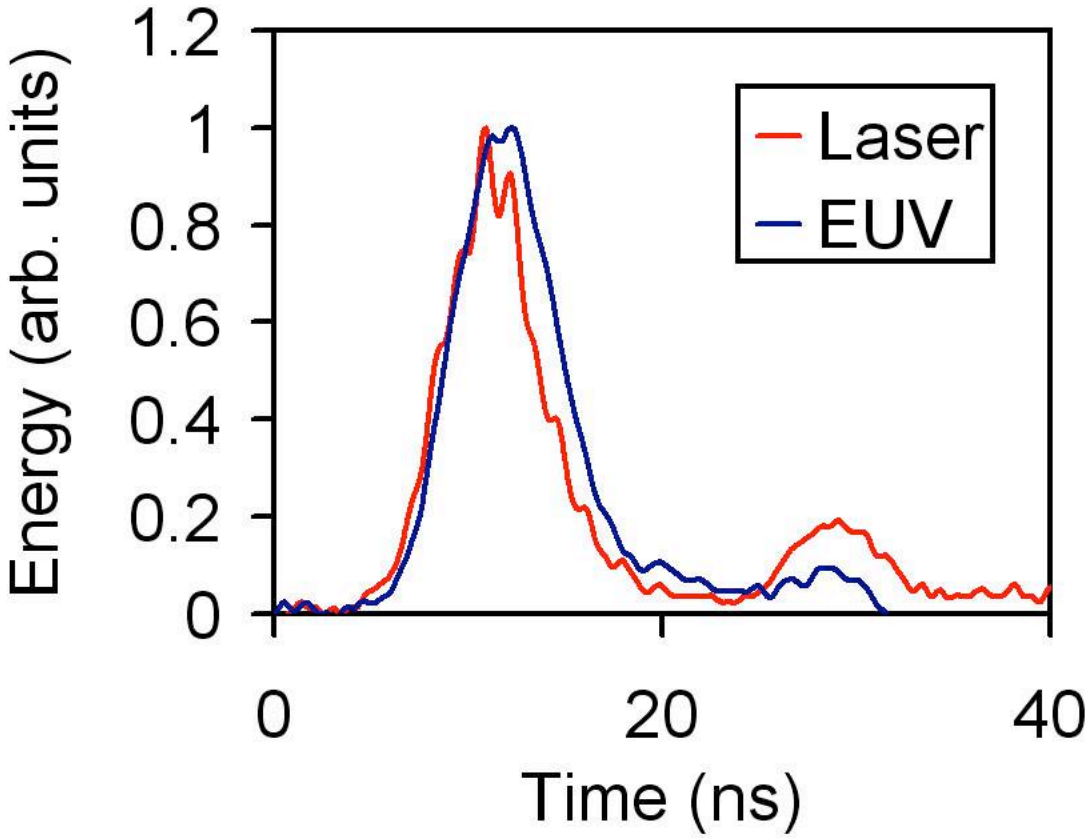

Figure 4.13: Comparison of the temporal shape of the laser pulse and the in-band EUV emission.

4.2. Spherical target

In this section the results of experiments conducted using spherical targets will be presented. Every effort was made to exactly reproduce the conditions of the planar target experiments, while only changing the target geometry. In Figure 4.14 the effects of target geometry can be seen. Here the CE for spherical targets of different sizes from Yuspeh et al is presented [100]. The laser focal spot size (FSS) was fixed at 80 μm FWHM and the sphere diameter (SD) was varied from 80 to 330 μm. Data for planar (slab) targets under the same irradiation conditions is also present. It is clear that the target geometry has a great deal of influence on the CE. All results shown in the sections to follow would be located at 3.5 SD/FSS in Figure 4.14. This ratio is centrally located on the plateau where the CE is highest for spherical targets. At this ratio spherical targets appear to emit about 15% more in-band EUV than planar targets. We will explore this phenomenon in the following sections.

4.2.1. Angular distribution of in-band EUV for spherical targets

The angular distribution of the in-band EUV emission for spherical targets was measured in the same manner as for the planar targets. Figure 4.15 shows the results of the measurements. It is evident that the dip between 5° and 45° is much larger for the spherical target. This dip reduces the overall EUV emission by about 5% compared to the planar target. In Figure 4.15 it can be seen that the in-band emission near 39° is almost identical for the two target geometries, instead of the planar target emitting less, this suggests that the in-band emission is about 5% lower for the spherical target, instead of higher, because of the larger dip in the angular distribution for spherical targets. This

discrepancy could be caused by the difference in the laser spot size in the two experiments.

Again examining the angular distribution it can be seen that there is also no second peak at 15° for the spherical distribution measurement. Instead the angular distribution is at a minimum near 15° for the spherical target. In a similar manner as described by the simple model for the planar target, there is highly absorbent plasma in what can be though of as a corner region of the plume far from the target surface and outside of the laser beam. This corner region plays a significant role in the dip at 30° for the planar target, and is even more important for the spherical targets.

As the laser heats the Sn of the target, the plasma expands outward normal to the surface. In the case of spherical targets, the normal expansion from the surface results in an angular spread of the plasma. Material flows from areas of high laser intensity to areas of low laser intensity. As the Sn leaves the path of the laser it cools and becomes more optically thick. This process has the greatest impact near 15°. As can be seen in Figure 5.2, the average charge state in the absorption region along the 15° path is around Sn^{9+}. This is the optimum charge state to absorb in-band emission. We have already seen that the charge states 9 through 11 are responsible for the large spectral dip seen near the in-band portion of the EUV spectrum. Again the density is an important factor here. Because the density is lower in the absorption region than in the emission region, the light absorbed is not emitted in equal quantities, resulting in a net loss.

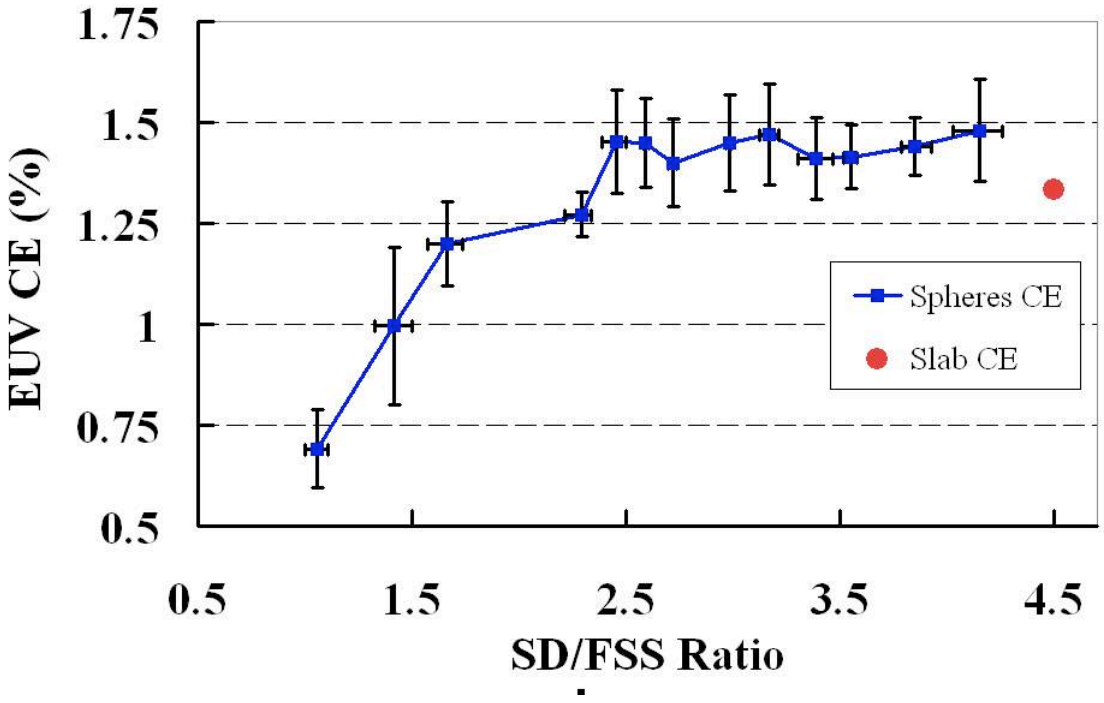

Figure 4.14: The effect of sphere diameter to focal spot size ratio on in-band CE. Data for slab targets is shown for comparison. Adapted from Yuspeh et al [100].

It should also be noted here that the error is much larger for the spherical targets than for the planar targets, and that the integrated in-band spectra were not included in Figure 4.15 as it was for the planar target data. For spherical targets the alignment is critical for repeatable measurements. To acquire repeatable data with spherical targets the laser axis and target center must be aligned within a few tens of microns or better. However for planar targets a misalignment of several hundred microns does not cause a significant change in the E-Mon reading. The requirements on the concentric alignment of the laser and target make it difficult to acquire repeatable spectra intensities, since the TGS is extremely sensitive to alignment. Additionally changes in angular alignment for the angular distribution measurements were also more complicated in that there are an infinite number of angles normal to a spherical surface, and there is only one for each side of a planar target. The combination of the various difficulties in aligning the laser for spherical targets leads to more error in both the EUV emission and angle measurements, as well as making the selection of the angles measured more difficult.

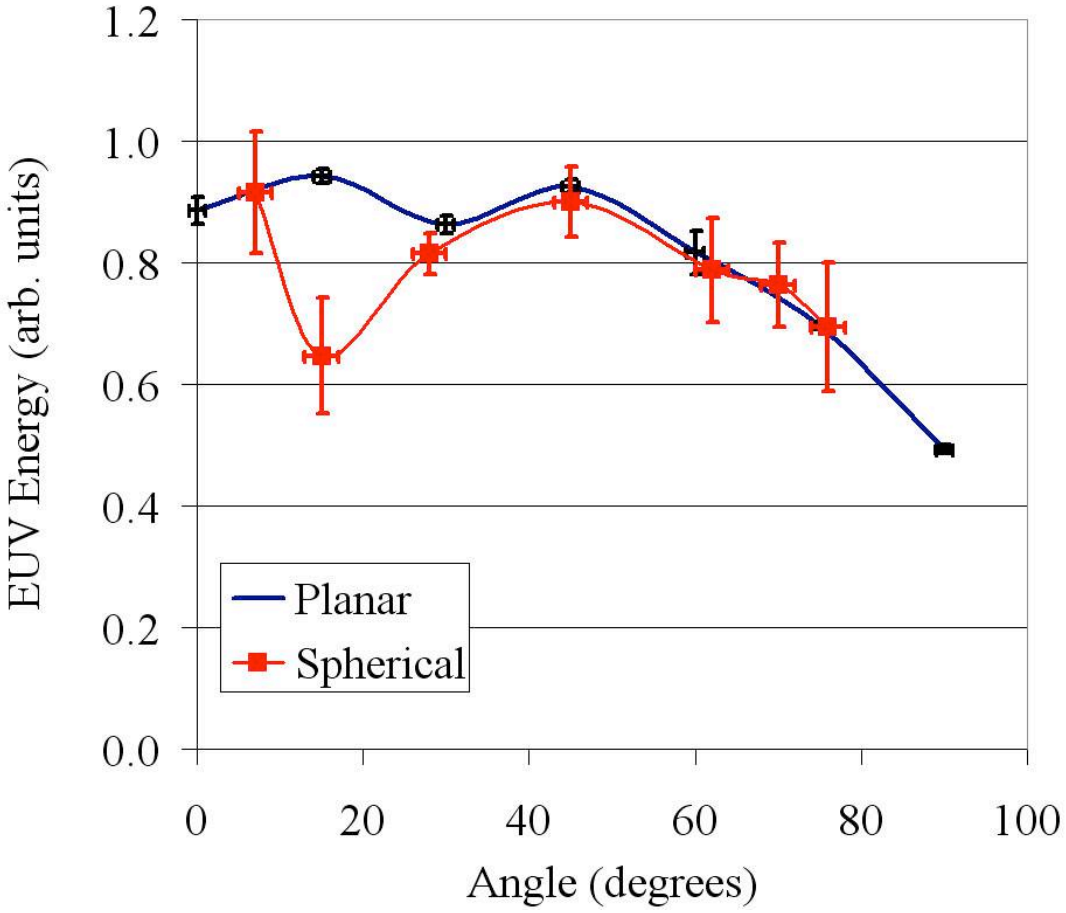

Figure 4.15: Angular distribution of spherical targets with the planar target distribution for comparison. 0° is along the laser axis.

4.2.2. Angular dependence of EUV Spectrum for spherical targets

The in-band EUV spectrum for spherical targets was measured at various angles: 14°, 20°, 28°, 45°, 62°, 75°, and 83°. The irregular angular spacing is attributed to the increased complexity in the alignment for spherical targets in comparison to planar targets. Top priority was given to centering the laser beam on the sphere.

The general trend for the spherical target is the same as the planar case. As the angle with respect to the laser increases from 0° to 45° the spectrum remains broad where the longer wavelengths are a significant portion of the EUV light. The dip near the in-band region is also present for the spherical targets for these angles. Once the angle is greater than 45°, the spectrum begins to narrow as the long wavelengths drop in intensity.

There are some differences however; one is that the dip at the in-band portion of the spectrum is reduced at 15° for the spherical target. There is a very strong dip in the spectrum for the planar target. At first this may seem odd since the in-band energy at 15° is much lower for the spherical target. The explanation is that the plasma absorbing the EUV is significantly different between the two target geometries. As discussed in the previous section, the ions expand faster laterally when the target surface is spherical, resulting in significantly different absorption coefficients along the path. The absence of the strong dip for the spherical targets indicates a lower abundance of Sn^{9+} - Sn^{11+}. Although these ions are responsible for the spectral dip, they are also responsible for the in-band emission. Here the density plays a key role in the emission and absorption process. When the density is high, as it is for a planar target, these ions act to absorb the in-band emission. When the density is lowered, as it is for spherical targets, the

absorption of the in-band emission is reduced. The reason the spherical target produces less in-band light without a large spectral dip is that the absorption is more uniform over the EUV range, but greater than the in-band absorption for planar targets.

When comparing the spectra at 20° for the spherical target to the spectra at 15° for the planar target, it can be seen that they are nearly identical. The 0° and 15° spectra for the planar and spherical targets respectively are also very similar. This may also be an effect of the increased lateral expansion caused by the curved spherical surface. When the plasma expands from the planar surface, the initial direction is 0°. The plasma expands laterally only due to pressure inside the plasma, but close to the laser axis the expansion is minimal. However, when the plasma expands from the spherical surface, there is significant lateral expansion caused by the curvature of the target. Plasma that would continue along the laser axis for the planar target instead travels at an angle corresponding to the normal of the target surface. A 5° change in the emitting plasma properties would not be unreasonable, and could account for the similarities of the spectra at 20° and 15° for the two different target types.

The EUV spectrum will be discussed in greater detail in the next chapter. There the measured spectra will be compared to simulated spectra produced from a combination of a two dimensional radiation hydrodynamic code and an atomic physics, collisional radiative code.

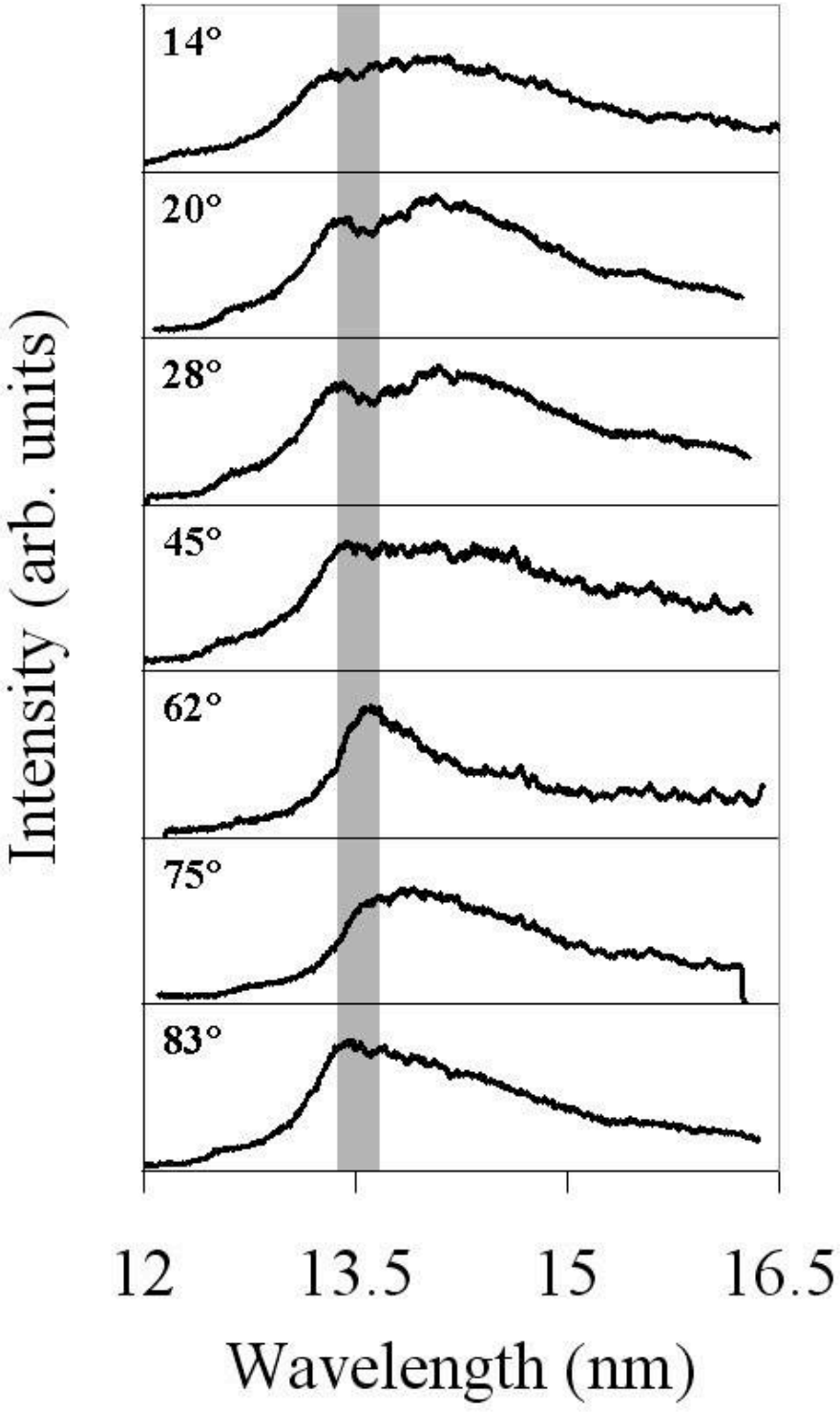

Figure 4.16: Angular dependence of EUV spectra for spherical targets

4.2.3. Plasma density measurements for spherical targets

As with planar targets, the electron density was measured at several times during the laser pulse. When a planar target is illuminated with a laser, the regions close to the laser axis expand almost normal to the target surface. The outer regions act to confine this inner plasma allowing the density to remain high. As can be seen in Figure 4.17, Figure 4.18, and Figure 4.19 the plasma expansion closely follows the shape of the target surface. There is a nearly uniform expansion of the plasma in both the lateral and longitudinal directions, unlike for the planar target where the plasma expands more along the laser axis.

The expansion of the plasma lateral to the laser beam reduces the density in the inner regions of the plasma, reducing the time that the ions are heated by the intense portion of the laser. The ions are first heated by the laser, and then travel outward, cooling, increasing the absorption coefficient of the plasma in the region that corresponds to the corner of the simple model diagram shown in Figure 4.4. This lateral transport of ions, caused by the target geometry, is responsible for the large dip seen in Figure 4.15.

It can also be seen in Figure 4.20 that the density along the laser axis is slightly lower for the spherical targets and that the scale length is shorter. The plasma scale length for a planar target was reported earlier to be 160 μm. Spherical targets have a slightly shorter scale length of 135 μm. With a shorter scale length, spherical targets should emit more in-band emission, because the absorption should be lower. However, the lateral transport of the ions to lower laser intensities decreases the efficiency of the

plasma heating. These two effects act to cancel one another out so that the in-band CE measured at 45° is nearly the same for the two target geometries.

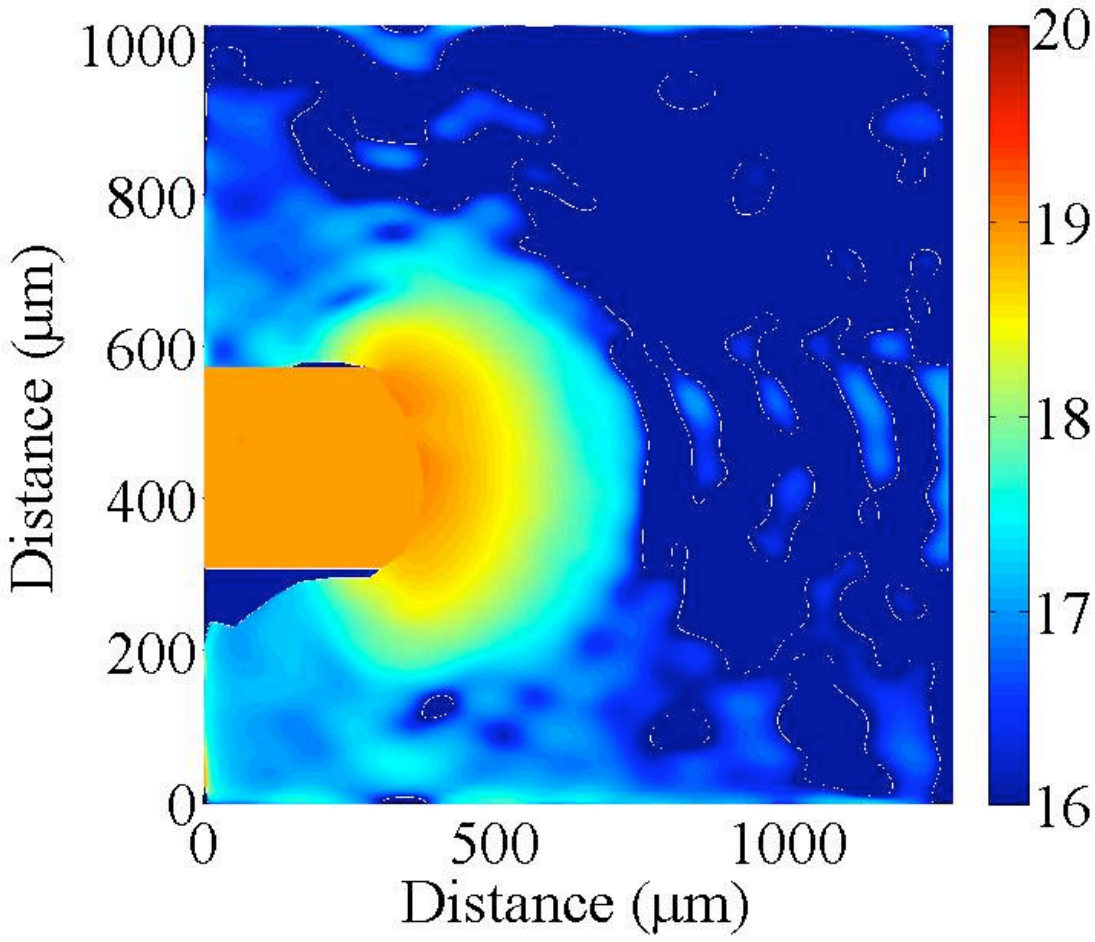

Figure 4.17: Typical electron density 4 ns before the laser peak. The color scale is $\log_{10}(n_e\ cm^{-3})$.

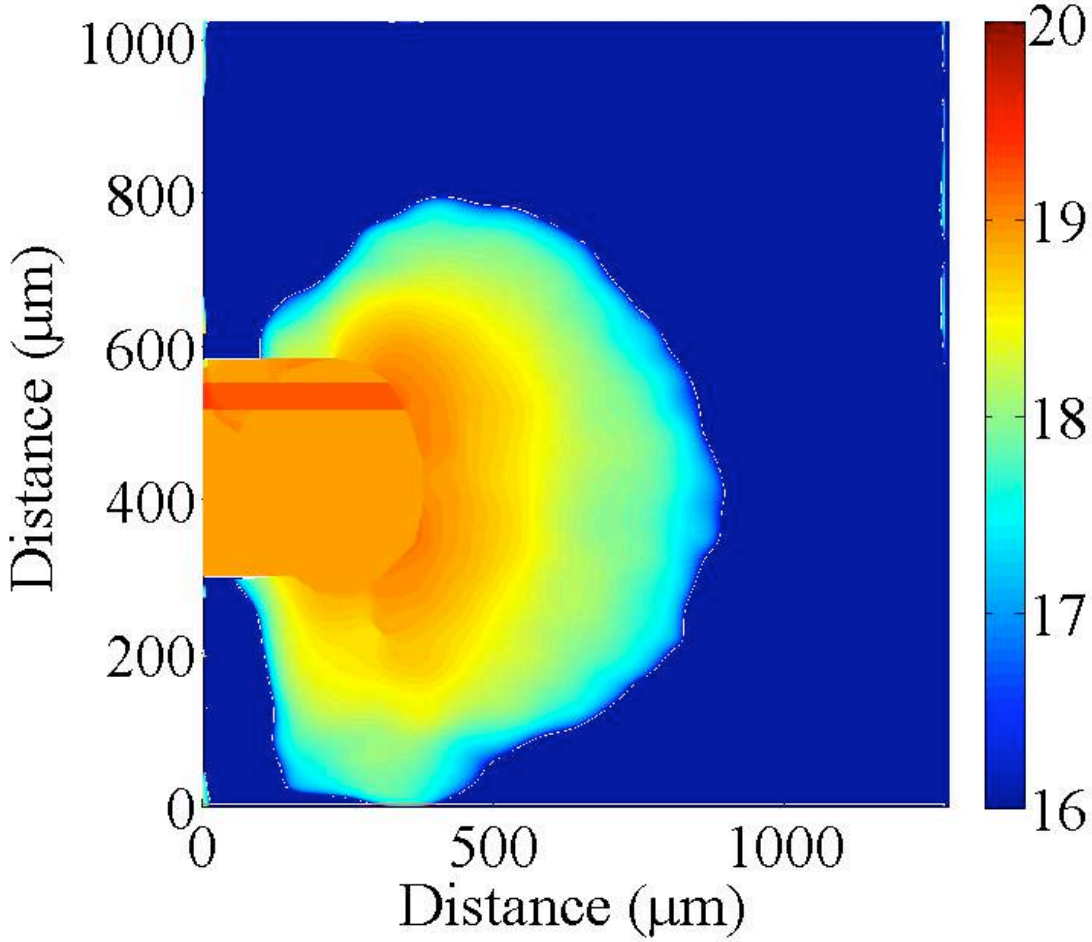

Figure 4.18: Typical electron density at the laser peak. The color scale is $\log_{10}(n_e\ cm^{-3})$.

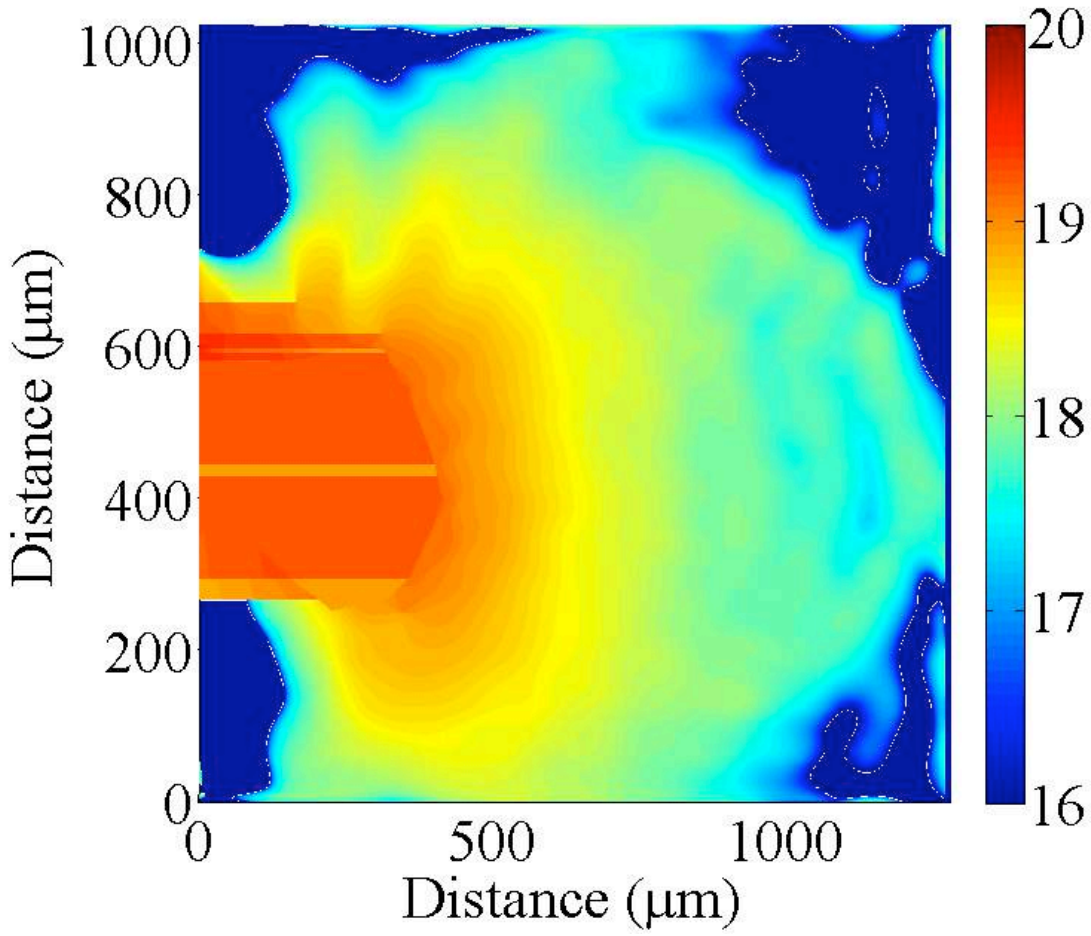

Figure 4.19: Typical electron density 4 ns after the laser peak. The color scale is $\log_{10}(n_e\ cm^{-3})$.

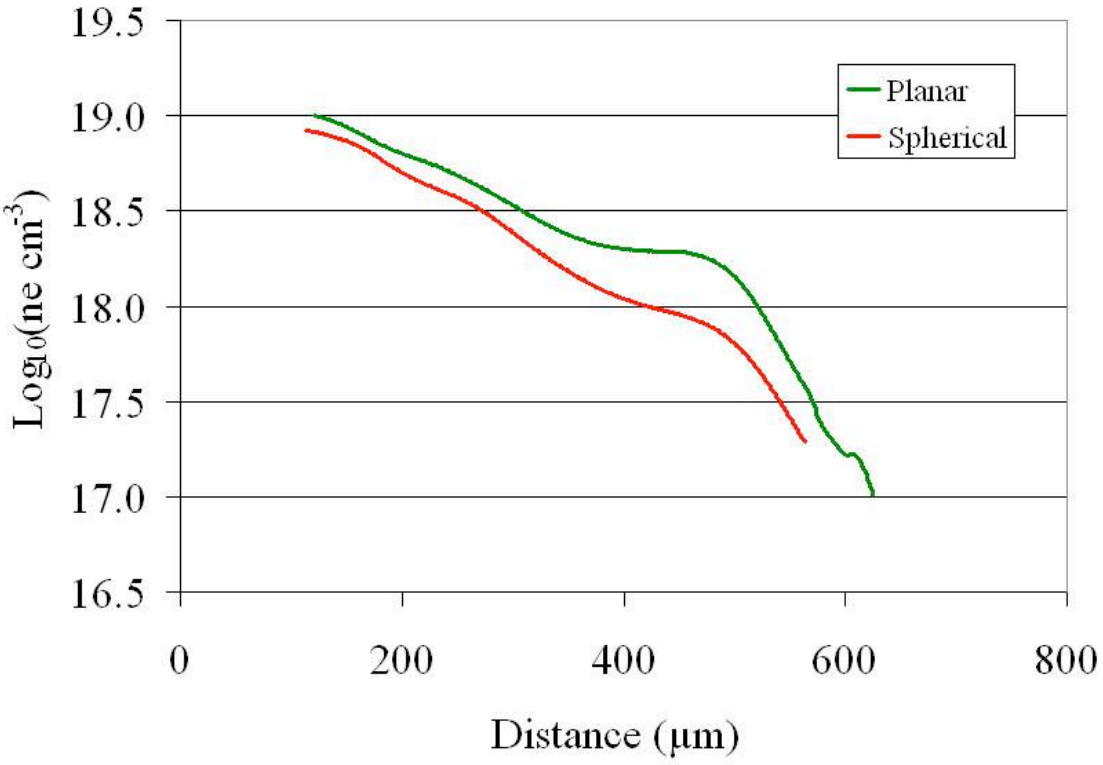

Figure 4.20: Comparison of the electron density along the laser axis at the peak of the laser pulse for planar and spherical targets.

4.2.4. EUV imaging for Spherical targets

In-band EUV images were acquired during the same set of experiments as the images acquired for the planar targets. Figure 4.21 shows a typical in-band image for a spherical target. There is no discernable difference between the images for planar and spherical targets. This indicates that the laser absorption occurs at the same location relative to the target surface and that the heated plasma volumes are similar. As described earlier the images are collected at 90° to the pump laser axis. From the spectra and E-Mon measurements of the two targets at this angle it is clear that the radiation transport in this direction is very similar for both targets. It is likely that images acquired at angles such as 15° or 20° would not be so similar between the two targets, based on the other diagnostics.

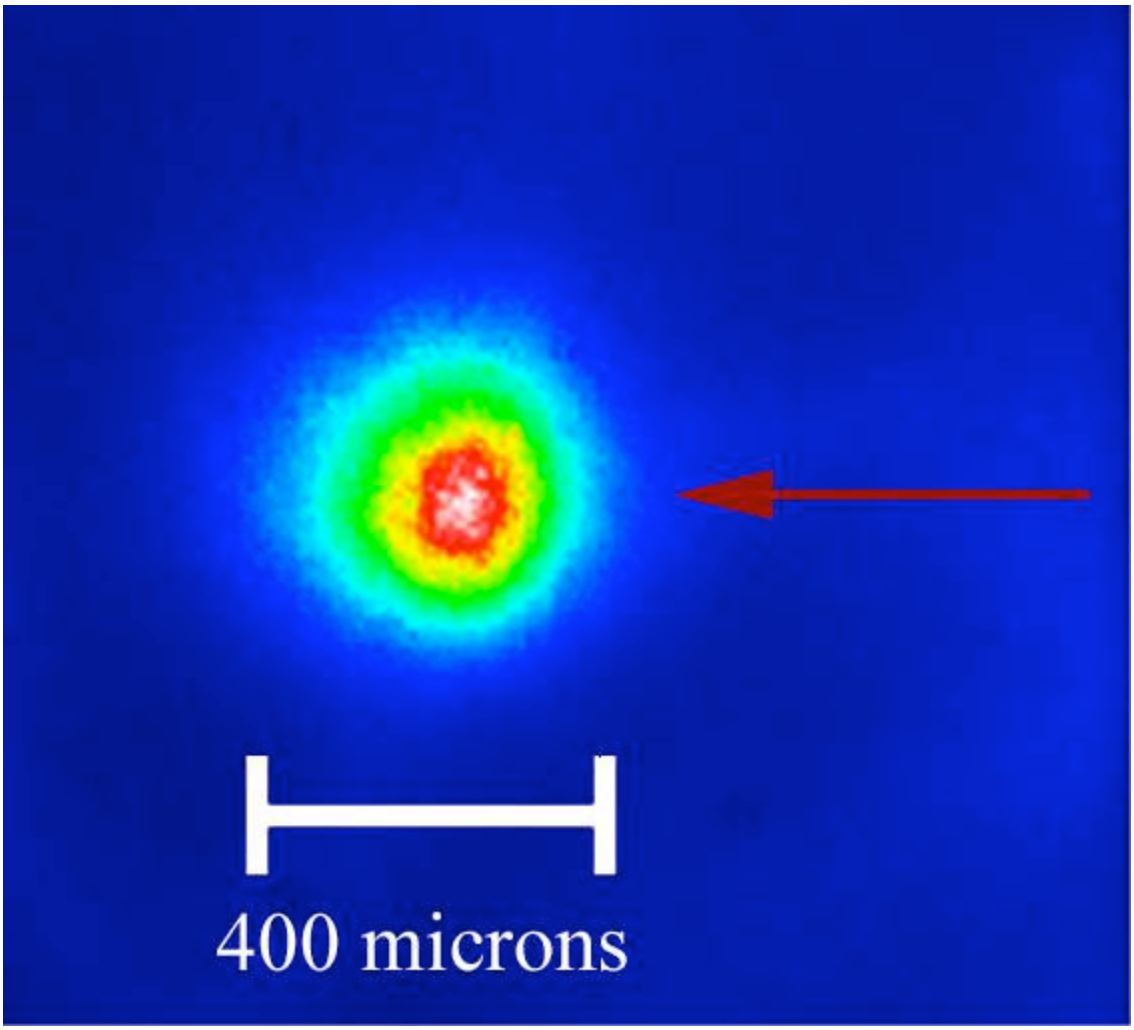

Figure 4.21: Typical time integrated in-band EUV emission from a spherical target. The arrow indicates the laser incidence.

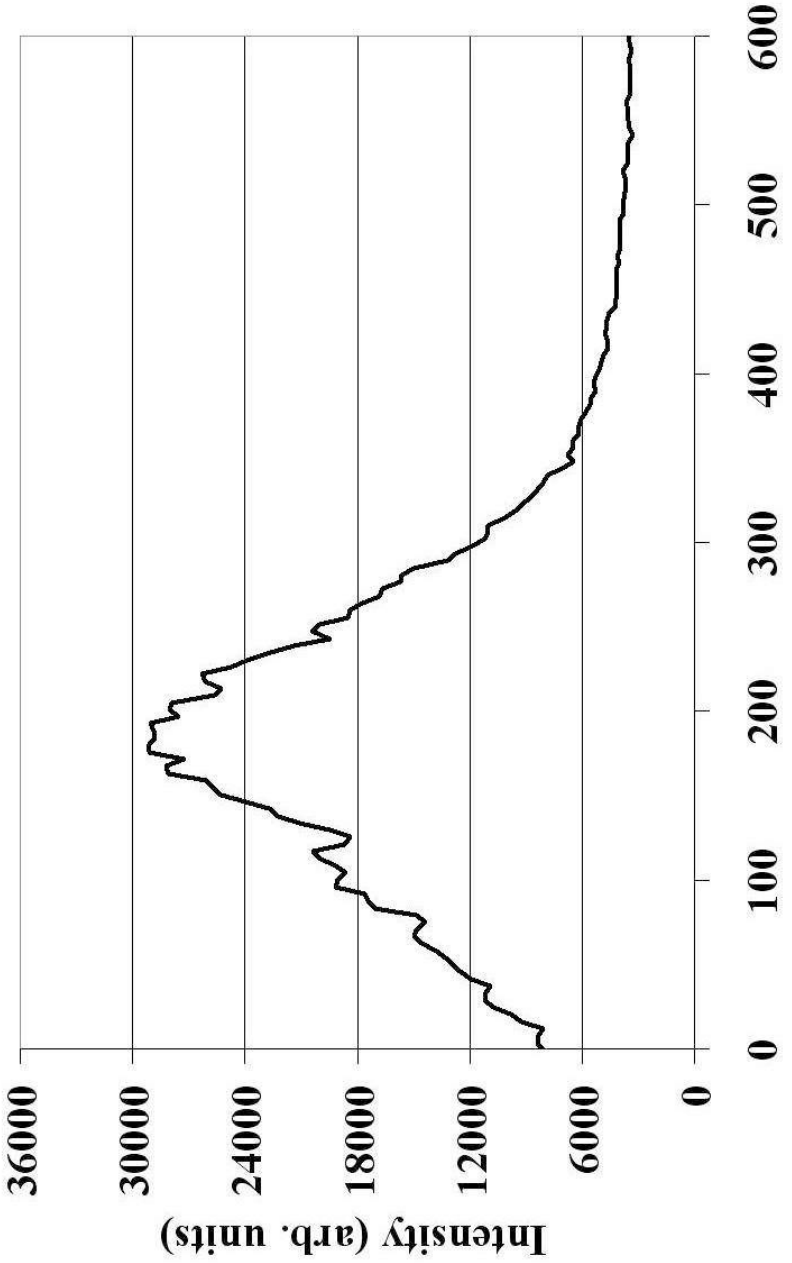

Figure 4.22: Typical EUV line profile along the laser axis for a spherical target. Zero represents the target surface.

5. Two-dimensional numerical simulations

5.1. Introduction

For small scale laser produced plasmas such as those in this work, there is no good way of measuring the plasma temperature directly. Techniques involving spectroscopy are not reliable here because of the non-LTE nature of the problem. Moreover these techniques are not spatially resolved, and only provide temperature measurements as deep as one optical depth. In order for Thomson scattering to be useful the plasma scale must be significantly larger than the plasmas produced in this work because of the small scattering cross section. The diagnostic limitations on direct measurements of the electron temperature makes two-dimensional modeling a valuable tool for understanding the plasma dynamics and radiation transport.

In this section, two-dimensional radiation hydrodynamic simulations using h2d will be discussed. Only results for spherical target geometry are presented. Attempts to simulate planar geometry have been unsuccessful due to computational mesh problems. The computational mesh implemented in h2d is Lagrangian. As the plasma expands, the mesh follows the fluid so that the mass in each zone remains constant. The geometry of a planar target causes a "bowtie" in the mesh near the edge of the laser beam. Bowties occur when the mesh nodes cross one another so that two zones occupy the same space. When a bowtie occurs in h2d, the problem must quit and in most cases can not be resumed. When the target material is in a planar geometry a bowtie will occur before the laser can reach peak intensity, making the simulation of little use. Many steps were taken

to resolve this problem, but the effort was unsuccessful. However, spherical target geometries have been modeled with great success and are presented here.

5.2. Two-dimensional plasma property calculations

There is only one fundamental plasma parameter that can be both modeled and measured directly in the experiment, the plasma electron density. In Figure 5.1 the plasma density calculated in h2d is directly compared to the experimental measurement. The comparison is made at the peak of the laser pulse, when the EUV emission is maximum. It is clear that the two are very similar. First, both the longitudinal and lateral expansions are in agreement so that the simulation and the data are near mirror images of one another where the density is below a few 10^{19} cm^{-3}. The density gradients along each axis are also in agreement in this density range. Densities above this level are beyond the limits of the diagnostic capabilities for the experiment.

Figure 5.1 also contains the EUV image contours as well as the absorption region thickness lines from Figure 4.10. Here it is clear that the peak of the EUV emission is located in the region of the plasma where the density is in the high 10^{18} cm^{-3} range. The interesting thing here is that the emission comes from a large range of densities, from above the critical density for the pump laser, 10^{21} cm^{-3}, to as low as a few 10^{17} cm^{-3}. This result shows that the emission occurs within a large range of densities, and that the most intense emission comes from a density near 10^{19} cm^{-3}.

The absorption region thickness lines, from Figure 5.1, also show that the simple model gives a reasonable prediction of the thickness of the absorbing plasma. The plasma becomes optically thin when the density is below a few 10^{17} cm^{-3}. In Figure 5.1

the absorption region thickness line in the lateral direction, corresponding to the side absorption region in the simple model, extends from the emission region to where the plasma is a few 10^{17} cm^{-3}. In this direction the model was able to accurately predict the absorption region thickness. If we compare the absorption thickness along the laser axis, we see that the model predicted a much shorter absorption region. The measured density profile indicates that this region should be almost twice the thickness as predicted by the model. Figure 4.10 showed that the model was able to predict accurately the length of the emission region along the laser axis. It is this length and the thickness of the side absorption region, which was accurately predicted by the simple model, that determine the lateral contribution of the total angular emission shown as the purple dashed line in Figure 1.1. In other words the model accurately described the important factors for the radiation transport in the lateral direction. However, the model was not as accurate in the longitudinal direction. In this direction the emission is determined by the lateral length of the EUV emission region, which was over predicted by the model, and by the thickness of the absorption region in the longitudinal direction, under predicted by the model. The explanation for this can be found in the average charge state, $\overline{Z}$. Figure 5.2 shows $\overline{Z}$ at the peak of the laser pulse as calculated by h2d, along with the EUV contours and absorption thickness lines. It can be seen that $\overline{Z}$ is nearly uniform through out the entire side absorption region, and is around 7. The plasma opacity is heavily dependant on the ionization state of the atoms, and low charge states, at or below 7, do not have strong absorption lines at the in-band wavelengths. Therefore it is not unreasonable to assume a uniform absorption coefficient, as the simple model does, for the side absorption region. The same can not be said for the absorption region along the laser path. In Figure 5.2 it

can be seen that $\overline{Z}$ ranges from around 8 to 11. These charge states have very different opacities for the in-band emission. The model could not accurately predict the relevant scales because it uses a single absorption coefficient which does not adequately describe the absorption along the laser path. An improved model would implement a more refined spatially resolved absorption coefficient. However to keep the model simple, this approach was not pursued.

It is worth noting that the outer regions of the plasma have a charge state of 10 or above. These ions do not contribute to the total in-band emission in any significant way. As can be seen in Figure 5.1 the electron density is below 10^{17} cm^{-3} over 500 μm from the edge of the simulated plasma. These outer most regions have densities as low as a few 10^{14} cm^{-3}, but the color scale is limited to 10^{17} cm^{-3} for comparison to the experimental data. At such low densities, the emission from these regions will be several orders of magnitude lower than those of the plasma core. The temperature in these outer regions is only a few eV. The high charge state is achieved due to the extremely low density.

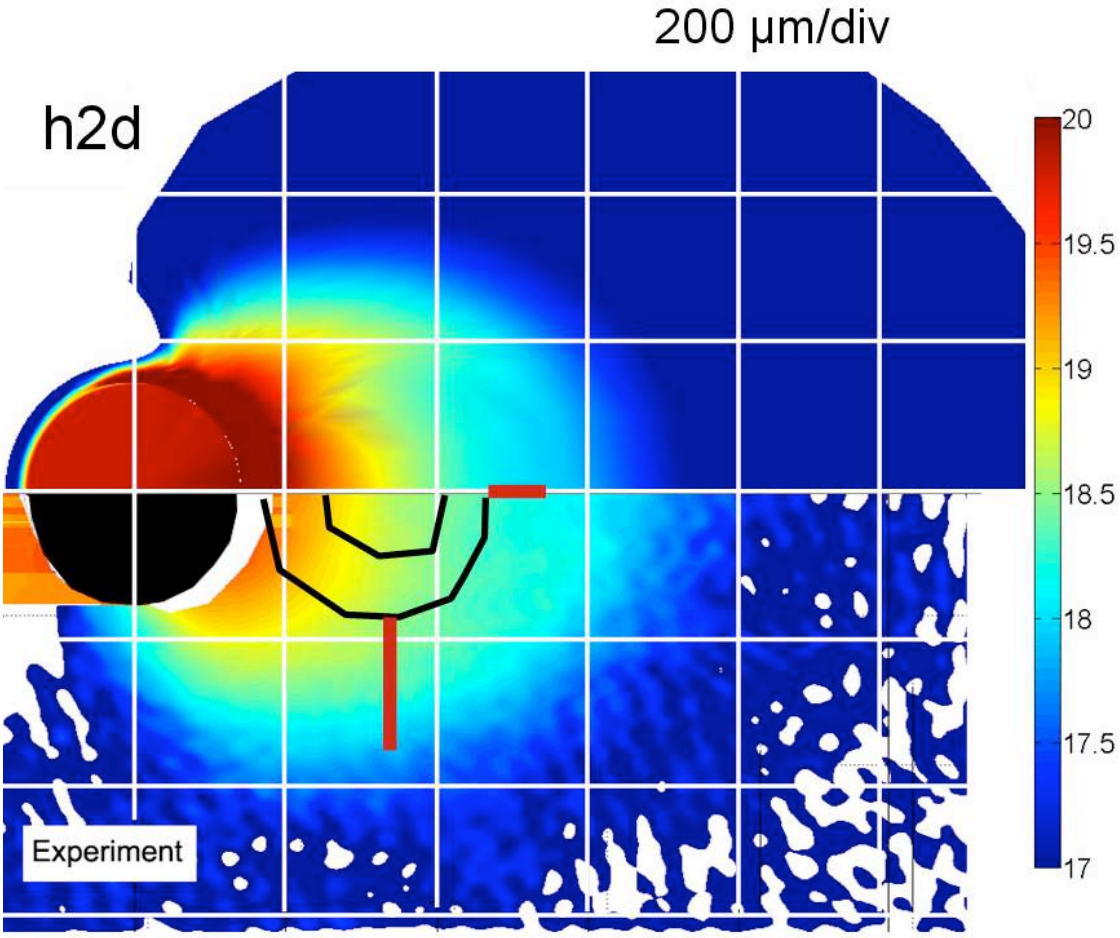

Figure 5.1: Comparison between h2d and experiment of the electron density at the laser peak. The color scale is $1og_{10}(n_e\ cm^{-3})$. Black contours indicate the in-band EUV emission region, and red lines indicate the absorption region calculated from the model in 4.1.1.

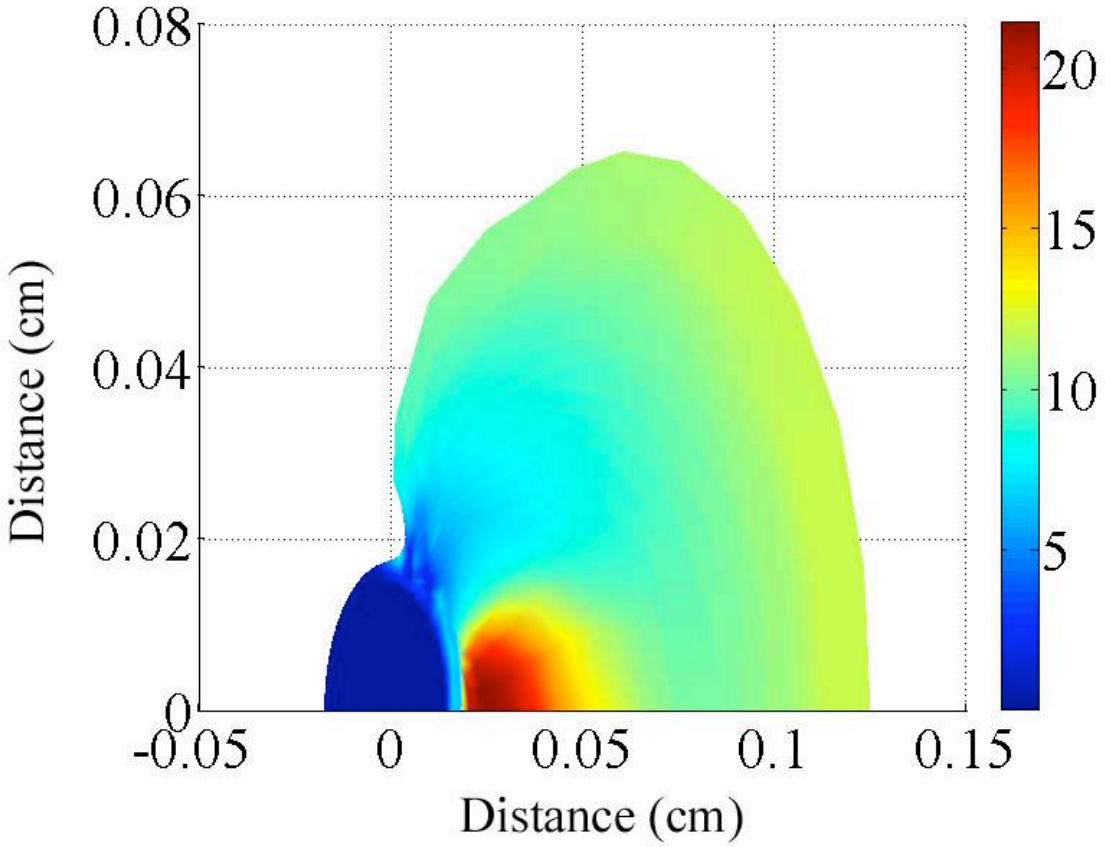

Figure 5.2: h2d simulation of the average charge state of the plasma.

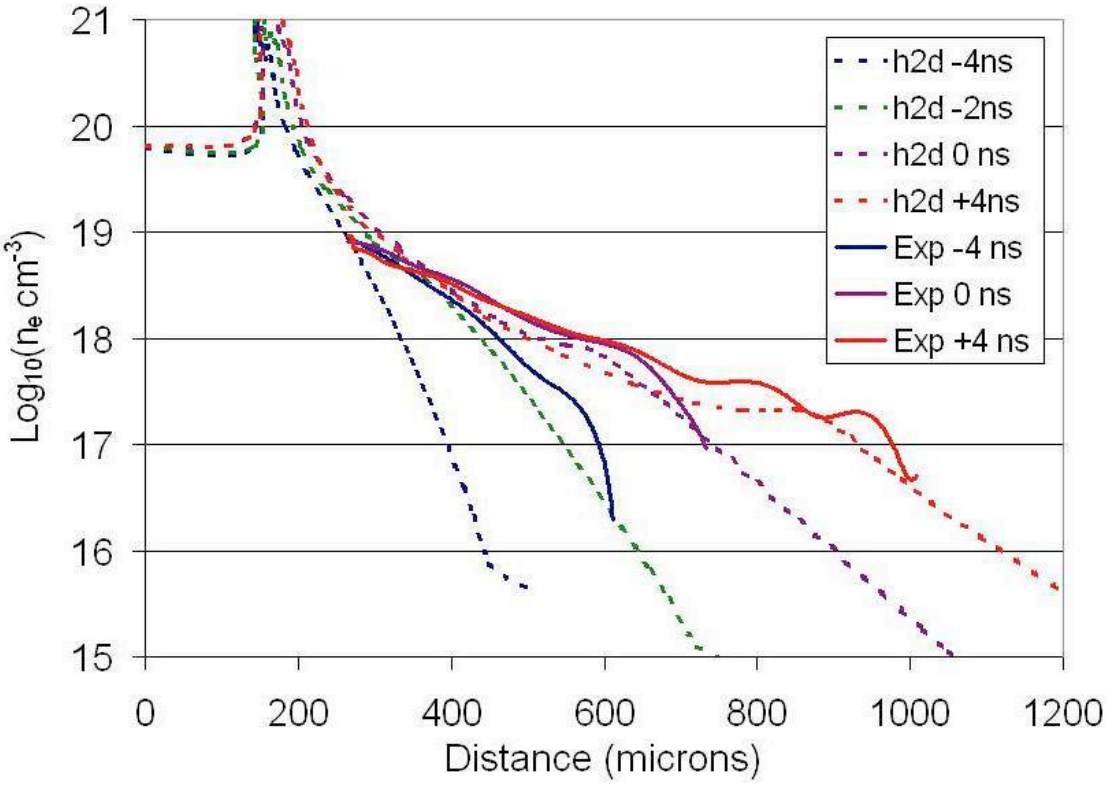

Figure 5.3: Line profiles of the electron density along the laser axis at various times for both h2d and experiment.

5.3. Analysis of two-dimensional simulations

One of the advantages of h2d is that the temporal evolution of the plasma properties can be studied. We have already shown that h2d accurately models the plasma electron density at the peak of the laser pulse. In Figure 5.3 the electron density evolution along the laser axis calculated by h2d and measured from the experiment is presented. It is clear that h2d accurately calculates the electron density near and after the laser peak. However, during the very early portion of the laser pulse h2d underestimates the plasma expansion. The best explanation for this is that the laser pulse is 7 ns FWHM and the peak of the pulse occurs at 7 ns into the simulation. Therefore the laser intensity is already at about 7% of the maximum at the start of the simulation; resulting in a small portion of the laser energy being lost. This, of course, does not happen in the experiment, so the plasma actually has a little more time to develop than is given in the simulation. As more laser energy is dumped into the target, the small difference at the beginning of the problem becomes insignificant. From the density profiles in Figure 5.3, we can have confidence that the simulation adequately describes the plasma evolution after several ns of laser irradiation.

In Figure 5.4 the plasma electron temperature evolution is presented. The peak of the laser pulses occurs at t = 0 ns. Again the laser is incident from right to left and is centered on the x-axis of the plots. From the figure it is clear that even 4 ns before the laser peak, the plasma temperature is high enough to produce EUV emissions. As the laser intensifies, the plasma expands outward and the core temperature rises. For several ns around the laser peak intensity the core plasma temperature profile remains nearly constant. The plasma temperature then begins to fall as the laser intensity decreases.

It is clear that the plasma is overheated in the core where the temperature reaches above 60 eV, whereas the optimum temperature for in-band EUV production is around 30 eV. At first it may seem obvious that overheating the plasma would reduce the in-band CE. However, in this case the overheating is necessary to achieve the highest CE. The majority of the incident laser energy is absorbed near the critical density, 10^{21} cm^{-3}. The density is several orders of magnitude too high for the in-band emission to escape from this region. If the laser intensity is reduced so that the peak temperature is near 30 eV, nearly all of the in-band energy produced in that region will be absorbed. Overheating the plasma to 60 eV in the high density region sets up a temperature gradient so that the optimum plasma temperature corresponds to the optimum density. The extra energy used to overheat the plasma core is not completely wasted. As seen previously in Figure 4.13, the in-band EUV continues to emit as the laser pulse decays. The energy deposited in the plasma core is lost to the surrounding material, lowering the laser energy needed to maintain the proper temperature in the emitting region. In the process of the core cooling the emitting region is held at the proper conditions for in-band production. If this did not occur the EUV temporal profile would match that of the laser, and would not persist for an extra ns after the laser pulse.

From the experiment we know that the in-band emission continues for approximately 1 ns longer than the laser pulse, and from h2d we know how the plasma temperature evolves as the laser heats the Sn. One of the determining factors for the intensity of the in-band emission is the amount of plasma at the appropriate conditions for production. Using temperature profiles like those in Figure 5.4 it is possible to determine the area occupied by any given plasma temperature as a function of time. It is the cross-

sectional area that is of interest here, as the detectors in the experiment see the plasma in this way. In Figure 5.5 the cross-sectional areas of different plasma temperatures as a function of time can be seen. The areas are calculated by integrating inside the contours at each temperature. With the laser axis being the axis of symmetry, one could visualize the plasma as an onion. Each layer of the onion represents a different plasma temperature. Integrating inside the contours of the plasma temperature is like pealing away each layer of the onion and measuring the cross-section of what remains.

Figure 5.5 clearly shows that the area of the peak plasma temperature remains nearly constant for several ns. Lower temperatures have shorter periods of constant area, until finally at 20 eV there is no longer stagnation in the area. From this figure it can also be seen that the 20 eV plasma area follows the temporal pulse shape of the in-band EUV emission with a FWHM of about 1 ns longer than the laser pulse. Note that the 30 eV plasma has a FWHM equal to the laser pulse. This is evidence that the majority of the in-band emission detected in the experiment is produced in the region of the plasma where the temperature is around 20 eV.

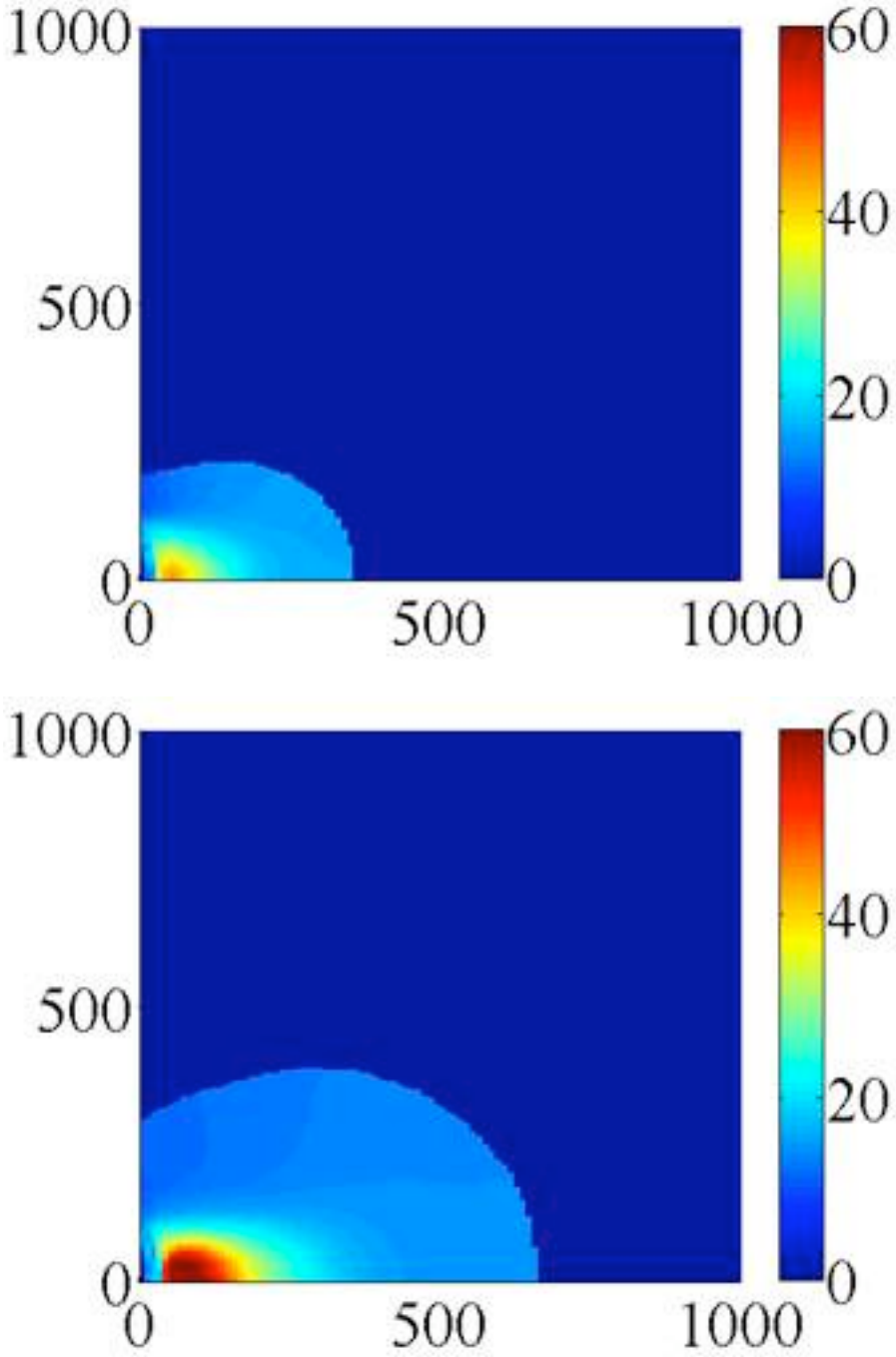

Figure 5.4: Plasma electron temperature at -4, -2, 0, 2, 4, and 6 ns. 0 ns is the peak and the color scale is temperature in eV and the spatial units are microns.

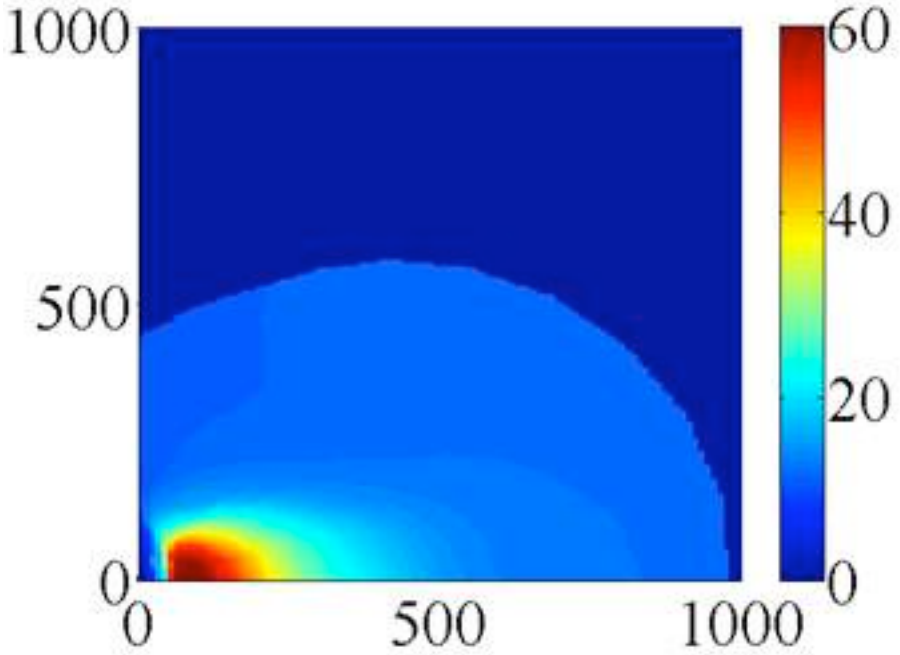

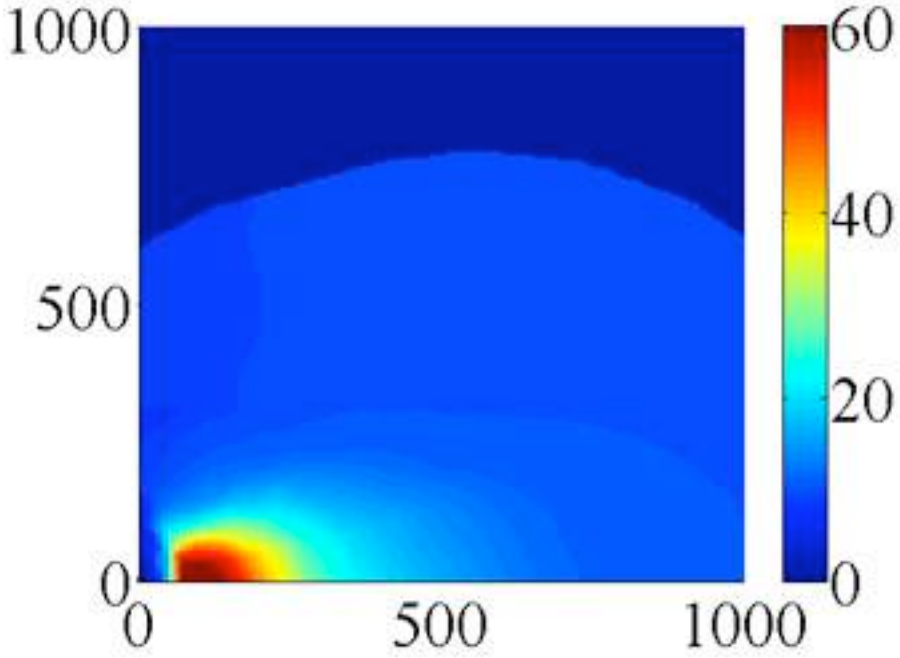

Figure 5.4 continued

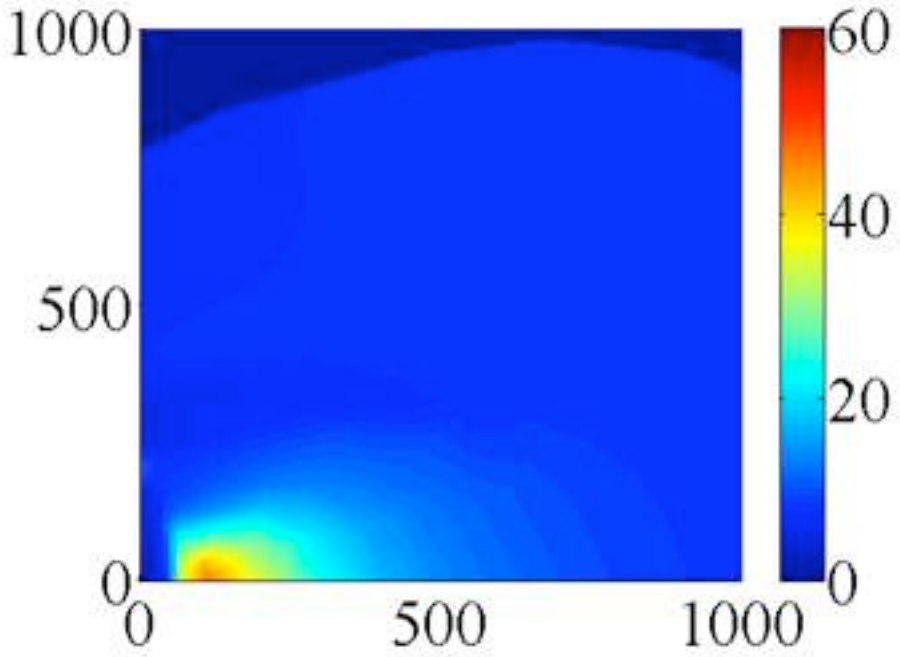

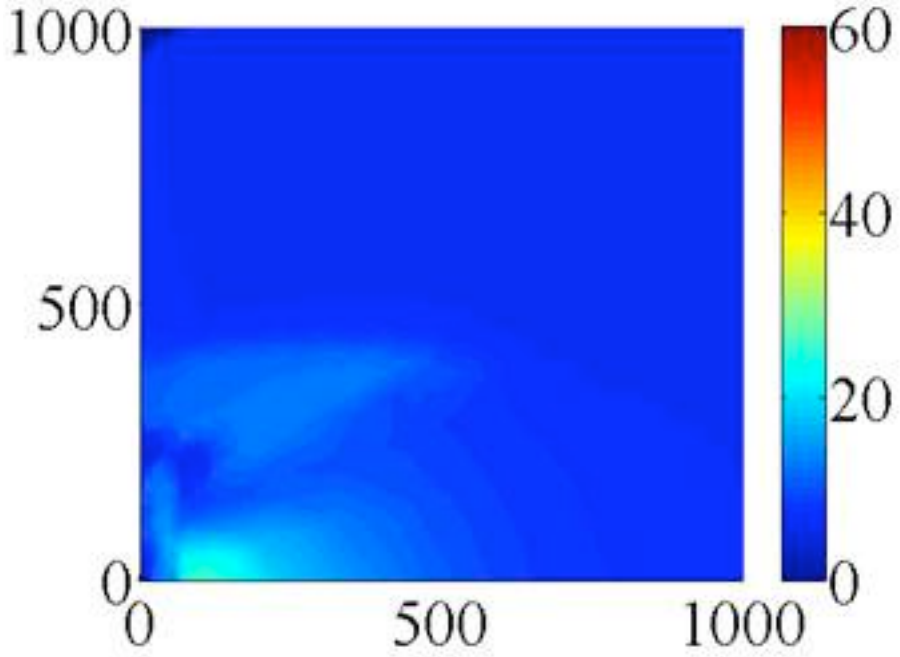

Figure 5.4 continued

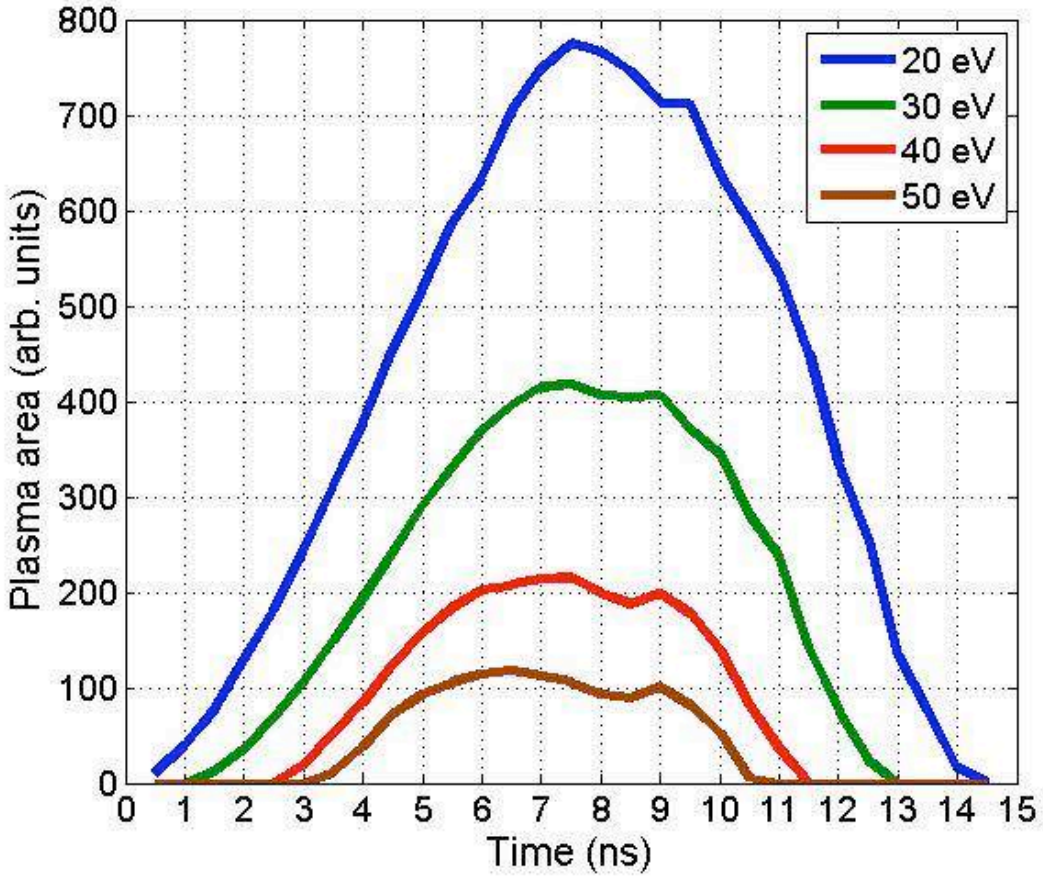

Figure 5.5: Cross sectional area of plasma with various electron temperatures during the laser pulse. Here the laser peak occurs at 7 ns and has a FWHM of 7 ns.

In chapter 4 the results from the time integrated EUV imaging system were presented. This data can be compared to the h2d modeling results to gain further understanding of the effects of the electron density and plasma temperature on the emission. Because the diagnostic has no time resolution, the modeling results must be converted to a time integrated form for comparison. This can be accomplished by calculating the plasma temperature persistence. It is fairly well publicized that the optimum emission for in-band EUV occurs when the plasma temperature is around 30 eV [49, 65, 95]. Therefore knowledge of the lifetime of 30 eV plasma as a function of distance from the target surface provides insight into the spatial distribution of the EUV.

The plasma temperature persistence is calculated from the h2d temperature profiles by checking for the existence of plasma at or above a certain temperature at each point in space using the same 2-D contours areas used in Figure 5.5. At each time step if the temperature exceeds the minimum value a count is added to the total for that position. Twenty-nine snapshots spaced by 0.5 ns starting at 0.5 ns up to 14.5 ns were used in this calculation.

A comparison of the plasma temperature persistence and the in-band EUV image is presented in Figure 5.6. Immediately it can be seen that the extent of the EUV emission is of the same scale as the 20 eV plasma, and not the 30 eV plasma. Higher temperatures have an area smaller than the EUV region, indicating that the EUV must be produced in the region of the plasma that is around 20 eV.

Additionally the EUV peak location does not correspond to the position of the peak temperature. In Figure 5.7 the plasma temperature persistence at 20 and 30 eV are shown with the line profile of the EUV image along the laser axis. The plasma electron

density, from the h2d simulation, at the peak of the laser pulse is also shown. In this figure it is clear that the plasma temperature remains at the optimal levels for the longest time, 100 μm from the target surface, and the EUV peaks at 180 μm from the target surface. If temperature alone were the determining factor for in-band emission, then these two peaks would occur at the same location. Once the electron density is accounted for the picture becomes clearer. The peak of the EUV occurs where the plasma density is around 10^{19} cm^{-3}. As the plasma density increases towards the target surface, the absorption also increases to the point where the increased production by the longer persistence of the plasma temperature is over come by absorption. This leads to a decline in the detected emission closer to the target surface.

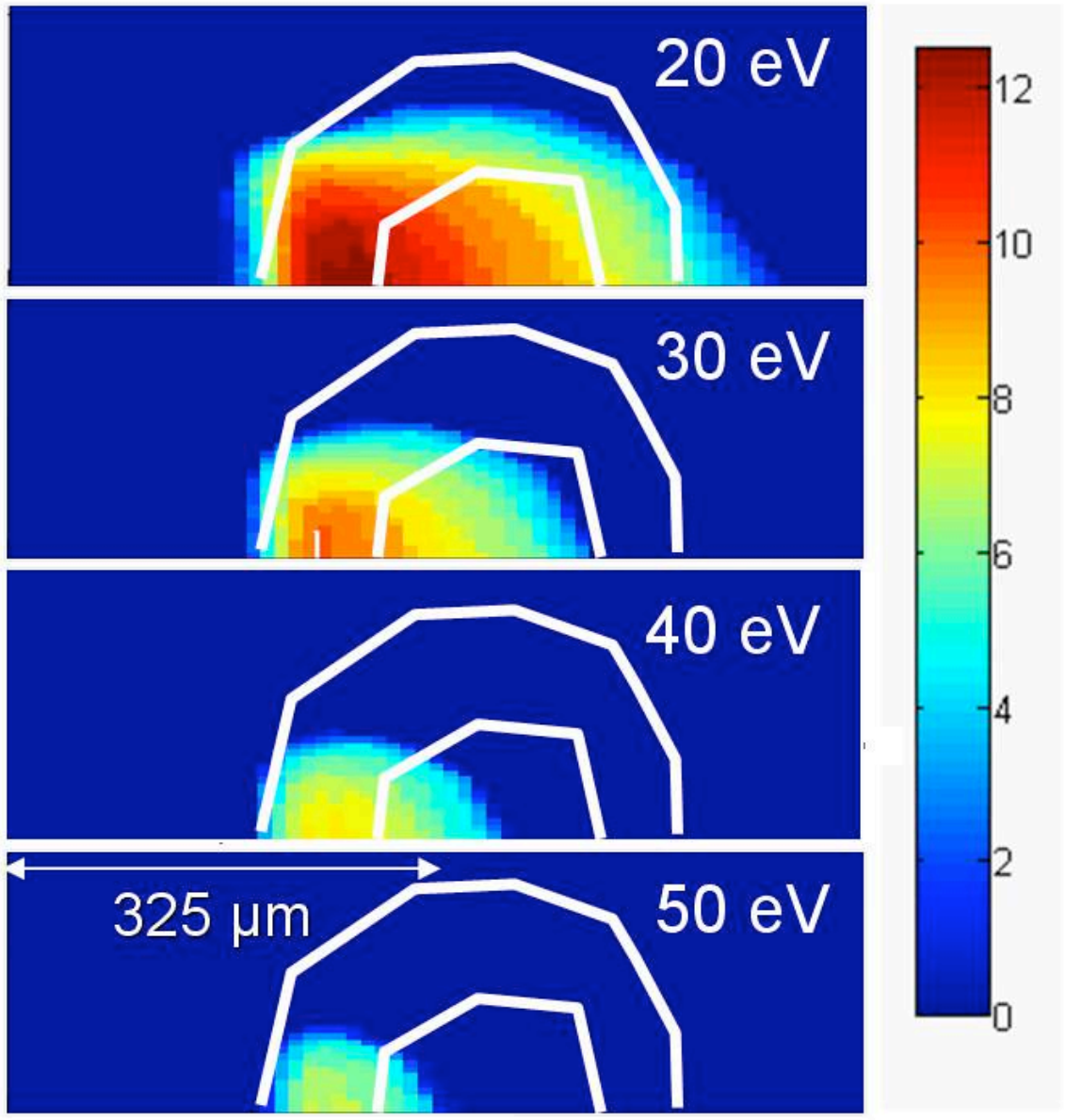

Figure 5.6: Time integrated h2d temperatures with EUV image contours for comparison. The color scale is in ns.

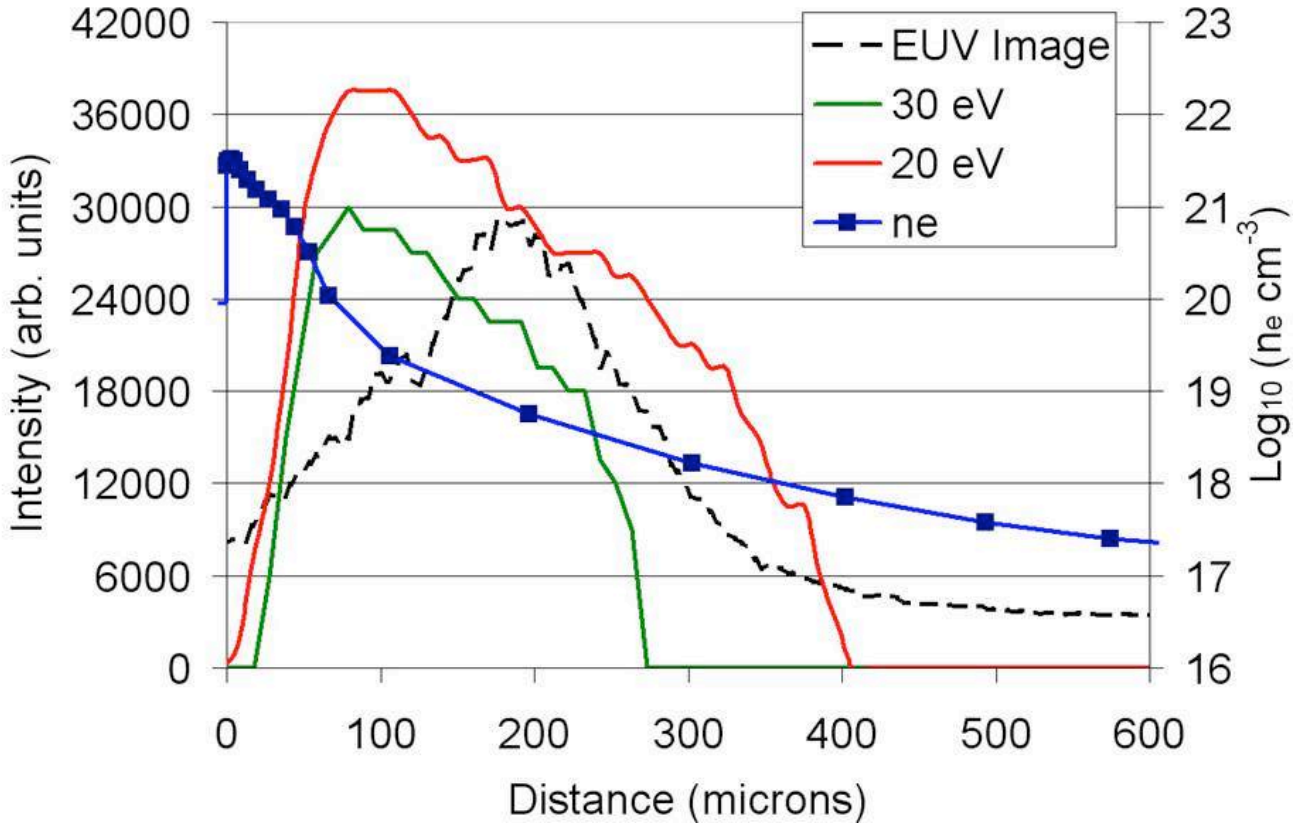

Figure 5.7: Time integrated 30 eV plasma (green) and electron density (blue) from h2d compared to line profile from EUV image (black dash).

6. Simulated EUV spectra

One of the most difficult problems in the study of laser-produced plasmas is accurate modeling of the radiation transport. Because of the step temperature and density gradients present in a LPP, it is important that the physics that govern the radiation transport as well as the atomic levels of the ions are both accurate and detailed. The radiation transport model implemented in h2d is not sufficient for this task. It is lacking in two important aspects. One, the atomic model that determines the energy levels and transitions in h2d is based on a hydrogenic model. These relatively simple models do not capture the most important transitions for EUV emission. It is necessary to use a more detailed atomic model that includes the important transitions. The other aspect that h2d lacks in its radiation transport model is the means to accurately calculate the processes involved in the emission on the detailed level. The radiation is treated with a diffusion model and acts as a heat source or sink based on a gray opacity. To properly treat the radiation emission and absorption the rate equations must be solved along with detailed atomic data.

Here we attempt to reproduce the atomic spectra measured in laser-produced plasma experiments for tin microspheres. The work here has a two fold importance. It serves as a benchmarking case for the atomic physics codes for a complex LPP. Typically these codes are benchmarked with very uniform plasmas created at large laser facilities [101-103]. The gradients present in the plasmas produces for EUVL make it possible to test the codes over a larger range of plasma parameters. In addition to benchmarking the codes with experimental results, the codes also provide valuable

information about the plasma that can not be measured directly in the experiment. If accurate spectra can be produced from the model, then conclusions can be drawn about the radiation transport within the plasma.

As described in chapter 3, the evolution of the temperature and density profiles is calculated by h2d and is imported into Cretin to calculate the emission spectrum. Atomic data produced by the HULLAC code at Lawrence Livermore National Laboratory is employed as the atomic model for Cretin. The atomic data is limited to charge states 6^+ to 14^+. Figure 6.1 shows the dependence of the ionization level on the plasma temperature. Notice that there is an artificial upper and lower limit caused by the limited ionization states in the atomic data. This causes a saturation of the charge state when the temperature is below 15 eV or above 50 eV. The extent of the charge state saturation can be seen in Figure 6.2. The figure shows the average charge state at the peak of the EUV emission. Notice that the core of the plasma reaches an ionization level of around 20 in the h2d simulations, where as it is only 14 using the Cretin model.

The limited atomic data results in a limited range of photon energies produced in the UTA by the model. In Figure 6.3 the emission produced by various temperatures ranging from 5 to 40 eV can be seen. Here the plasma was a 100 μm cube with uniform density of 10^{19} cm^{-3}. First it is clear that there is an absence of significant emission above 15 nm. At the lowest temperature of 5 eV, the emission peaks at 14.64 nm. It is clear that at this temperature the emission should be at a longer wavelength, but is not because of the lower limit on the ionization level available in the atomic data.

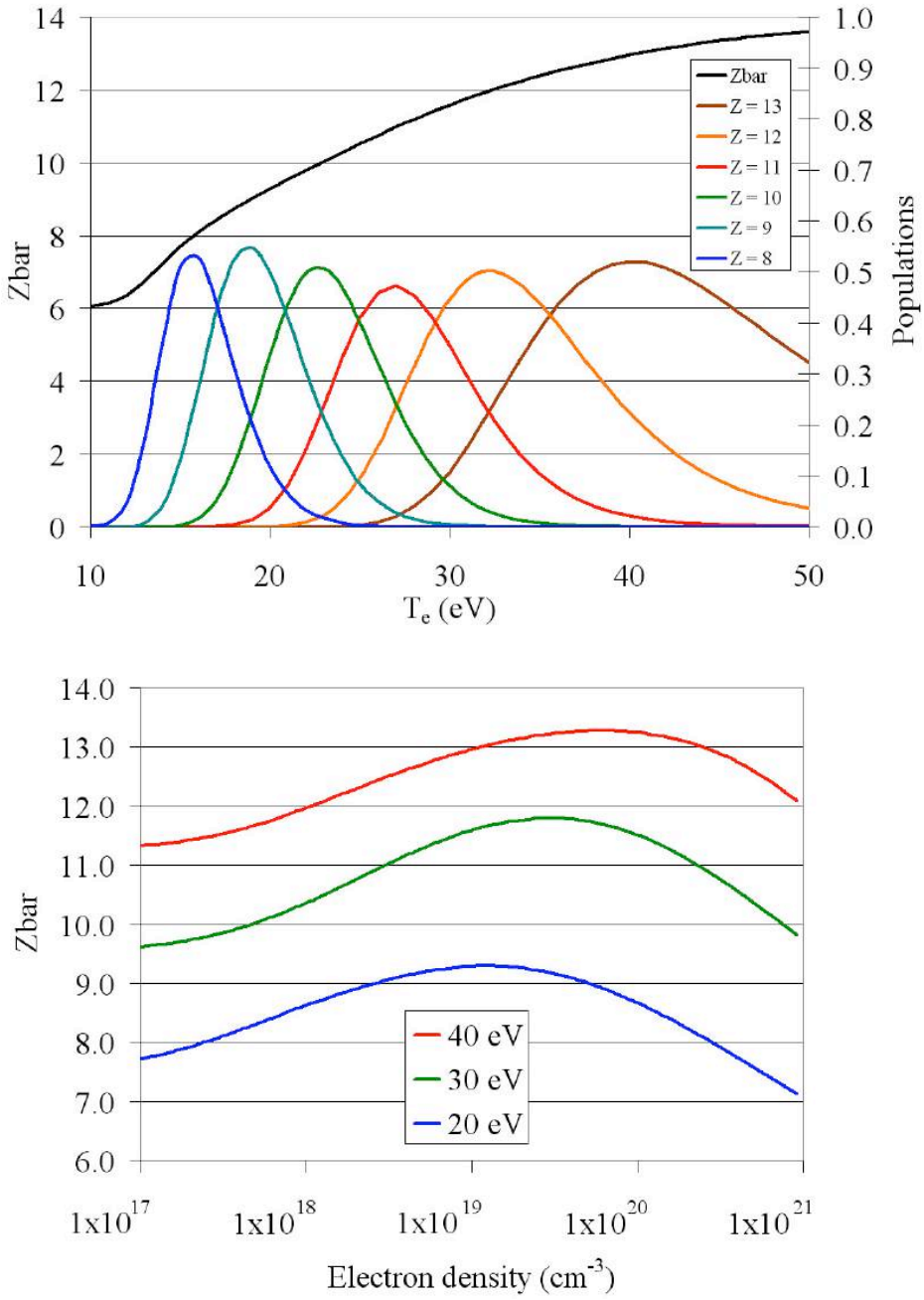

Figure 6.1: Charge populations and $\overline{Z}$, vs. Te with ne = $1x10^{19}$ cm^{-3} (top), and $\overline{Z}$ as a function of density for various temperatures (bottom).

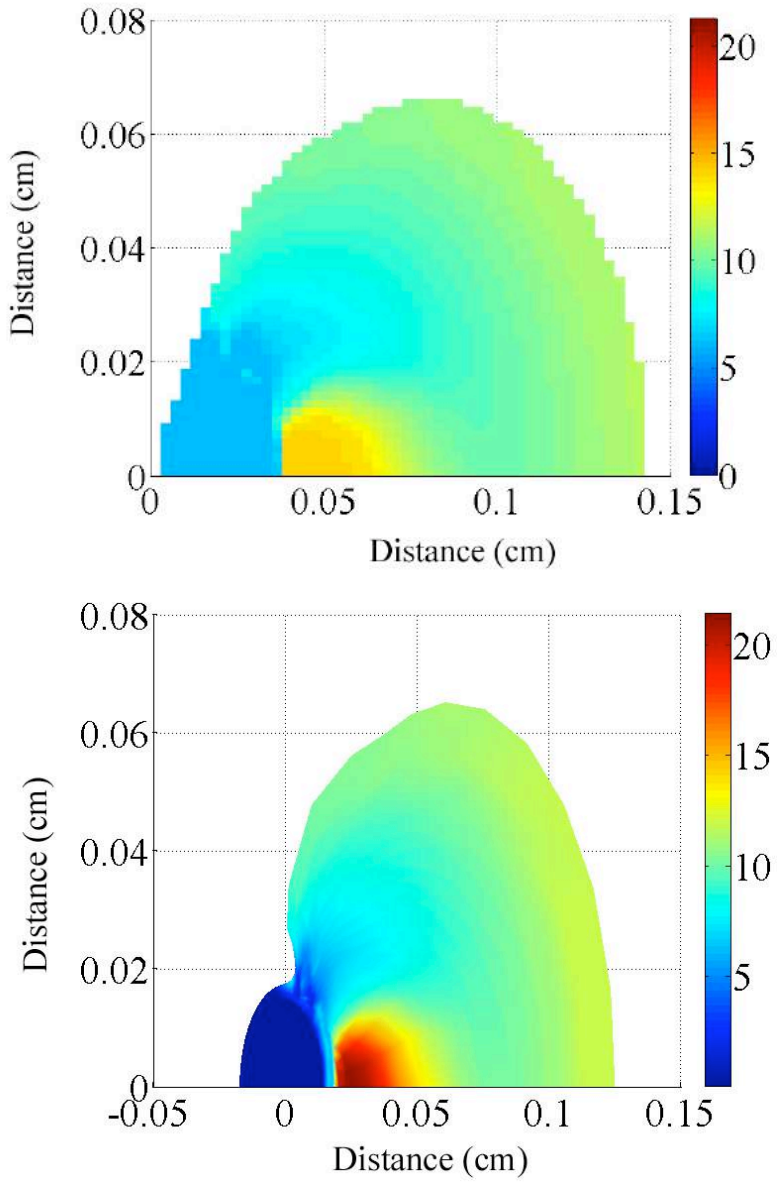

Figure 6.2: Average charge state calculated by Cretin using HULLAC atomic data (top), compared to that calculated by h2d (bottom).

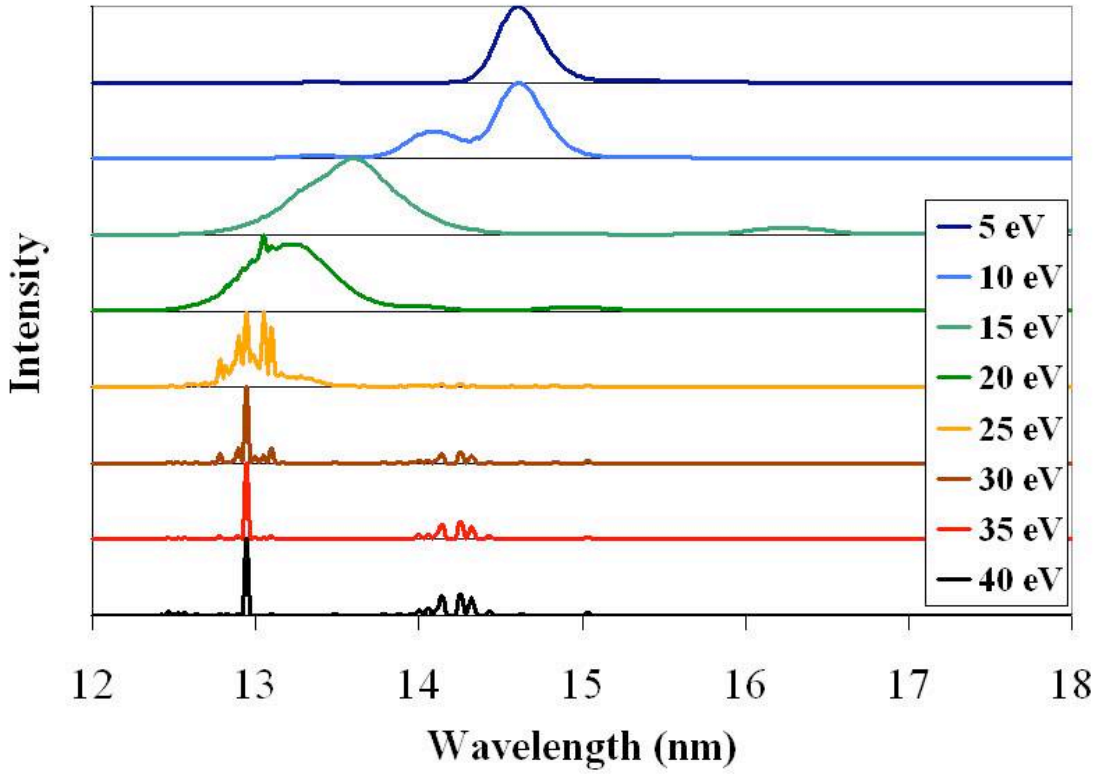

Figure 6.3: Emission spectra produced by uniform plasma at various temperatures.

It can also be seen in Figure 6.3 that the in-band emission is produced within the temperature range of 15 to 25 eV, with the highest intensity produced by 15 eV plasma. Of course the ionization level depends on the electron density, shown in Figure 6.1. Changing the electron density by an order of magnitude has the same effect on the ionization level as changing the temperature by 5 eV. Therefore it is not unreasonable to conclude that the in-band emission is produced in the region of the plasma where the plasma temperature is around 20 eV. This is in agreement with the results in chapter 4.

The simulated EUV spectra from 0° to 75° every 15° can be seen in Figure 6.4, Figure 6.5, and Figure 6.6. They are compared to typical experimental measurements at the same angles. It is not possible to compare the measured and simulated spectra on an absolute scale because the TGS is not an absolutely calibrated instrument. Therefore the spectra at each angle have been normalized to compare the relative intensities. Because of experimental constraints, there are no experimentally measured spectra for spherical targets at 0° or 90°. Measurements from a planar target are included in Figure 6.4 for comparison at 0°. There is, in general, good agreement between the experimental and simulated spectra from 0° to 45°. The main discrepancy is at wavelengths above 15 nm. Recall this is the part of the spectra that can not be obtained due to limited atomic data. If the atomic data extended to lower charge states this part of the spectra might also be in agreement.

Whenever these types of simulations are carried out, one always has to question the accuracy of the atomic transitions calculated to construct the atomic data file. One way to access the validity of the atomic data is to look for specific lines, or in this case features composed of many lines, that are clearly defined in the spectra. There are

several such features that are easily discernable on both the simulated and measured spectra. The clearest appear in the top of Figure 6.5 where the spectra at 30° are shown. For example there are three distinct peaks in the simulated spectra located around 14 nm, followed by a dip that occurs at 14.2 nm, and then there are two more peaks near 14.25 nm. Upon examination of the experimentally measured spectrum, these features can be seen although in less detail, due to instrumental broadening. Another pair of peaks that are present in both the measured and simulated spectra, seen in Figure 6.4 for the 15° spectra, can be identified at 13.43 nm and 13.52 nm. At 45° there is a peak at 14.6 nm that is clearly present in both spectra. The presence of so many identifiable features makes verifying the atomic data possible. These peaks match in both wavelength and intensity, although the intensity is also highly dependent on the plasma conditions, giving a high degree of confidence in the atomic data.

It can be seen from the figures of the spectra at different angles that as the angle increases the sharp peaks around 13 nm and 14 nm in the simulated spectra become more dominant. These peaks arise from charge state 14. As shown in Figure 5.1, there is a steep density gradient in the longitudinal direction, and the density is nearly constant in the emission region along any lateral line, the only change corresponding to the curvature of the target surface. The density profile, along with the charge state saturation, is responsible for the increasing intensity of the peaks. The narrow spectra measured at 60° and 75° indicate that there is less absorption from the plasma surrounding the emitting region and that the emitting region is a more uniform temperature. The emitting region viewed laterally is a dense and uniform temperature plasma surrounded by a much lower density and much cooler absorbing plasma. This amplifies the effects of the charge state

saturation. If the atomic data accessed ionization levels higher than 14, the plasma responsible for the exaggeration of the peaks would be well above charge state 14 and would not contribute to the peaks.

If the exaggeration of the large peaks can be accounted for by the charge state saturation, then there is in general good agreement between the simulated and measured spectra from 13 nm to 15 nm. The general trend is that the agreement is best at 15° and 30° and worsens as the angle increases above 30° or decreases below 15°. In the 30° comparison the model underestimates the absorption dip at 13.7 nm, and at 15° the model overestimates the same dip. Otherwise the spectral shape produced by the simulation at these two angles is almost identical to that measured in the experiments. This is an indication that the 2D radiation hydrodynamic simulations performed with h2d provide an accurate description of the evolution of the plasma properties during the laser pulse. Small deviations in the plasma temperature would have a significant impact on the emission spectra as can be seen in Figure 6.3.

To test the sensitivity of the spectra to the plasma temperature, a Cretin simulation was run with modified electron temperature profiles from h2d. At each time step in the h2d simulation the plasma temperature was increased by 16.7%, by multiplying the temperature at each zone by 1.167. This is the percentage necessary to increase the zones at a temperature of 30 eV to 35 eV. The original and modified simulations were identical except for the artificial increase in the temperature. As might be expected, increasing the plasma temperature has the effect of reducing the longer wavelength, out-of-band emission, as seen in Figure 6.7. In this figure, it can be seen that the emission above 14.3 nm in the modified case is much too low compared to the measured spectrum. The

original temperature profile produces a spectrum consistent with the experiment until the lower limit of the atomic data causes a deviation. The ability of Cretin to replicate the spectrum accurately is an indication that h2d is accurately modeling the plasma conditions. Even a small variation in the plasma temperature can be detected in the spectrum.

In the experiments both the spectrum and integrated in-band emission were measured. It is also easy to convert the simulated spectra into integrated in-band energy detected. The simulated spectra are simply integrated over the in-band range, in the same manner that the TGS data was integrated in chapter 4 for direct comparison to the E-Mon data. Figure 6.8 compares the measured and simulated angular distribution of the in-band energy. The simulation was normalized to the experimental value at 45°. It is obvious that the model does not accurately predict the energy distribution.

The bottom graph in Figure 6.8 contains the distribution produced by a spherical plasma of uniform temperature and density. The computational mesh in h2d at time zero was used to construct a spherical target with an electron temperature of 30 eV and electron density of 5×10^{19} cm^{-3}. The uniform sphere mesh was then imported into Cretin to establish a baseline distribution. If the code is working properly this case should provide a perfectly flat angular distribution. As can be seen from the figure, this is not the case. It is obvious that the dominant factor for the simulated angular distribution seen in the top of Figure 6.8 is this baseline distribution.

This baseline distribution is caused by the finite number of ray angles used in Cretin for radiation transport. If there are a significant number of rays, then each detector will see the same number of rays, and for the uniform case, a uniform distribution will be

produced. However, the number of rays must be limited in order to make the computational time reasonable. This causes an uneven distribution of rays among the detectors. Slight changes in the position of the target or the detectors cause as significant change in the number of rays incident on the detector area. The expansion of the plasma during the laser pulse makes a calibration to account for the baseline difficult, because of this sensitivity to position. The best solution would be to use more rays for the radiation transport. Here this is not a possibility because of the limit on computational power.

Despite not recovering the angular distribution of the in-band EUV emission with the model, the computational work here is not a failure. We have seen that the EUV spectra were reasonably reproduced with the exception of the features caused by charge state saturation. This alone is valuable to understand the radiative properties of the plasma, and to benchmark the atomic data and the radiation hydrodynamic and atomic kinetic calculations.

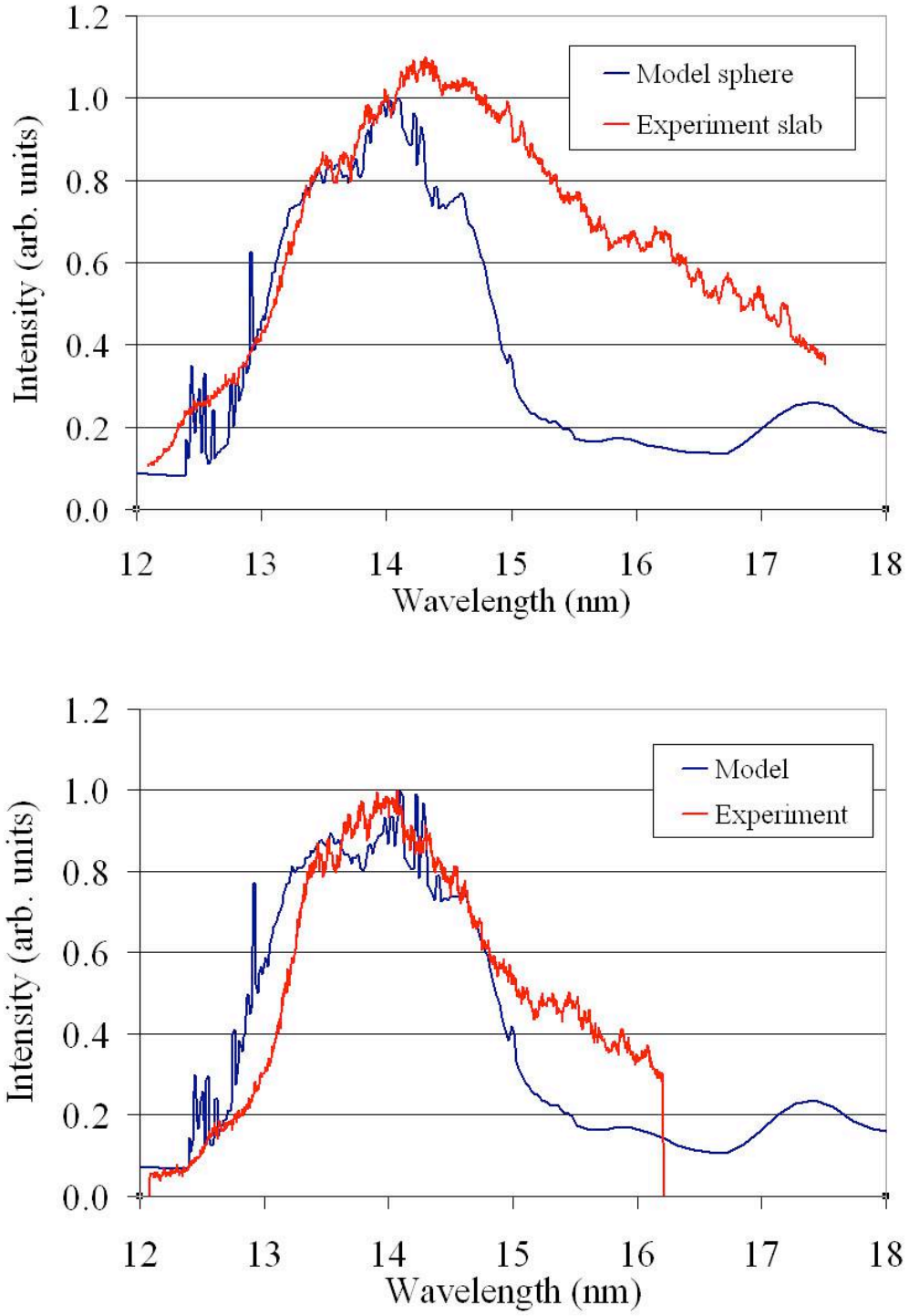

Figure 6.4: Experimentally measured and simulated EUV spectra at 0 degrees (top) and 15 degrees (bottom).

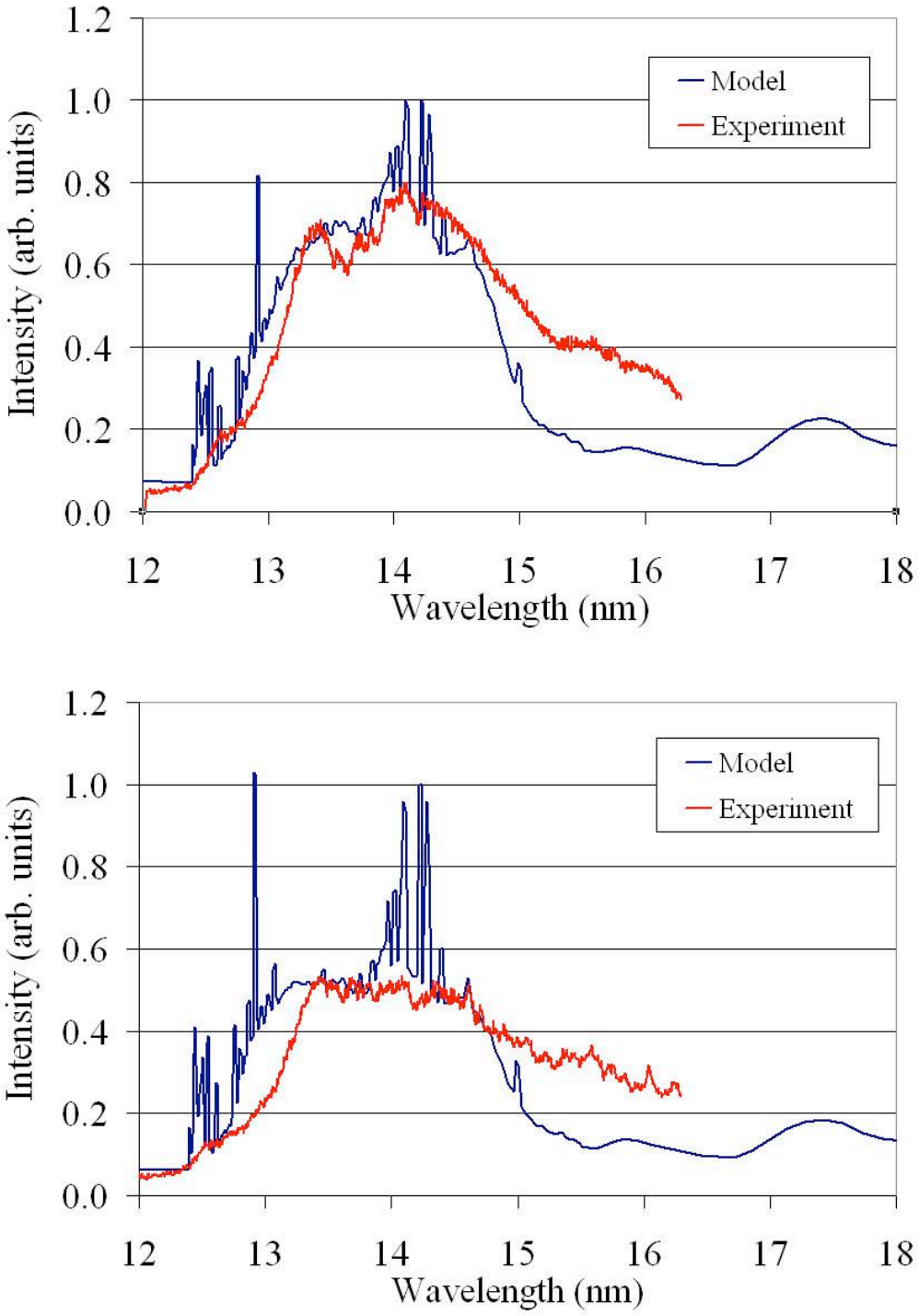

Figure 6.5: Experimentally measured and simulated EUV spectra at 30 degrees (top) and 45 degrees (bottom).

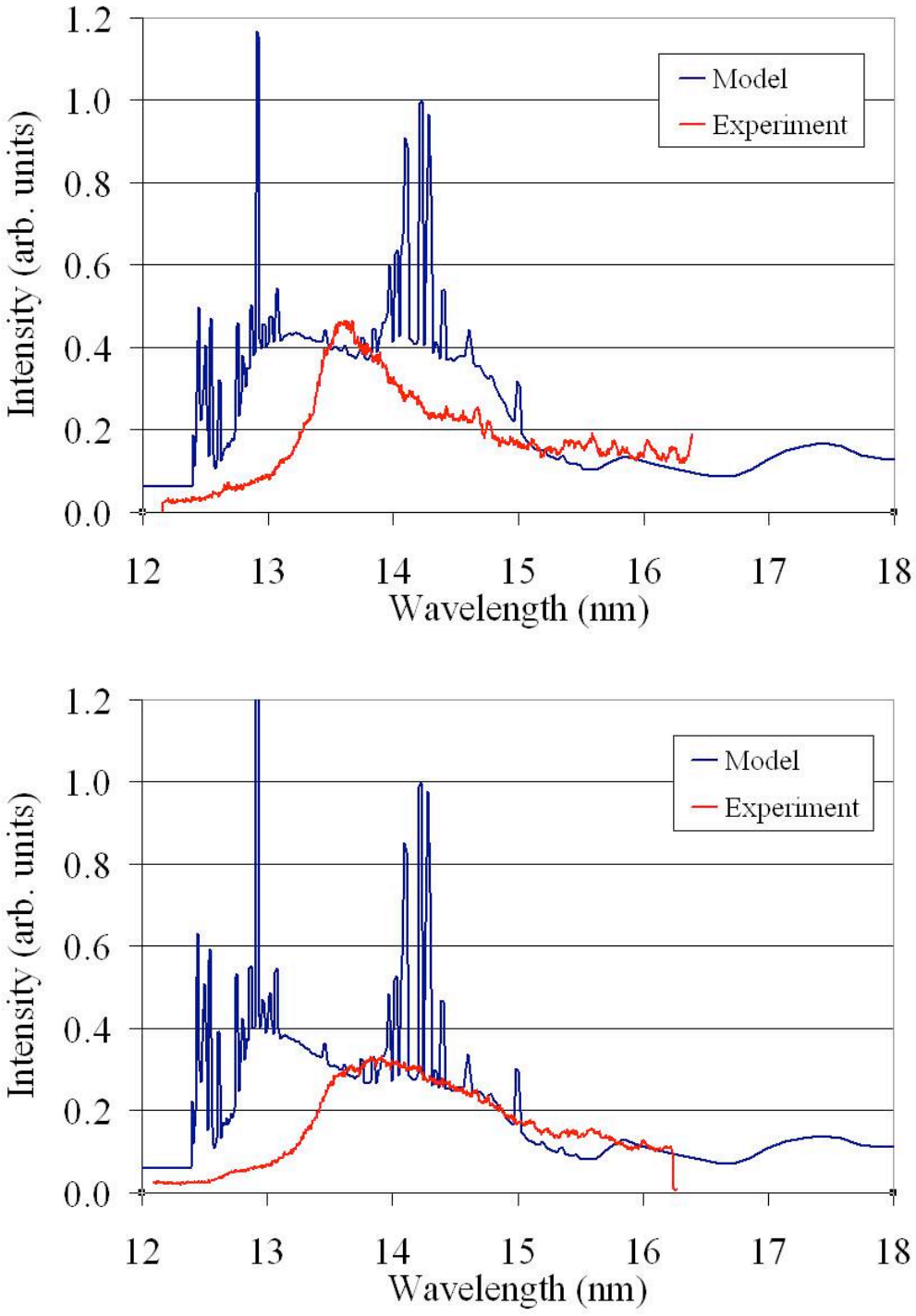

Figure 6.6: Experimentally measured and simulated EUV spectra at 60 degrees (top) and 75 degrees (bottom).

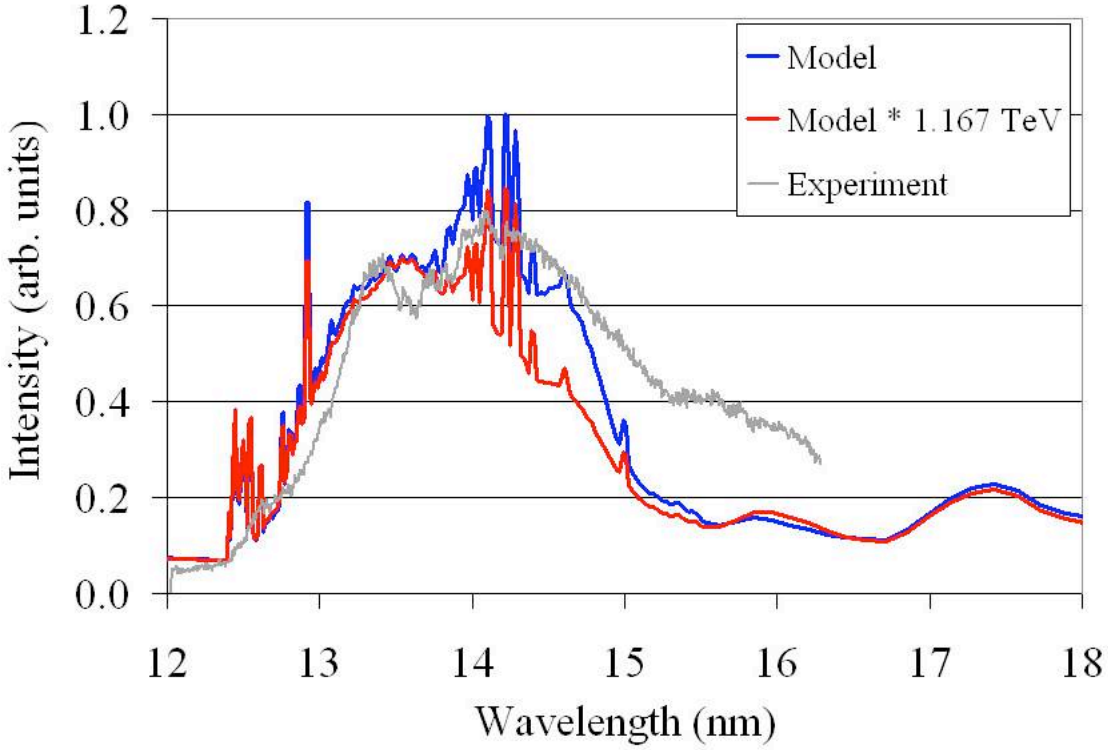

Figure 6.7: Spectral shift, shown in red, caused by a 16.7% increase in the electron temperature calculated by h2d compared to the spectra produced without changing the output from h2d, shown in blue.

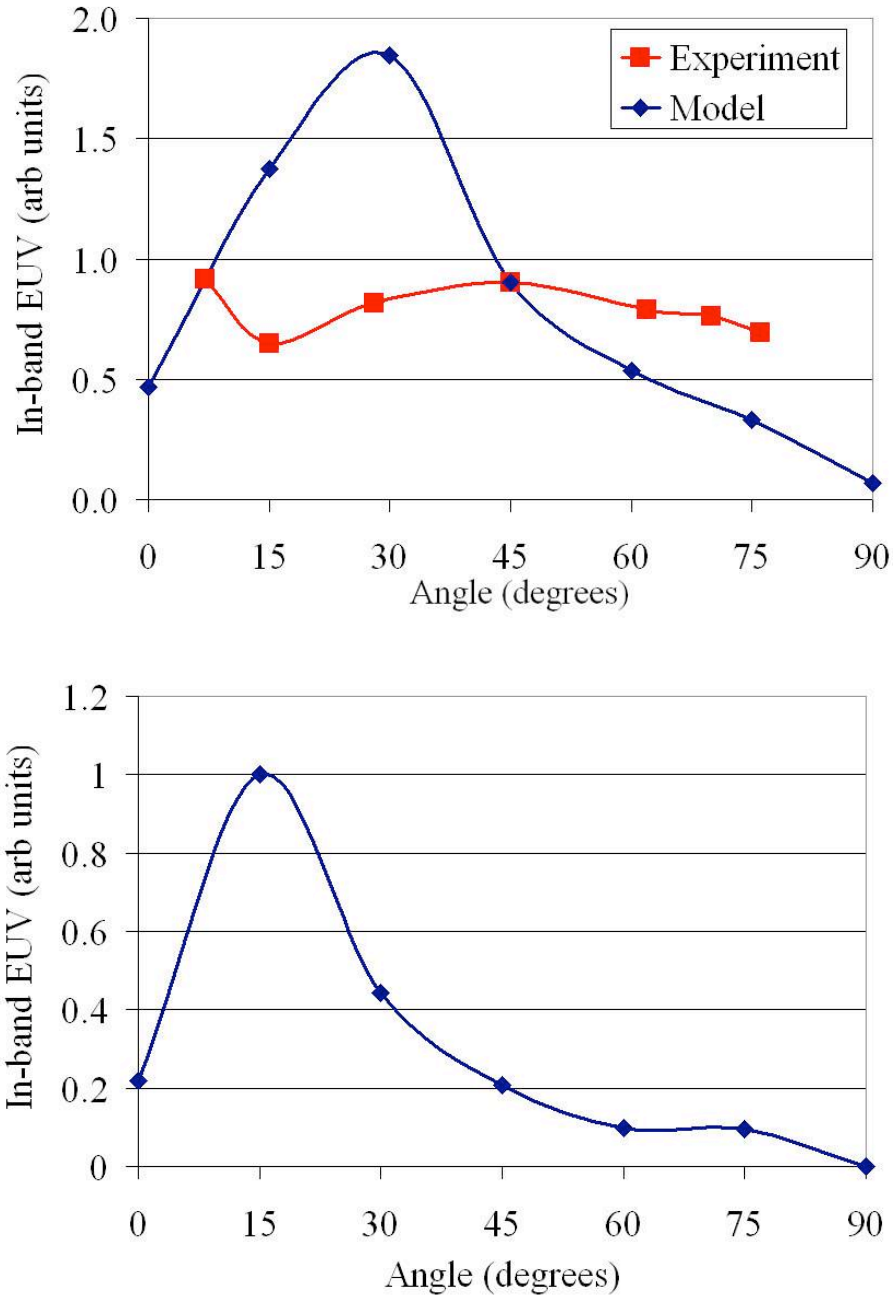

Figure 6.8: Measured and simulated angular distribution of in-band EUV energy (top) and the distribution produced from a uniform sphere (bottom).

7. Laser pulse duration effects

In this chapter the effects of the laser pulse duration on the plasma evolution will be reported. Again, the main objective is to understand how the conditions in the plasma effect the EUV emission and absorption. The laser pulse duration affects the plasma conditions in several ways. Perhaps the most obvious is that the plasma scale length increases proportionally with the laser pulse duration, as seen in Equation (1.6). Manipulating the plasma scale length affects the EUV production by controlling where the laser absorption occurs and influencing the amount of EUV emission and absorption. Careful selection of the laser temporal pulse makes it possible to pump the plasma when conditions are appropriate for EUV production.

7.1. Experimental description

The data presented here were collected using a 1.064 μm pump laser with pulse durations ranging from 0.5 ns to 16 ns. The pulse duration was varied, as described in chapter 2, by implementing two different lasers with pulse durations of 0.5 and 7 ns. These pulse durations could then be lengthened by means of a delay system to produce pulses of 1 and 16 ns respectively.

A schematic of the optical delay system can be seen in Figure 7.1. The laser enters the optical delay system by passing through a ½ waveplate. Because the laser is Q-switched, the waveplate in combination with a polarizing cube beam splitter can be used to adjust the total laser energy entering the system. Another waveplate immediately follows the cube polarizer to again rotate the polarization of the beam. This time

however, the cube polarizer that follows acts to send a portion of the beam directly to the final focusing lens and into the chamber, and the other portion of the beam is sent through a delay line. The beam energy sent directly to the chamber is less than that sent through the delay line to account for losses along the delayed path. The laser energy is balanced by monitoring the temporal pulse shape as seen in Figure 7.2. The delay line consists of three mirrors spaced so that the total path length is around 240 cm, giving a 8 ns delay for long pulse durations, or around 15 cm for a delay of 0.5 ns when a short pulse is required. When the delay path is long, the laser divergence must be accounted for by the addition of a telescope. The telescope is adjusted so that the laser focal spot size is the same for the short and long path to the chamber. The two spots are aligned via focal spot imaging to within a few microns.

Adjusting the delay line spacing varies the pulse duration of the 7 ns pulse to give 13 or 16 ns. Pulse durations from 1 ns to 7 ns could not be obtained in this experiment, data from Ando et al. [49] is included to cover this range for comparison. However, it should be noted that the laser focal spots size in Ando et al. was significantly larger, 500 μm, than that of this work, less than 300 μm.

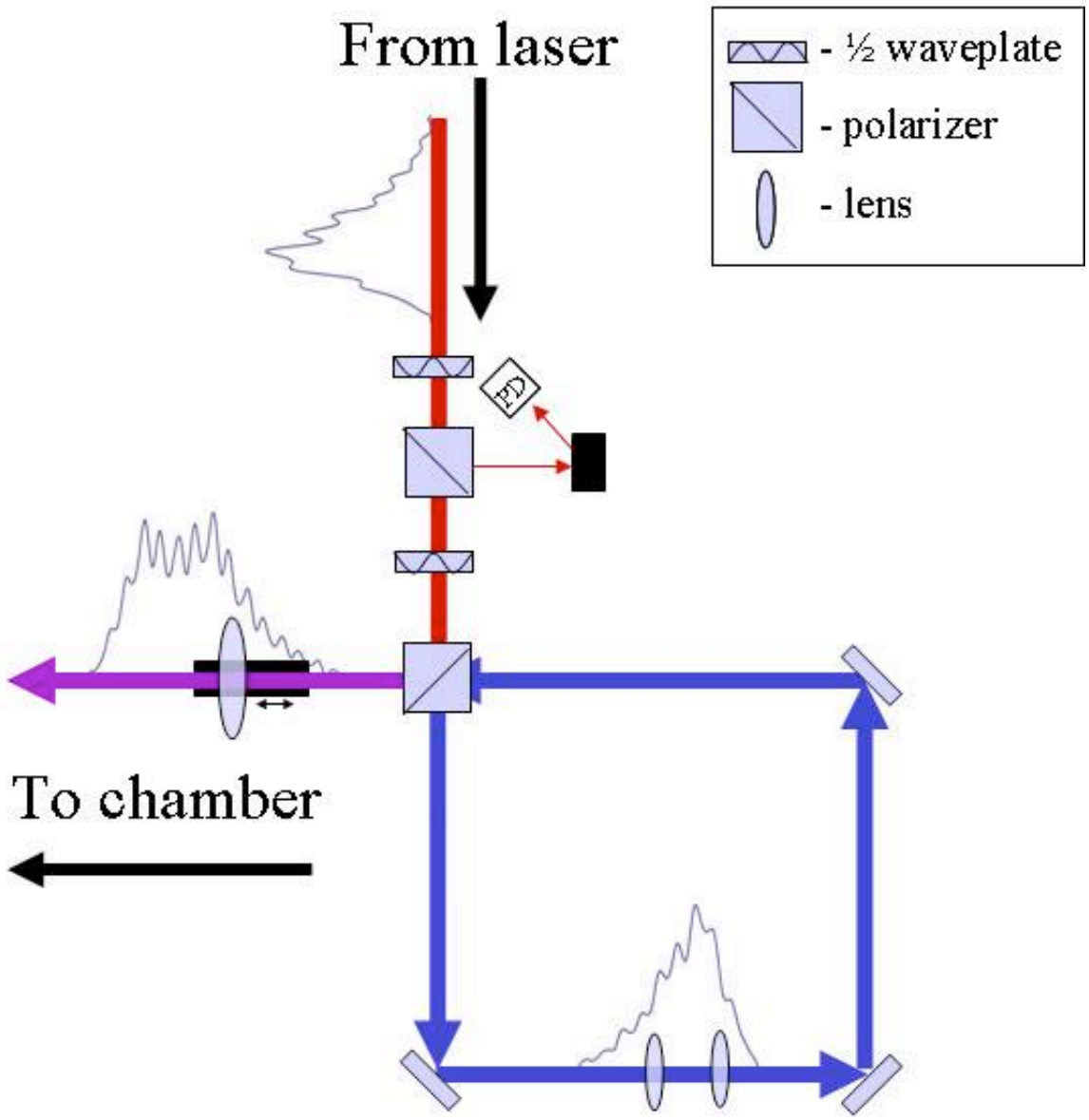

Figure 7.1: Schematic of the laser delay system for producing extended pulse durations.

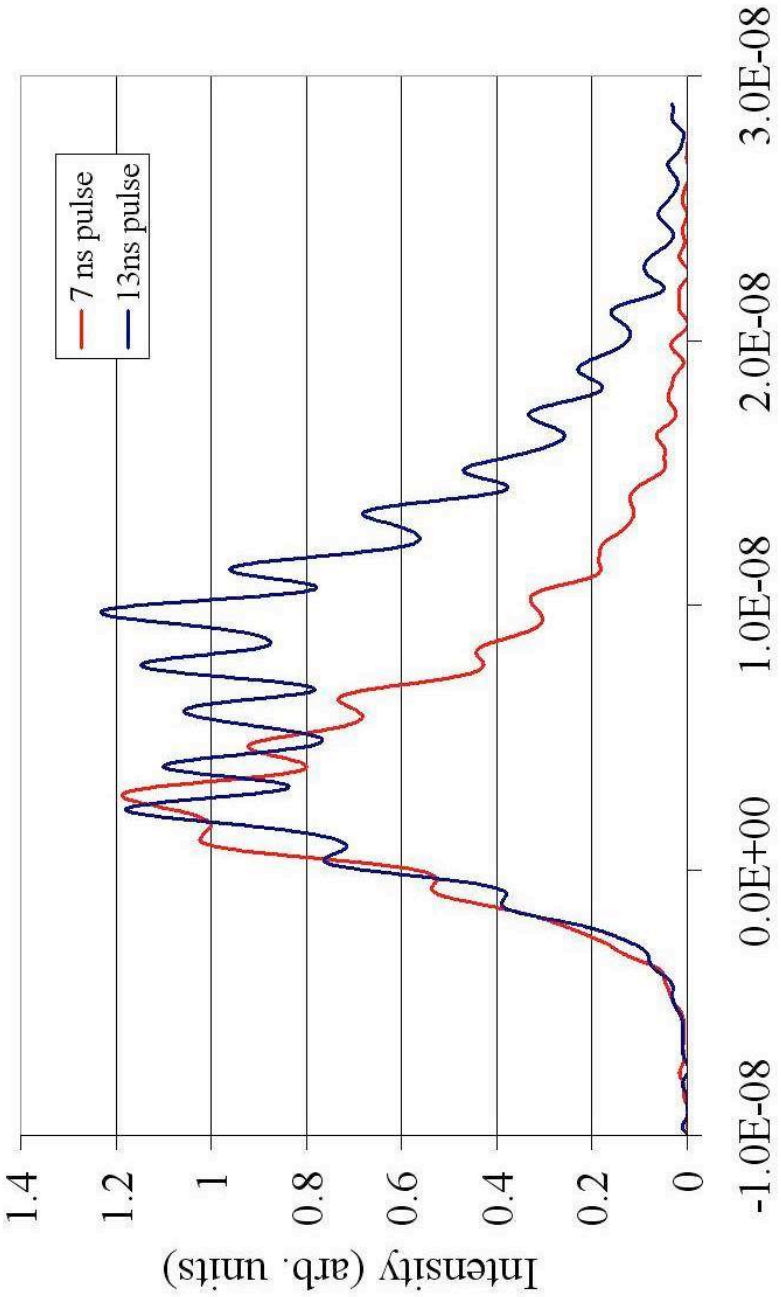

Figure 7.2: Typical laser pulse shape for 7 and 13 ns durations.

7.2. Conversion efficiency dependence on intensity

When the laser pulse duration is changed, the intensity, energy, and/or focal spot size must also change. However, the most important factor for efficient EUV production is the laser intensity. In Figure 7.3 the in-band CE is reported for various laser intensities when the pulse duration was 0.5, 1, 7, and 16 ns. The data for the 0.5 ns pulse duration had a fixed spot size of 300 μm, and a focal spot size of 250 μm or 160 μm was implemented for the 1 ns pulse durations. The laser energy was also adjusted to vary the intensity. These spot sizes are around twice that used for laser pulses of 7 ns and above. The in-band CE is measured by integrating the E-Mon signal and dividing it by the laser energy. When the pulse duration is short the spot size must be large or the energy low to access the same intensity. When the laser energy is too low the E-Mon signal to noise ratio becomes too small, and the percentage error in the shot to shot laser energy increases, making the in-band CE measurement contain more error. For the 7 to 16 ns pulse durations, data were collected by both fixing the laser energy and varying the focal spot and fixing the spot size and changing the energy. The spot size range was from 75 to 230 μm. There is a weak dependence on in-band CE when the focal spot is within this range [104]. In Figure 7.3 all data collected at a given intensity are included whether they were with fixed energy or spot size.

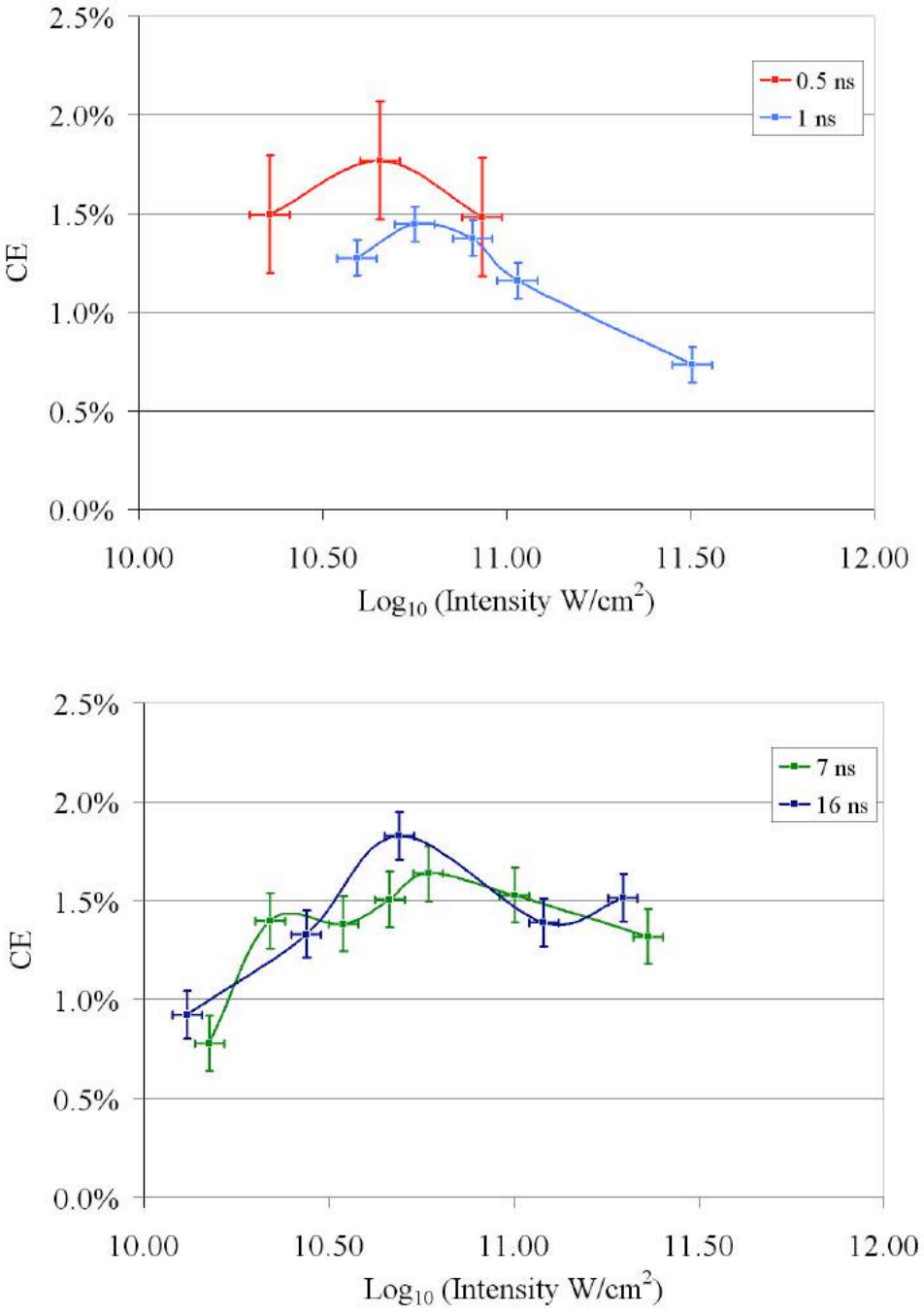

Figure 7.3: Dependence of in-band CE on laser intensity for 0.5, 1, 7, and 16 ns.

As described previously the very short pulse duration of 0.5 ns leads to large error in the CE measurement. This is evident in Figure 7.3 where the error bars for the 0.5 ns pulse are much larger than those of the other pulse durations. In the collection of the 1 ns data, twice the laser energy could be applied to maintain the same laser intensity, and this was enough to all but eliminate errors due to a low signal to noise ratio. Additionally the laser energy is more accurately known once the energy is above 60 mJ because of the lower detection limit on the laser energy monitor.

From the figure, especially for the longer pulses, it can be seen that the rising edge of the CE is steeper than the falling edge. When the laser intensity increases the plasma temperature will also increase. From Sasaki et al. [105] we can see that there is a sharp increase in in-band emission as the temperature increases above 20 eV, and as the plasma continues to increase beyond the optimal temperature, 30 eV, the in-band emission decays rather slowly, reaching sub 20 eV levels only after going above 70 eV. The sharp onset of efficient in-band emission can be attributed to the minimum temperature needed to obtain charge states that contribute to the emission, around charge state Sn^{7+}. Further heating of the plasma only increases the charge state to the optimum around Sn^{10+}, and even more heating slowly shifts the plasma to higher charge states away from the optimum, but which still emit in the in-band region.

7.3. Conversion efficiency's dependence on pulse duration

It is evident in Figure 7.3 that the ideal intensity is around $5x10^{10}$ W/cm^2 regardless of the pulse duration. It is near this intensity that the data in

were acquired. Here the maximum CE for each pulse duration is presented. It is clear that the very short pulse durations do not provide optimal conditions for efficient EUV emission. When the pulse duration is very short, the density in the emitting region is above the optimum of around 10^{19} cm^{-3} resulting in a low CE. The laser is absorbed near the critical density, and the plasma is heated to around 70 eV. At such a high density this temperature far exceeds the optimum for in-band emission. Deeper within the plasma the temperature is cooler and near optimal levels. However, the density is much too high causing the in-band photons emitted from this region to be totally absorbed, hence low CE.

As the pulse duration increases the plasma scale length increases so that the density in the emitting region is more suitable for efficient EUV emission. Additionally the surrounding plasma is still short enough that the absorption of the EUV is minimized. This is the mechanism responsible for the rapid rise of the CE up to 2 ns pulse durations. As the pulse duration grows beyond 2 ns the dominant EUV emission region is surrounded by cool dense plasma, which acts as an absorption region and we see a drop in the CE [49].

Eventually, as the pulse duration continues to increase, the laser absorption begins to spread out over a longer path due to the ever increasing plasma scale length. This acts to reduce the peak plasma temperature and increase the amount of plasma in the optimum temperature range. For several ns the play between emission and absorption is balanced, and there is very little change in the CE as the pulse duration increases. Once the plasma scale length has reached a critical value the CE once again increases, because the laser heating is occurring at a lower density where the efficient temperature range is much

broader as can be seen in Figure 7.5. This figure shows the dependence of the in-band emission on the plasma temperature at various electron densities. It is clear that lower electron densities emit efficiently over a larger temperature range.

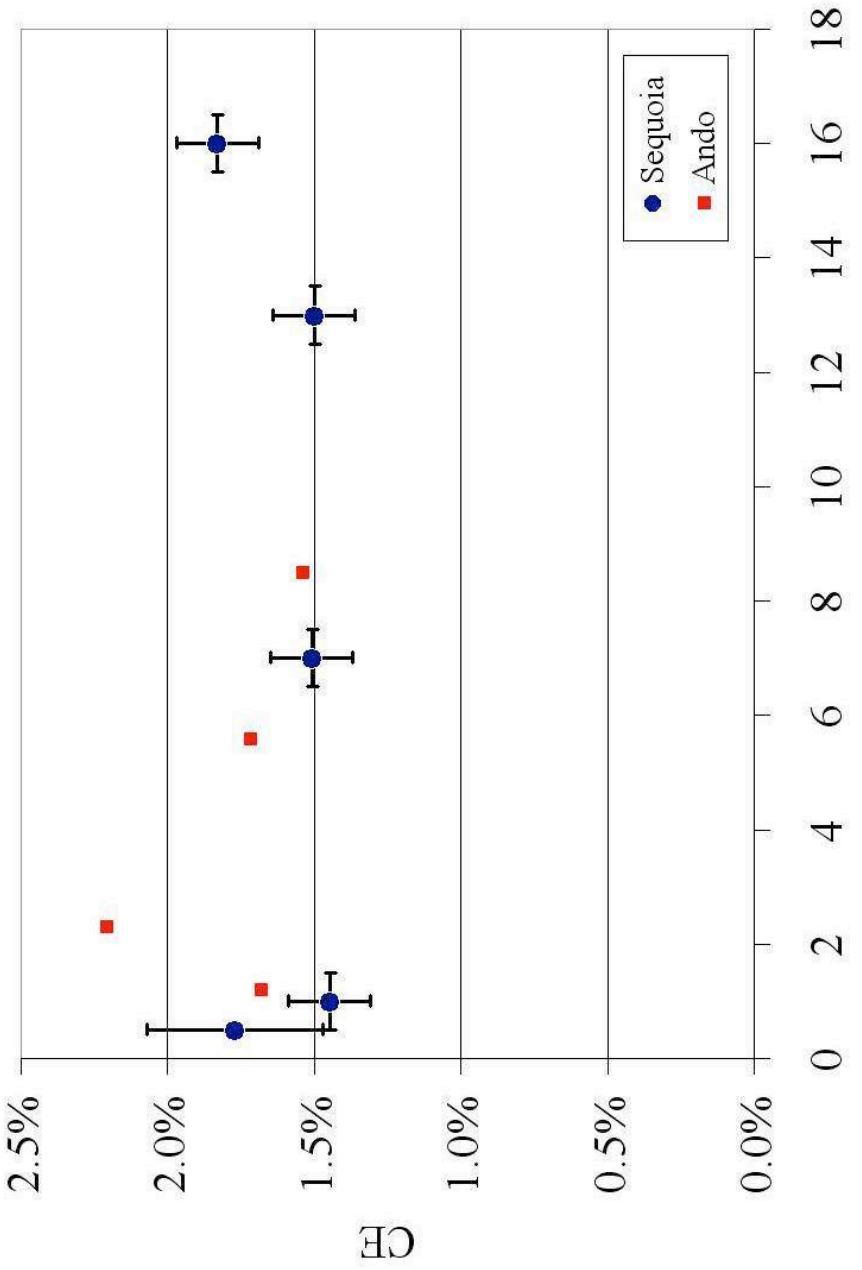

Figure 7.4: Maximum CE obtained with various pulse durations. Red squares are data from Ando et al. [49] and blue circles are data collected for this work.

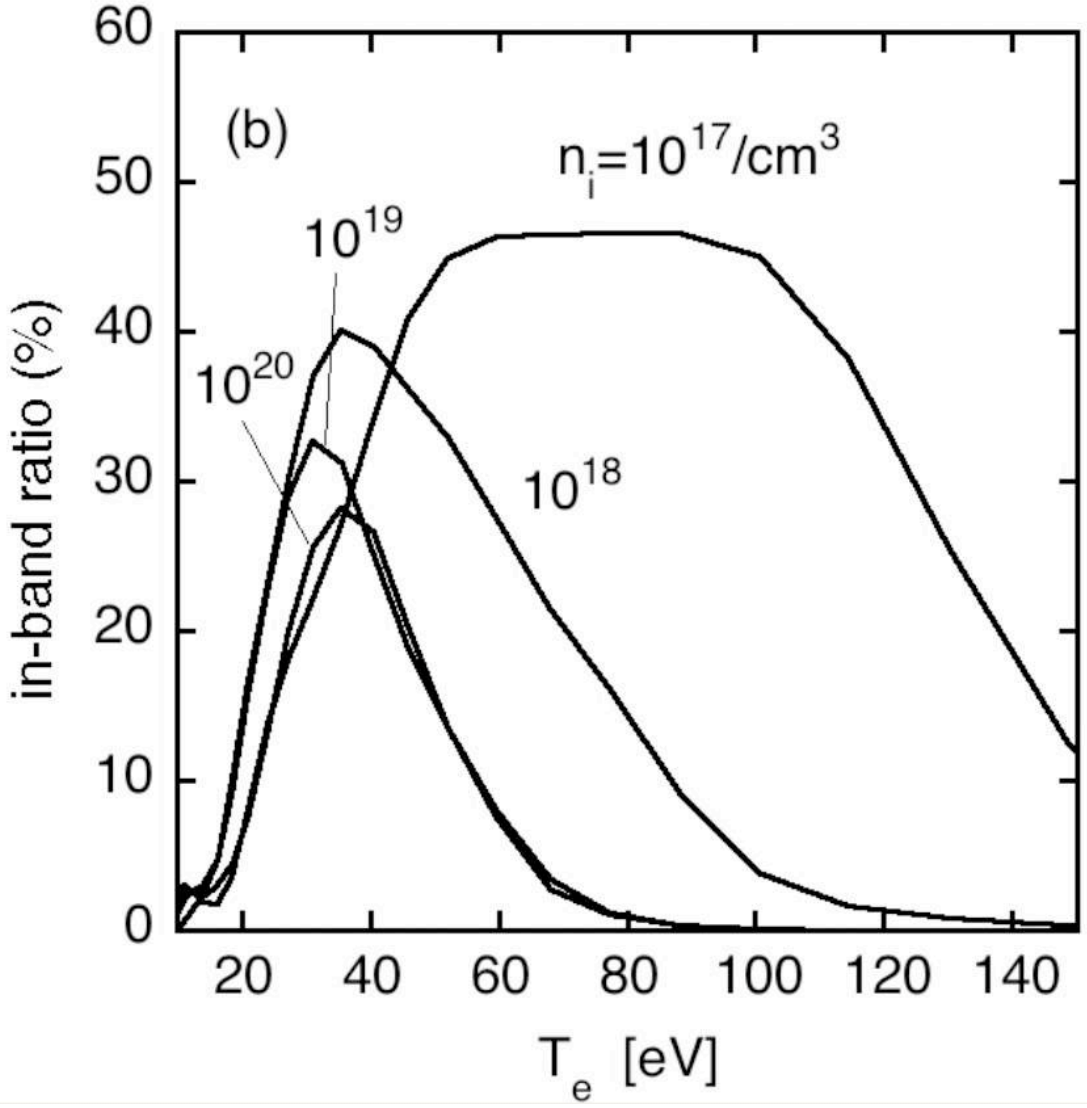

Figure 7.5: Spectral efficiency of the plasma calculated by Sasaki et al. from [105]

7.4. Pulse duration effects on EUV spectra

The EUV spectra, in Figure 7.6, provide evidence for the explanations above. The spectra are normalized to one another at 13.5 nm for comparison. First the 0.5 ns laser pulse yields an EUV spectrum typical of a plasma that is strongly absorbing the in-band emission. There is a clear dip in the spectrum from 13.3 to 14.3 nm. This is the same dip seen in chapter 4, and it is caused by the resonant lines in Sn^{9+} to Sn^{13+} [65]. This effect is only seen with the optical depth, given by

$$\tau_\nu = \int_0^x \mu_\nu dx, \tag{7.1}$$

where μ_ν is the total absorption coefficient at frequency ν, is significant. The absorption coefficient is related to the radiation mean free path by,

$$l_\nu = \frac{1}{\mu_\nu}. \tag{7.2}$$

We know that the plasma scale length is relatively short for such a short laser pulse. Hence the path length, x, is small. For there to be significant absorption the absorption coefficient must be relatively large. From Equation (7.2) it is clear that as the density of the plasma increases μ_ν increases proportionally, therefore where the plasma is dense more absorption takes place. The overall shape of the 0.5 ns spectrum is similar to that of the longer pulse durations with the exception of the dip.

Comparing the 7 ns pulse spectrum to that of the 16 ns pulse, it is clear that the latter is narrower. The features in each case are similar, but the longer wavelengths are at

a higher intensity for the 7 ns pulse. Just from the spectra one could argue that the EUV emission region has similar plasma conditions, with the only difference being that the density is higher for the 7 ns pulse. It is known that as the density of the plasma increases inner-shell and multiply excited configurations become more populated. As a result more emission is produced in the satellite lines from the 4d-4f, 4p-4d, and 4d-5p transitions [65]. Hence, the spectrum will be broader when the density is higher.

The emission and absorption as calculated by Sasaki et al. [65] can be seen in Figure 7.7. Both optically thick and optically thin emission spectra are present making the observed spectra for the various pulse durations more clear. When the plasma is very optically thick, as in the short pulse case, the emission spectrum shows a very strong dip near the in-band portion. As the plasma becomes more optically thin to the EUV, the spectral dip diminishes, as is the case when the pulse duration is extended.

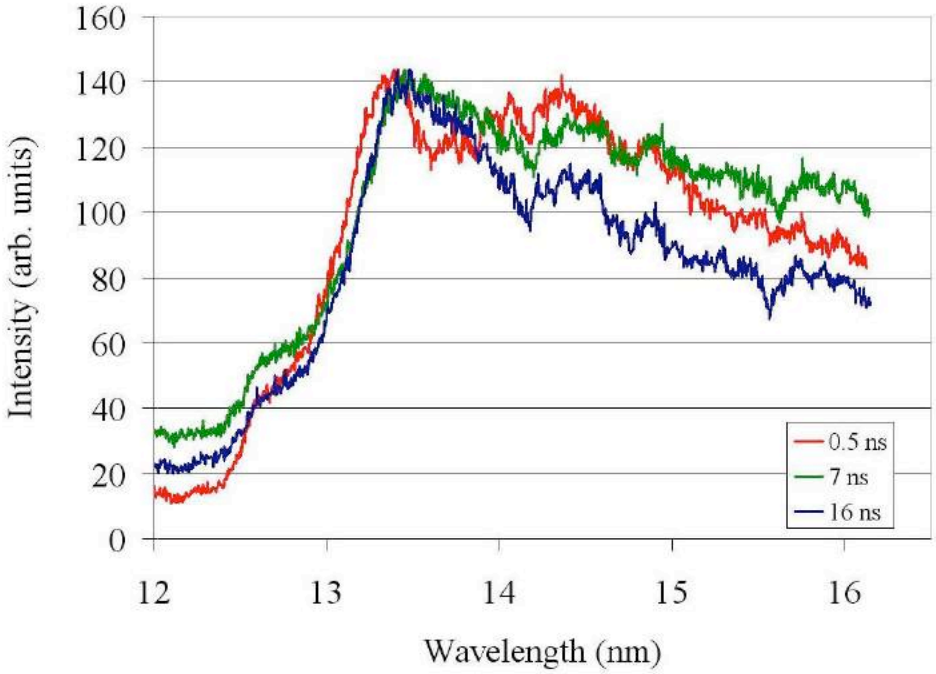

Figure 7.6: Typical spectra for 0.5 (red), 7 (green), and 16 (blue) ns pulse durations.

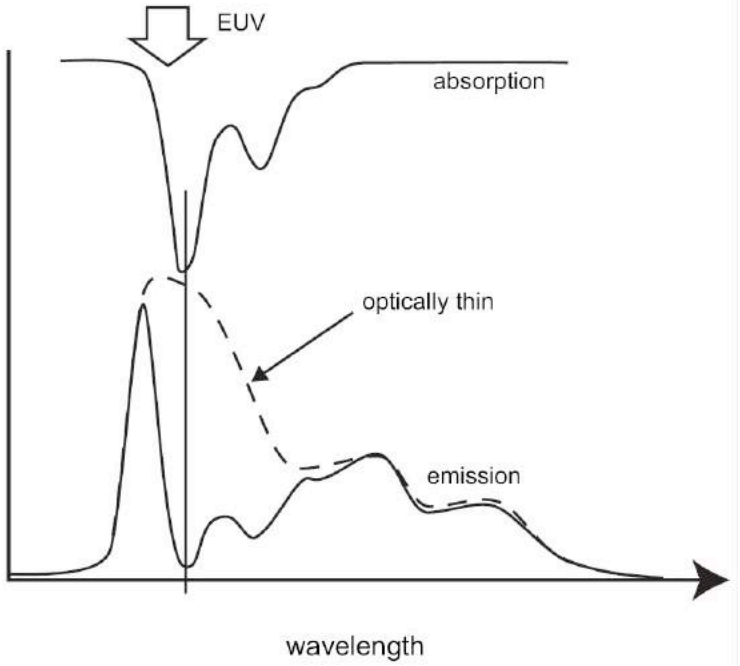

Figure 7.7: Schematic of EUV emission and absorption adapted from Sasaki et al. [65].

7.5. Pulse duration effects on EUV plasma density

Finally we look to the plasma density profiles which show the increase in scale length with pulse duration. In Figure 7.8, the line profiles along the laser axis can be seen. The densities for a 0.5, 7, and 15 ns pulse are presented. The top of the figure shows the log base 10 of the electron density for ease of reading. While the lower figure has the natural log of the electron density so that the plasma scale lengths can be calculated. To acquire the profile for the 0.5 ns pulse the Surelite laser was used in combination with a CCD camera with a 2 ns gated MCP. This does not allow for an accurate measurement of the peak density as the image is exposed for much longer than the laser pulse.

Despite this, a reasonable plasma scale length of 72 μm can be calculated for the short pulse. From this scale length the average charge state and the electron temperature can be calculated, as in chapter 4, to be 14 and 60 eV respectively. The 7 and 15 ns pulses have plasma scale lengths of 192 μm and 322 μm respectively. Again the average charge state and electron temperatures can be calculated to be 14 and 60 eV for the 7 ns pulse and 13 and 40 eV for the 16 ns pulse.

It is immediately clear that the shorter pulse durations cause a steeper density gradient, which causes the laser absorption to occur very locally near the critical density. At first it may seem advantageous to create a short scale length plasma in order to reduce absorption of the in-band light. However, the density is so high where the laser is absorbed the in-band light can not escape. By increasing the scale length, the laser absorption occurs over a larger volume. This has a two fold effect: one the peak

temperature is reduced to a more suitable level for efficient in-band production, two the surrounding plasma temperature is higher, reducing the absorption of in-band light as it passes through the plasma.

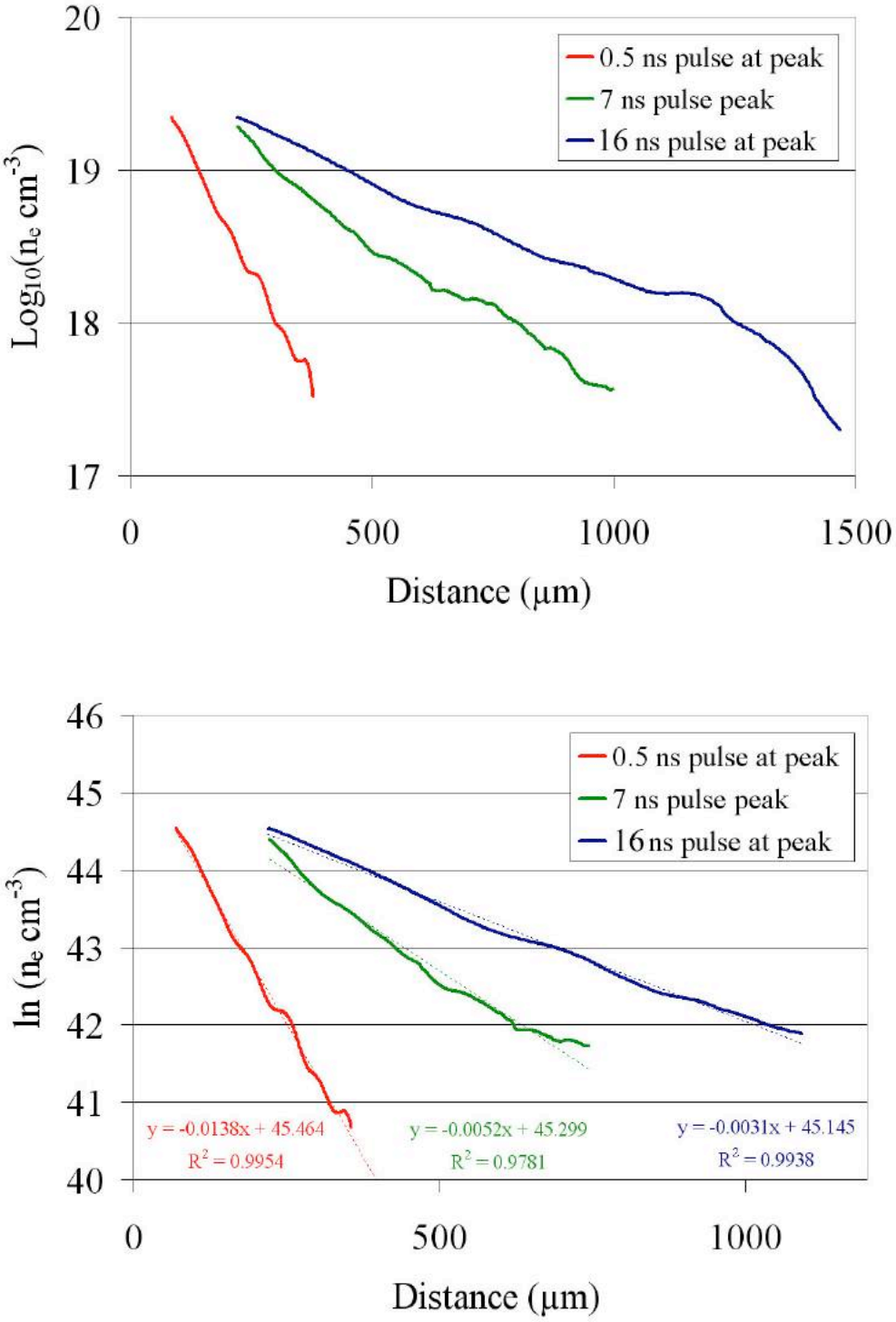

Figure 7.8: Electron density profiles along the laser axis for 0.5, 7, and 16 ns pulse durations.

8. Conclusions and possible future directions

In this work laser-produced Sn plasmas were investigated as an efficient source of EUV emission. Plasma diagnostics such as an in-band EUV energy monitor, TGS, EUV imaging system, Nomarski interferometer, and fast photo diodes were implemented in an experimental campaign to investigate the production and transport of 13.5 nm EUV radiation. Two-dimensional radiation hydrodynamic simulations coupled with a collisional-radiative atomic physics code were used to gain a better understanding of the underlying physics involved in the production and transfer of in-band radiation. The results of these experiments and simulations can be found in chapters 4 – 7.

In chapter 4 the results of the experimental campaign to explore the difference in the EUV emission between planar and spherical targets was presented. It was seen that the plasma expansion plays an important role in the absorption of in-band EUV emission. It is likely that similar levels of in-band EUV energy are generated along the laser axis, where the temperature and density are conducive to the appropriate atomic transitions. The difference, as is demonstrated by the angular distributions of the two target geometries, is in the surrounding plasma that absorbs the emission from the plasma core.

For planar target geometries a simple model was developed to demonstrate the two-dimensional nature of the emission and absorption of the EUV light. The simplified plasma geometry by assuming the emission originates from the core the plasma uniformly, and that the absorption takes place in the outer regions of the plasma where the absorption coefficient depends on the location. The magnitude of the emission is dependent upon the angle and size of the plasma. The absorption is determined by a

pathway through the absorption region and absorption coefficient of that region. The model was able to re-create the measured angular distribution of the in-band EUV emission. The model was also able to accurately predict the dimensions of the emission region, as confirmed by the EUV image. Additionally the absorption region thicknesses predicted by the model were confirmed by the two-dimensional electron density profile.

The simple model has obvious shortcomings such as assuming uniform emission from the core plasma alone, using a single absorption coefficient in each region, and assuming the plasma regions are rectangular blocks. The use of a single absorption coefficient in each absorption region is probably the most problematic assumption. As we saw, the temperature and density gradients lead to rapidly changing opacities along the laser axis, which lead to errors associated with the emission from the front surface and the longitudinal absorption.

It was seen that when the spherical target geometry was employed, the angular distribution matched that of the planar target from 30° to 90°. Between 7° and 30° the spiritual targets producer large dip the angular distribution. This dip is thought to be caused by ions produced near the laser axis expanding laterally outward and cooling to produce a more absorbent region of the plasma. This process not only reduces the total in-band emission by increasing the opacity of the plasma in a small region. It also allows for increased lateral transport of energy away from the dominant emission region located within the laser spot.

This work only measured the angular distribution of the in-band EUV emission for a particular geometry with specific laser parameters. It is expected that different laser spot sizes, intensities, and pulse shapes, as well as, sizes of spherical targets would yield

different angular distributions of in-band light. This is of great importance since the total in-band CE over 2π is one of the key issues for a commercial EUVL source. Much more work is needed to fully characterize the effects of laser parameters in combination with target geometries on EUV emission. It should also be noted that in order to accurately measure the total in-band CE, the angular distribution of the light must be properly measured under the exact conditions as the CE measurement.

In chapter 5 the results of two-dimensional radiation hydrodynamic simulations were presented for the spherical geometry target. An attempt was made to perform simulations for planar geometries, but bowties in the computational mesh prevented the successful completion of the simulations. We were able to construct planar computational meshes that did not bowtie, however the zone spacing was so course that the simulation offered little insight into the relevant physical processes. It may be possible to carefully design the mesh in a way that avoids bowties at the edge of the laser without sacrificing the mesh resolution to such an extent as to make the simulation useless. Attempts to do this had varying levels of success. In the future h2d may be updated and improved to the point where this will no longer be an issue.

On the other hand, h2d was able to run the spherical geometry to completion without any bowties. It was seen that the electron density of the simulated plasma agreed with the experimentally measured density. The agreement held in both the lateral direction and along the laser axis, providing confidence that the simulation accurately modeled the plasma properties. The plasma temperature profile produced by h2d was then compared to the experimental in-band EUV images and temporal profile, measured with a fast photo diode. This showed that the in-band emission that escapes the plasma is

produced where the plasma temperature is around 20 eV. The literature often states that the dominant in-band emission region should be at 30 eV. It may be true that a 30 eV plasma will produce more in-band emission, although the Cretin results in this work show again that 20 eV is the optimum temperature, but absorption is a key factor. Most of the in-band light produced deeper in the plasma than the 20 eV region will be absorbed before it can escape. It is this high absorptivity that makes longer wavelength pump lasers attractive.

In chapter 6 simulated EUV spectra were presented. The most notable result here is that the spectra produced by Cretin using the atomic data from HULLAC contained many of the features observed in the experiments. There are both emission peaks and absorption dips that agree to within the error of the TGS. This is an indication that the atomic data is accurate and contains the relevant atomic transitions. The atomic data were limited to charge states 6 – 14. This caused a charge state saturation that manifests as increased intensity of several distinct peaks near 14.2 nm. This could be remedied by including a broader range of charge states, but with only a few transitions each.

We also saw that there are considerable differences between the different NLTE atomic physics codes, as seen in Figure 3.1. Cretin's calculations of the average ionization level were in the higher range of the codes compared there. This would have the effect of shifting the optimum temperature for efficient in-band emission to a lower temperature. We have already seen that the experimental results along with the h2d simulations showed that the majority of the in-band emission is produced at 20 eV. The results from Cretin agree with this, and it was seen in Figure 6.3 that the in-band light is produced when the plasma temperature is near 20 eV.

The coupling of h2d with Cretin could be a valuable tool for studying LPP if accurate atomic data can be acquired. The work completed here is only the first step for numerical simulations of Sn LPP. From here it would be simple to model many different cases in order to understand the effects of such things as laser intensity, focal spot size, and, probably most importantly, laser wavelength. It may also be possible to study target geometries that would be difficult to produce in the laboratory, yet relatively simple to create in a simulation. This would depend on the ability to resolve the bowties in the computational mesh for h2d.

Finally the effects of pulse duration on EUV emission were explored. Although we were unable to completely reproduce the results found in Ando et al. [49], the data points at 1 and 7 ns agree with those results. It was found that, though the optimum pulse duration is around 2 ns, longer pulse durations, as high as 16 ns, can efficiently produce in-band EUV. It is possible that the trend of increasing CE as the pulse duration increases could continue past 16 ns to the point where 2 ns is no longer the optimum. Further experiments, preferably where the pulse duration can be easily controlled, should be carried out to determine what the optimum pulse duration is for a 1 μm pump laser. This could be accomplished with a modulated low power frontend laser followed by several stages of amplification.

Bibliography

1. Moore, G.E., *Cramming more components onto integrated circuits*, in *Electronics*. 1965.

2. Singh, R., et al., *High-numerical-aperture optical designs.* IBM Journal of Research and Development, 1997. **41**(1): p. 39-48.

3. Smith, B.W., et al., *Water immersion optical lithography at 193 nm.* Journal of Microlithography, Microfabrication, and Microsystems, 2004. **3**(1): p. 44-51.

4. Silfvast, W.T. and N.M. Ceglio, *Introduction to special issue of Applied Optics on soft-x-ray projection lithography.* Applied Optics, 1993. **32**(34): p. 6895-6896.

5. Izawa, Y., et al., *Development of EUV light source by laser-produced plasma.* Journal of Physics IV France, 2006. **133**: p. 1161-1165.

6. Lysaght, M., et al., *Opacity of neutral and low ion stages of Sn at the wavelength 13.5 nm used in extreme-ultraviolet lithography.* Physical Review A, 2005. **72**(1): p. 14502-4.

7. Harilal, S.S., et al., *Spectral control of emissions from tin doped targets for extreme ultraviolet lithography.* Journal of Physics D: Applied Physics, 2006(3): p. 484.

8. Shields, H., et al., *Xenon target performance characteristics for laser-produced plasma EUV sources.* Proceedings of SPIE, 2002. **4688**: p. 94-101.

9. Myers, D., et al., *EUV source system development update: advancing along the path to HVM.* Emerging Lithographic Technologies IX, 2005. **5751**: p. 248-259.

10. Shimada, Y., et al., *Properties of EUV emissions from laser-produced tin plasmas.* Proceedings of SPIE, 2004. **5374**: p. 912-917.

11. Aota, T. and T. Tomie, *Ultimate Efficiency of Extreme Ultraviolet Radiation from a Laser-Produced Plasma.* Physical Review Letters, 2005. **94**(1): p. 015004-4.

12. Lindl, J., *Development of the indirect-drive approach to inertial confinement fusion and the target physics basis for ignition and gain.* Physics of Plasmas, 1995. **2**(11): p. 3933-4024.

13. Pukhov, A. and J. Meyer-ter-Vehn, *Laser Hole Boring into Overdense Plasma and Relativistic Electron Currents for Fast Ignition of ICF Targets.* Physical Review Letters, 1997. **79**(14): p. 2686-2689.

14. Krol, A., et al., *Laser-based microfocused x-ray source for mammography: Feasibility study.* Medical Physics, 1997. **24**(5): p. 725-732.

15. Klosner, M., et al., *Intense plasma discharge source at 13.5 nm for extreme-ultraviolet lithography.* Optics Letters, 1997. **22**(1): p. 34-36.

16. Lebert, R., et al., *Soft x-ray emission of laser-produced plasmas using a low-debris cryogenic nitrogen target.* Journal of Applied Physics, 1998. **84**: p. 3419.

17. Kmetec, J., et al., *MeV x-ray generation with a femtosecond laser.* Physical Review Letters, 1992. **68**(10): p. 1527-1530.

18. Murnane, M.M., et al., *Ultrafast X-ray Pulses from Laser-Produced Plasmas.* Science, 1991. **251**(4993): p. 531-536.

19. Fujioka, S., et al., *Opacity Effect on Extreme Ultraviolet Radiation from Laser-Produced Tin Plasmas.* Physical Review Letters, 2005. **95**(23): p. 235004-4.

20. Perry, T., et al., *Opacity measurements in a hot dense medium.* Physical Review Letters, 1991. **67**(27): p. 3784-3787.

21. Zhang, Y., et al., *Absorption spectra measurements of the x-ray radiation heated sio2 aerogel plasma in "dog-bone" targets irradiated by high power laser pulses.* Journal of Physics: Conference Series, 2008. **112**(4): p. 042005.

22. Koenig, M., et al., *Relative Consistency of Equations of State by Laser Driven Shock Waves.* Physical Review Letters, 1995. **74**(12): p. 2260-2263.

23. Faure, J., et al., *A laser-plasma accelerator producing monoenergetic electron beams.* Nature, 2004. **431**(7008): p. 541-544.

24. Remington, B.A., et al., *A review of astrophysics experiments on intense lasers.* Physics of Plasmas, 2000. **7**: p. 1641-1652.

25. Yamanaka, C., *Physics of Laser Plasma*. Handbook of Plasma Physics, ed. A. Rubenchik and S. Witkowski. Vol. 3. 1991: North-Holland. 1 - 61.

26. Baldis, H.A., E.M. Campbell, and W.L. Kruer, *Physics of Laser Plasma*. Handbook of Plasma Physics, ed. A. Rubenchik and S. Witkowski. Vol. 3. 1991: North-Holland. 361 - 434.

27. Tao, Y., et al. *Comprehensive and reliable diagnostics for the corona of laser-produced plasmas*. CER Technical Report 2005 September 2005 [cited; 05-06:[

28. More, R.M., *Physics of Laser Plasma*. Handbook of Plasma Physics, ed. A. Rubenchik and S. Witkowski. Vol. 3. 1991: North-Holland. 63 - 110.

29. Zel'dovich, Y.B. and Y.P. Raizer, *Physics of shock waves and high temperature hydrodynamic phenomena*, ed. W.D. Hayes and R.F. Probstein. 2002: Dover Publications, Inc.

30. Liberman, D., *Self-consistent field model for condensed matter.* Physical Review B, 1979. **20**(12): p. 4981-4989.

31. Rozsnyai, B.F., *Relativistic Hartree-Fock-Slater Calculations for Arbitrary Temperature and Matter Density.* Physics Review A, 1972. **5**(3): p. 1137.

32. Hummer, D.G., *The atomic internal partition function.* AIP Conference Proceedings, 1988. **168**(1): p. 1-14.

33. Ghosh, K. and G. Ghosh, *The Saha ionization equation.* European Journal of Physics, 1998(1): p. 7.

34. Duston, D., *Line emission from hot, dense, aluminum plasmas.* Physical Review A, 1980. **21**(5): p. 1664.

35. Perrot, F., *Fast calculation of electronic structure in plasmas: The screened hydrogenic model with L-splitting.* Physica Scripta, 1989. **39**: p. 332-337.

36. Nishikawa, T. *Improved Screened Hydrogenic Model*. 1996: AIP.

37. Olson, G.L., *Gray radiation transport in multi-dimensional stochastic binary media with material temperature coupling.* Journal of Quantitative Spectroscopy and Radiative Transfer, 2006. **104**(1): p. 86-98.

38. Brantley, P.S., *Angularly adaptive P1-double P0 flux-limited diffusion solutions of non-equilibrium grey radiative transfer problems.* Journal of Quantitative Spectroscopy and Radiative Transfer, 2006. **104**(1): p. 116-132.

39. Ripolla, J.-F. and A.A. Wrayb, *A half-moment model for radiative transfer in a 3D gray medium and its reduction to a moment model for hot, opaque sources.* Journal of Quantitative Spectroscopy and Radiative Transfer, 2004. **93**(4): p. 473-519.

40. Turpault, R., *A consistent multigroup model for radiative transfer and its underlying mean opacities.* Journal of Quantitative Spectroscopy and Radiative Transfer, 2004. **94**(3-4): p. 357-371.

41. Siewert, C.E. and J. J. R. Thomas, *A method for computing the discrete spectrum basic to multi-group transport theory.* Journal of Quantitative Spectroscopy and Radiative Transfer, 2002. **37**(2): p. 111-115.

42. Spitzer, R.C., et al., *Conversion efficiencies from laser-produced plasmas in the extreme ultraviolet regime.* Journal of Applied Physics, 1996. **79**(5): p. 2251-2258.

43. Choi, I., et al., *Detailed space-resolved characterization of a laser-plasma soft-x-ray source at 13.5-nm wavelength with tin and its oxides.* Journal of the Optical Society of America B, 2000. **17**(9): p. 1616-1625.

44. Jansson, P.A.C., et al., *Liquid-tin-jet laser-plasma extreme ultraviolet generation.* Applied Physics Letters, 2004. **84**(13): p. 2256-2258.

45. Cummings, A., et al., *Conversion efficiency of a laser-produced Sn plasma at 13.5 nm, simulated with a one-dimensional hydrodynamic model and treated as a multi-component blackbody.* Journal of Physics D: Applied Physics, 2005. **38**(4): p. 604.

46. Kieft, E.R., et al., *Comparison of experimental and simulated extreme ultraviolet spectra of xenon and tin discharges.* Physical Review E, 2005. **71**(3): p. 036402.

47. Tanaka, H., et al., *Comparative study on emission characteristics of extreme ultraviolet radiation from CO[sub 2] and Nd:YAG laser-produced tin plasmas.* Applied Physics Letters, 2005. **87**(4): p. 041503.

48. Tao, Y., et al., *Dynamic imaging of 13.5 nm extreme ultraviolet emission from laser-produced Sn plasmas.* Applied Physics Letters, 2005. **87**(24): p. 241502-3.

49. Ando, T., et al., *Optimum laser pulse duration for efficient extreme ultraviolet light generation from laser-produced tin plasmas.* Applied Physics Letters, 2006. **89**(15): p. 151501-3.

50. Harilal, S., et al., *Extreme-ultraviolet spectral purity and magnetic ion debris mitigation by use of low-density tin targets.* Optics Letters, 2006. **31**(10): p. 1549-1551.

51. Hayden, P., et al., *Tin based laser-produced plasma source development for EUVL.* Microelectronic Engineering 2006. **83**(4-9): p. 699-702.

52. Tao, Y., et al., *Mass-limited Sn target irradiated by dual laser pulses for an extreme ultraviolet lithography source.* Optics Letters, 2007. **32**: p. 1338-1340.

53. Sequoia, K.L., et al., *Two dimensional expansion effects on angular distribution of 13.5 nm in-band extreme ultraviolet emission from laser-produced Sn plasma.* Applied Physics Letters, 2008. **92**(22): p. 221505.

54. O'Sullivan, G.D. and R. Faulkner, *Tunable narrowband soft x-ray source for projection lithography.* Optical Engineering, 1994. **33**(12): p. 3978-3983.

55. Koay, C.-S., et al. *High conversion efficiency microscopic tin-doped droplet target laser-plasma source for EUVL*. in *Emerging Lithographic Technologies IX*. 2005. San Jose, CA, USA: SPIE.

56. White, J., et al., *Tin laser-produced plasma source modeling at 13.5 nm for extreme ultraviolet lithography.* Applied Physics Letters, 2008. **92**(15): p. 151501.

57. Sequoia, K., M. Tillack, and Y. Tao, *High Conversion Efficentcy for Laser-Produced EUV Plasmas with Longer Pulse Durations.* Pulsed Power Plasma Science Conference, 2007., 2007: p. 771-771.

58. Ueno, Y., et al., *Enhancement of extreme ultraviolet emission from a CO[sub 2] laser-produced Sn plasma using a cavity target.* Applied Physics Letters, 2007. **91**(23): p. 231501.

59. Tao, Y., et al., *Efficient 13.5 nm extreme ultraviolet emission from Sn plasma irradiated by a long CO[sub 2] laser pulse.* Applied Physics Letters, 2008. **92**(25): p. 251501.

60. Poirier, M., et al., *Modeling of EUV emission from xenon and tin plasma sources for nanolithography.* Journal of Quantitative Spectroscopy and Radiative Transfer, 2006. **99**(1-3): p. 482-492.

61. Cerjan, C., *X-ray plasma source design simulations.* Applied Optics, 1993. **32**(34): p. 6911-6913.

62. Cerjan, C., *Spectral characterization of a Sn soft x-ray plasma source.* Journal of Applied Physics, 1994. **76**(6): p. 3332-3336.

63. Kagawa, T., et al., *RCI Simulation for EUV spectra from Sn ions.* Journal of Physics: Conference Series, 2007. **58**(1): p. 149-152.

64. Sasaki, A., et al., *Simulation of the EUV spectrum of Xe and Sn plasmas.* Selected Topics in Quantum Electronics, IEEE Journal of, 2004. **10**(6): p. 1307-1314.

65. Sasaki, A., et al., *Atomic modeling of the plasma EUV sources.* High Energy Density Physics, 2007. **3**(1-2): p. 250-255.

66. Sizyuk, V., et al., *Numerical Simulation of Laser-Produced Plasma Devices for EUV Lithography Using the Heights Integrated Model.* Numerical Heat Transfer, Part A: Applications, 2006. **49**(3): p. 215-236.

67. Sizyuk, V., A. Hassanein, and T. Sizyuk, *Three-dimensional simulation of laser-produced plasma for extreme ultraviolet lithography applications.* Journal of Applied Physics, 2006. **100**(10): p. 103106-7.

68. Sunahara, A., A. Sasaki, and K. Nishihara, *Two dimensional radiation hydrodynamic simulation for extreme ultra-violet emission from laser-produced tin plasmas.* Journal of Physics: Conference Series, 2008. **112**(4): p. 042048.

69. Tanuma, H., et al., *4d-4f unresolved transition arrays of xenon and tin ions in charge exchange collisions.* Journal of Physics: Conference Series, 2007. **58**(1): p. 231-234.

70. White, J., et al., *Simplified calculation of nonlocal thermodynamic equilibrium excited state populations contributing to 13.5 nm emission in a tin plasma.* Journal of Applied Physics, 2007. **101**(4): p. 043301.

71. Woodruff, P.R., et al. *Simulation of EUV spectral emission from laser-produced tin-doped water plasmas*. in *Emerging Lithographic Technologies XI*. 2007. San Jose, CA, USA: SPIE.

72. White, J., et al., *Simplified modeling of 13.5 nm unresolved transition array emission of a Sn plasma and comparison with experiment.* Journal of Applied Physics, 2005. **98**(11): p. 113301.

73. Raymond F. Smith, J.D., Joseph Nilsen, James R. Hunter, Vyacheslev N. Shlyaptsev, Jorge J. Rocca, Jorge Filevich, and Mario C. Marconi *Refraction effects on x-ray and ultraviolet interferometric probing of laser-produced plasmas.* Journal of the Optical Society of America B, 2003. **20**(1): p. 254.

74. Takeda, M., H. Ina, and S. Kobayashi, *Fourier-transform method of fringe-pattern analysis for computer-based topography and interferometry.* Journal of the Optical Society of America B, 1982. **72**(1): p. 156.

75. Hipp, M., et al., *Digital evaluation of interferograms.* Measurement, 2004. **36**(1): p. 53-66.

76. AIXUV, *Manual for Transmission-grating-spectrograph (TGS)*.

77. Mikrotechnik, J., *Energy monitor E-Mon Manual*. 2004.

78. Larsen, J.T. and S.M. Lane, *HYADES--A plasma hydrodynamics code for dense plasma studies.* Journal of Quantitative Spectroscopy and Radiative Transfer, 1994. **51**(1-2): p. 179-186.

79. Larsen, J.T., *Physics of HYADES.*

80. Amiranoff, F., et al., *Experimental Transport Studies in Laser-Produced Plasmas at 1.06 and 0.53 mum.* Physical Review Letters, 1979. **43**(7): p. 522.

81. Hauer, A., et al., *Measurement and Analysis of Near-Classical Thermal Transport in One-Micron Laser-Irradiated Spherical Plasmas.* Physical Review Letters, 1984. **53**(27): p. 2563.

82. Malone, R.C., R.L. McCrory, and R.L. Morse, *Indications of Strongly Flux-Limited Electron Thermal Conduction in Laser-Target Experiments.* Physical Review Letters, 1975. **34**(12): p. 721.

83. Tarvin, J.A., et al., *Mass-Ablation Rates in a Spherical Laser-Produced Plasma.* Physical Review Letters, 1983. **51**(15): p. 1355.

84. Scott, H.A., *Cretin--a radiative transfer capability for laboratory plasmas.* Journal of Quantitative Spectroscopy and Radiative Transfer, 2001. **71**(2-6): p. 689-701.

85. Rubiano, J.G., et al., *Review of the 4th NLTE Code Comparison Workshop.* High Energy Density Physics, 2007. **3**(1-2): p. 225-232.

86. Mihalas, D., *Stellar atmospheres.* 1978, San Francisco: W.H. Freeman and Co.

87. Stewart, J. and J.K. Pyatt, *Lowering of Ionization Potentials in Plasmas.* Astrophysics Journal, 1966. **144**: p. 1203.

88. Holstein, T., *Imprisonment of Resonance Radiation in Gases.* Physical Review, 1947. **72**(12): p. 1212.

89. Bakshi, V., *EUV sources for lithography*. 2006, Bellingham, WA: SPIE Press.

90. Bar-Shalom, A., M. Klapisch, and J. Oreg, *Theoretical Aspects of HULLAC.* AIP Conference Proceedings, 2002. **635**(1): p. 92-100.

91. Fomenkov, I., et al., *Laser-produced plasma source system development.* Proceedings of SPIE, 2007. **6517**: p. 65173J.

92. Sakaguchi, H., et al., *Absolute evaluation of out-of-band radiation from laser-produced tin plasmas for extreme ultraviolet lithography.* Applied Physics Letters, 2008. **92**(11): p. 111503.

93. Morris, O., et al., *Angle-resolved absolute out-of-band radiation studies of a tin-based laser-produced plasma source.* Applied Physics Letters, 2007. **91**(8): p. 081506.

94. Nagai, K., et al., *Angular distribution control of extreme ultraviolet radiation from laser-produced plasma by manipulating the nanostructure of low-density SnO[sub 2] targets.* Applied Physics Letters, 2006. **88**(9): p. 094102-3.

95. Tao, Y., et al., *Characterization of density profile of laser-produced Sn plasma for 13.5 nm extreme ultraviolet source.* Applied Physics Letters, 2005. **86**: p. 201501.

96. Shimada, Y., et al., *Characterization of extreme ultraviolet emission from laser-produced spherical tin plasma generated with multiple laser beams.* Applied Physics Letters, 2005. **86**(5): p. 051501-3.

97. Richardson, M., et al., *High-efficiency tin-based EUV sources.* Proceedings of SPIE, 2004. **5196**: p. 119.

98. Tao, Y., et al., *Monochromatic imaging and angular distribution measurements of extreme ultraviolet light from laser-produced Sn and SnO[sub 2] plasmas.* Applied Physics Letters, 2004. **85**(11): p. 1919-1921.

99. Yamaura, M., et al., *Characterization of extreme ultraviolet emission using the fourth harmonic of a Nd:YAG laser.* Applied Physics Letters, 2005. **86**(18): p. 181107.

100. Yuspeh, S., et al., *Optimization of the size ratio of Sn sphere and laser focal spot for an extreme ultraviolet light source.* Applied Physics Letters, 2008. **93**(22): p. 221503.

101. Weaver, J.L., et al., *Experimental Benchmark for an Improved Simulation of Absolute Soft-X-Ray Emission from Polystyrene Targets Irradiated with the Nike Laser.* Physical Review Letters, 2005. **94**(4): p. 045002.

102. Back, C.A., et al., *Absolute, time-resolved emission of non-LTE L-shell spectra from Ti-doped aerogels.* Journal of Quantitative Spectroscopy and Radiative Transfer, 2006. **99**(1-3): p. 21-34.

103. Springer, P.T., et al., *Spectroscopic absorption measurements of an iron plasma.* Physical Review Letters, 1992. **69**(26): p. 3735.

104. Tao, Y., et al., *Effect of focal spot size on in-band 13.5 nm extreme ultraviolet emission from laser-produced Sn plasma.* Optics Letters, 2006. **31**(16): p. 2492-2494.

105. Sasaki, A., et al., *Detailed atomic modeling of Sn plasmas for the EUV source.* Journal of Physics: Conference Series, 2008(4): p. 042062.